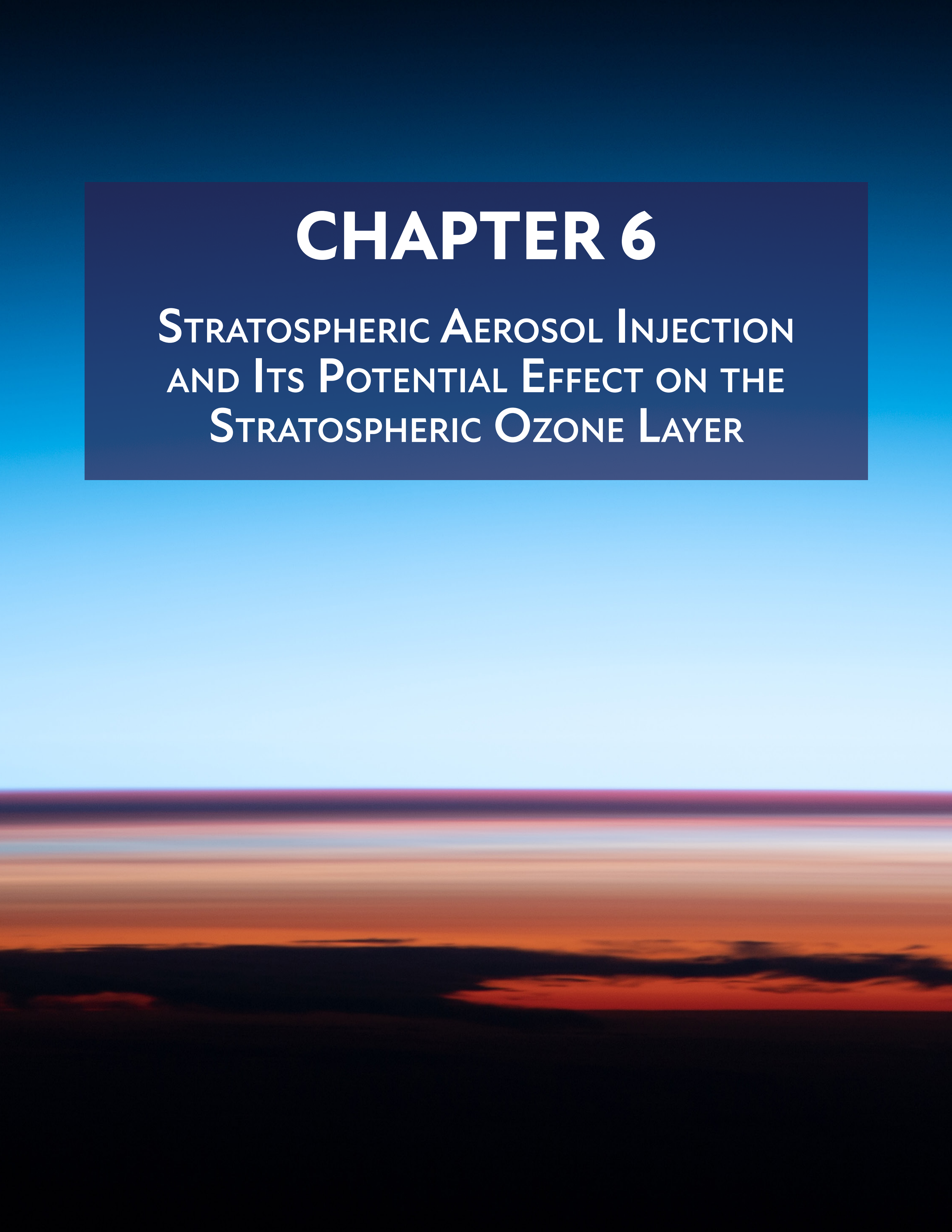

CHAPTER 6

Stratospheric Aerosol Injection and Its Potential Effect on the Stratospheric Ozone Layer

About the cover image:
The topmost, reddish-colored band is an aerosol layer between 23 and 30 km altitude as observed from the International Space Station on 12 February 2020. The layer resulted when the plume of unusually intense wildfires in Australia reached the lower stratosphere.

Photo credit: Provided by the ISS Crew Earth Observations Facility and
the Earth Science and Remote Sensing Unit, Johnson Space Center, NASA

CHAPTER 6

STRATOSPHERIC AEROSOL INJECTION AND ITS POTENTIAL EFFECT ON THE STRATOSPHERIC OZONE LAYER

Lead Authors :	James Haywood Simone Tilmes
Coauthors :	Frank Keutsch Ulrike Niemeier Anja Schmidt Daniele Visioni Pengfei Yu
Contributing Authors :	John Dykema Anthony Crawford Jones Anton Laasko Catherine A. Wilka
Review Editors :	Valentina Aquila Karen H. Rosenlof

CONTENTS

CHAPTER 6: STRATOSPHERIC AEROSOL INJECTION AND ITS POTENTIAL EFFECT ON THE STRATOSPHERIC OZONE LAYER

SCIENTIFIC SUMMARY

Since the 2018 Ozone Assessment global warming has continued, having now reached approximately 1.2 °C above preindustrial levels. All climate model scenarios considered by IPCC (2021) indicate continued future warming beyond 1.5 °C above the preindustrial level, a limit that has been proposed to prevent further detrimental impacts. Ambitious mitigation and decarbonization efforts are required to minimize the likely overshoot of temperatures above this limit and to stabilize global surface temperatures in the future. However, with a temperature overshoot, irreversible impacts on the climate system may still occur. Stratospheric aerosol injection (SAI) has been suggested as a potential mechanism for reflecting sunlight back to space, thereby offsetting some of the surface warming. Evidence from explosive volcanic eruptions and various model simulations has shown that increasing stratospheric sulfate aerosols can substantially cool the planet. SAI and other solar radiation modification (SRM) approaches may therefore be the only option to keep the global surface temperature below the limit of 1.5 °C. The amount and duration of SAI required would depend on how fast atmospheric greenhouse gas (GHG) concentrations are lowered through mitigation and decarbonization efforts.

While SAI could reduce some of the impacts of global warming, it cannot restore past climatic conditions and would very likely cause unintended consequences, including changes in stratospheric ozone concentrations. To date, Earth system models (ESMs) have performed simulations to provide information on the climate impacts, benefits, and risks of SAI. Little research has been done to quantify the effects of SAI on the stratospheric composition and total column ozone (TCO) in a multi-model setting, and even fewer studies have examined the effects of aerosol types other than sulfate. While existing studies do not suggest a deepening of the ozone hole beyond that already experienced, current shortcomings in model representation of required processes limit confidence in the results.

This new chapter of the Ozone Assessment assesses the impacts of SAI on stratospheric ozone through SAI-related changes in stratospheric chemistry and transport. The dependence of SAI effects on future climate change scenarios and injection strategies, as well as uncertainties in our current understanding and model shortcomings, are assessed. Side effects and risks beyond the effects on stratospheric ozone are only briefly covered. It is well recognized that any potential future deployment of SAI is fundamentally linked to complex moral, ethical, and governance issues. These aspects are of critical importance but beyond the scope of this chapter, which will focus solely on physical science.

Framing SAI scenarios and strategies

- **Based on the observed cooling after large volcanic eruptions and various model studies, stratospheric aerosol injection (SAI) has the potential to reduce global mean temperatures. However, SAI cannot fully offset the widespread effects of global warming and produces unintended consequences, including effects on ozone. Details of these effects depend on the specifics of the SAI scenario and injection strategies.** SAI uses stratospheric aerosols to reflect sunlight back to space, thereby cooling the planet. A straightforward offsetting of global warming from greenhouse gases (GHGs) cannot be achieved because SAI reduces a fraction of the incoming sunlight, which is seasonally and latitudinally dependent, while GHGs interact with terrestrial radiation and warm the planet more uniformly across latitudes and seasons. In addition, aerosol heating of the lowermost stratosphere by SAI using sulfate would result in further residual impacts, including changes in regional temperatures, precipitation, and stratospheric ozone. Details of the future climate scenario, the SAI scenario (i.e., the degree of SAI cooling applied), and applied SAI strategy (i.e., the specifics of injection location, timing, and material for achieving predefined climate goals) determine the specifics of the resulting impacts and risks.
    - **Changes in future ozone using SAI depend on details of future climate change and the degree of SAI cooling applied. The three different SAI scenarios considered in this report (Figure 6-2, reproduced here) result in significantly different future ozone.** The "peakshaving" scenario (Panel A in Fig. 6-2) assumes delayed and then aggressive mitigation and carbon dioxide removal (CDR). SAI offsets the overshoot of the surface temperature target until greenhouse gases have been sufficiently reduced. The "strong SAI" scenario (Panel B) assumes a limited or no-mitigation high-warming future scenario, requiring continuously increasing SAI to keep surface temperatures from exceeding the climate target (dashed line). The "medium SAI" scenario (Panel C) assumes a limited or no-mitigation high-warming future scenario in which global warming is reduced to that of a moderate mitigation scenario (red line) by the deployment of SAI. A qualitative illustration of the required injection amounts for each scenario is shown in Panel D. The impacts on ozone of many other possible SAI scenarios have not been comprehensively studied to date. These scenarios currently do not include any socioeconomic feedbacks related to SAI.
    - **In model simulations, different injection strategies have been developed to mitigate some of the unintended climate impacts of SAI.** For the same scenario, the specifics of the injection strategy, including location, timing, and material, can be adjusted to better achieve desired global and regional climate targets and minimize regional changes. Some models include a feedback control algorithm to modulate annual stratospheric sulfur injections in order to reach predefined climate temperature goals and other impact-relevant targets. Adjustments of sulfur injection to account for climate feedbacks help in managing uncertainties and limiting some of the side effects of SAI. Different strategies change the effectiveness of SAI and its effects on stratospheric ozone.

SAI effects on radiation and temperature

- **Multi-model comparisons reveal large uncertainties in forcing and surface cooling per unit of sulfur injected, which are attributed to differences in model complexity in representing key processes and details of SAI strategies.** Using sulfate aerosol, the efficacy of the radiative forcing ranges between –0.04 and –0.1 W m^{-2} per Tg SO$_2$ yr^{-1}, and the resulting surface cooling ranges from 0.04 to 0.14 °C per Tg SO$_2$ yr^{-1} based on a multi-model analysis. Continuous annual injection rates vary between 8 and 16 Tg of SO$_2$ yr^{-1} to cool the Earth by 1 °C; this range is approximately equivalent to the estimated injection amount from Mount Pinatubo in 1991, which resulted in less than 0.5 °C global surface cooling. The significant uncertainties associated with these values are attributed to differences in model representations of stratospheric chemistry, transport, radiation, and aerosol microphysical processes, including differences in model resolution. The choices of SAI injection location, timing, and material influence the resulting stratospheric aerosol mass, optical depth, and surface area density (SAD), which determine both cooling efficacy and impacts on stratospheric ozone.

Mechanisms for SAI impacts on ozone

- **Despite the limited number of model studies, some robust impacts of SAI on ozone have been identified. The combined effects of large-scale, long-term SAI on ozone are driven by 1) an increase in aerosol surface area, 2) stratospheric halogen concentrations, and 3) aerosol-induced heating of the stratosphere, which changes both stratospheric ozone chemistry and stratospheric dynamics.** SAI impacts on total column ozone (TCO) are regionally and seasonally dependent and result in ozone reduction in spring over Antarctica due to the increase in chemical ozone depletion. In contrast, an increase in TCO is possible (with increasing SAI amount) in the tropics, as well as in the winter Northern Hemisphere (NH) in mid- and high latitudes, due to increased tropical chemical ozone production rates and increased poleward transport.
    - **Enhanced stratospheric sulfate aerosol increases stratospheric heterogeneous chemical reaction rates and can enhance or deplete ozone depending on the altitude, latitude, and season.** Net chemical ozone production rates decrease in the lower polar stratosphere in winter and spring where halogen and hydrogen catalytic cycles are most important but increase in the tropical mid-stratosphere where the nitrogen cycle is most important. The magnitude and sign of ozone changes depend on the details of the SAI aerosol distribution and the current stratospheric halogen and nitrous oxide concentrations, as well as on any changes

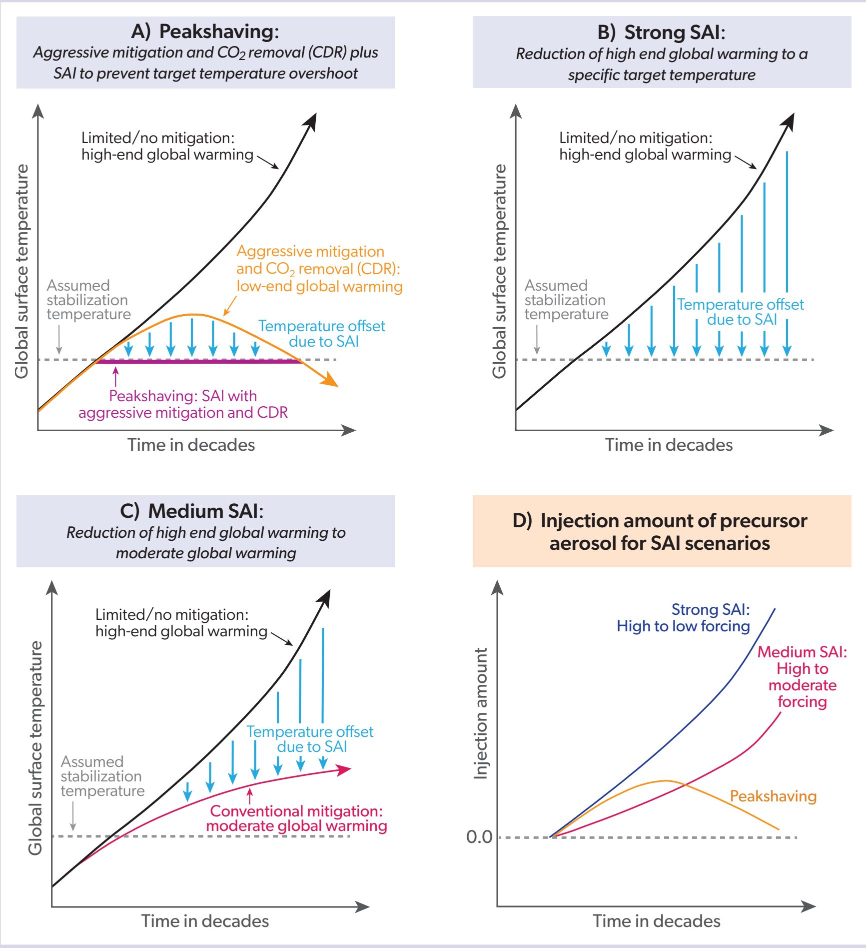

Figure 6-2. Schematic diagram representing the concept of three policy-relevant SAI scenarios: peakshaving scenario, strong SAI scenario, and medium SAI scenario. Different lines illustrate global mean surface temperatures for future scenarios: a limited or no mitigation scenario leading to strong future global warming (black line); a so-called "overshoot scenario" that assumes strong mitigation and Carbon Dioxide Removal (CDR), and leads to a temporary overshoot of global mean temperatures above sustainable limits for some time (orange); a peakshaving scenario that applies temporary SAI to the overshoot scenario in order to prevent the increase in global mean temperature from exceeding these sustainable limits (purple line); and a moderate warming scenario (red). The blue arrows represent the approximate relative magnitude of the temperature impact of the applied SAI. The bottom right panel shows the stratospheric injection that is applied under each of these three scenarios.

in stratospheric water vapor due to changes in transport and temperature that occur in response to SAI.

- **Enhanced stratospheric sulfate aerosol also impacts stratospheric temperature, transport, and chemistry, causing a general increase of ozone concentrations in the tropics and mid- to high latitudes through enhanced transport from the tropics to high latitudes.** Increased sulfate aerosols in SAI scenarios heat the lower tropical stratosphere by 4.6 ± 2.7 °C per 1 °C surface cooling, with variation across models and injection strategy. The heating induced by aerosols changes the vertical and horizontal transport in the stratosphere and polar vortex dynamics and leads to an acceleration of the lower branch of Brewer-Dobson Circulation (BDC). The stronger transport of ozone to high latitudes with SAI can overcompensate for the effects of ozone depletion, especially in the Northern Hemisphere winter in the strong SAI scenario. Heating of the tropopause results in increases in stratospheric water vapor. For any given scenario, the impacts of SAI on stratospheric temperature, transport, and dynamics are strongly model dependent.

SAI impacts on ozone in the future

- **Future changes in TCO resulting from SAI would be in addition to changes driven by future climate conditions and stratospheric halogen burden, as described in *Chapters 3*, *4*, and *5*. The SAI-related TCO changes depend on the required SAI injection rate, which is different for the three defined SAI scenarios (Figure 6-2). Compared to conditions without SAI, significant TCO reductions are expected in October over Antarctica for any SAI applications within the 21st century that are sufficient to appreciably impact climate warming.**
    - **In October over Antarctica, aerosol injection rates sufficient to achieve a 0.5 °C global cooling over the period 2020–2040 result in a reduction of TCO of around 58 ± 20 DU compared to no SAI. Smaller initial injection rates to achieve cooling of 0.2 °C between 2020 and 2040 result in a modeled reduction in TCO of 17 ± 9 DU.** Large injection rates based on the peakshaving and strong SAI scenarios starting in 2020 bring TCO close to the minimum values observed between 1990 and 2000, while smaller injection rates in the medium SAI scenario lead to less TCO reduction. The initial phase-in of SAI leads to relatively larger reductions in TCO over Antarctica in spring compared to a case without SAI because of nonlinearities in microphysical processes.
    - **In October over Antarctica, the magnitude of TCO changes in the second half of the 21st century increase with increasing injection rates. Injection rates and the resulting TCO reductions are scenario, strategy, and model dependent.** Under the strong SAI scenario, with injections starting in 2020, model simulations suggest that Antarctic TCO is reduced by around 55 ± 20 DU in October throughout the 21st century and the ozone hole recovery is delayed between 25 and 50 years. In this case, the effect of continually increasing injections is offset by the simultaneously declining chlorine burden in response to Montreal Protocol provisions. SAI, therefore, counters some of the super recovery of TCO above 1980 values driven by increasing greenhouse gases. The medium SAI scenario results in a smaller TCO reduction of between 9 and 29 DU (based on three models), and the peakshaving scenario results in no significant ozone loss by 2100 due to SAI (based on one model).
    - **In the Arctic in spring, SAI starting in 2020 to achieve global cooling of 0.5 °C by 2040 results in TCO reductions between 13 DU ± 10 DU and 22 ± 21 DU compared to no SAI, with no significant changes after 2040, based on results from two different models. The change in TCO for smaller initial injection rates is not significant.** In the Arctic, chemical changes are in part offset by changes in dynamics, resulting in smaller SAI-induced changes of TCO compared to Antarctica. As a result, SAI only slightly offsets the super recovery of TCO in a high-GHG scenario. Modeled impacts on TCO in the Arctic under the medium SAI scenario are smaller and not significant. These results, which are based on ensemble means of zonal and monthly mean TCO comparisons, do not reflect possible larger regional ozone changes that may occur within the Arctic polar vortex for years with warm and cold vortex conditions.
    - **In NH mid-latitudes in winter, increasing SAI toward the end of the century in both the strong and medium SAI scenarios can lead to a significant TCO increase relative to that in a scenario with no GHG mitigation and without SAI.** In both SAI scenarios, the increased heating in the tropical lower stratosphere causes increased transport of ozone from the tropics to mid- and high latitudes, resulting in a greater increase in TCO with injection amount. SAI, therefore, enhances the super recovery of TCO for a high-GHG scenario. No significant TCO changes occur in NH mid-latitudes in the peakshaving scenario.

Other side effects, risks, and limitations of SAI

- **Limited aerosol injections in a peakshaving scenario minimize SAI-induced side effects and climate risks, including reductions in global precipitation, while climate impacts and risks increase in scenarios with less mitigation and more SAI.** A portfolio of climate responses, including effective mitigation and decarbonization, limits the amount of SAI needed to maintain the global surface temperature below specific targets. Since SAI offsets the warming from atmospheric GHGs, limiting SAI would reduce the risks associated with a potential abrupt termination of SAI. Such an abrupt termination would result in a rapid (within 10 years) return of climate to the non-SAI climate base state if SAI was not restarted. Other side effects induced by SAI, such as Eurasian winter warming and associated precipitation impacts and a significant weakening of the Asian monsoon, depend on the amount of SAI. Ocean acidification depends mostly on atmospheric carbon dioxide (CO_2) concentrations and is impacted only to a small extent by SAI.

SAI using aerosols other than sulfates

- **The use of aerosols other than sulfate is expected to change the effects on ozone via changes in**

heterogeneous chemistry and dynamics and transport. Comprehensive climate model simulations to quantify these effects have yet to be performed. Other aerosol types that absorb less solar radiation would heat the tropical lower stratosphere much less than sulfate. They are also potentially more chemically inert and less impactful on stratospheric ozone. Materials that have been considered include calcium carbonate, titanium dioxide, aluminum oxide, and diamond. The effects on ozone are less certain for these alternate materials owing to the paucity of laboratory and modeling studies investigating them and the lack of natural analogs.

Evaluation of models

- **The study of SAI is aided by natural analogs. Volcanic eruptions and pyrocumulonimbus events are useful, albeit imperfect, natural analogs for assessing SAI.** Present-day Earth system models may not accurately simulate the effects of stratospheric aerosol perturbations on ozone and other side effects. Remote sensing and in situ observations of volcanic eruptions and pyrocumulonimbus (pyroCb) formation provide essential information on the stratospheric evolution of injected sulfur dioxide and resultant sulfate aerosol, which can be used to assess and improve SAI models. However, remote and in situ observations valuable for evaluating the effects of injected aerosols on the ozone layer are generally lacking. SAI scenarios with continuous aerosol (precursor) injections will produce different stratospheric aerosol distributions than pulse injections that occur with natural analogs; therefore, accurately simulating these natural events is a necessary but not sufficient constraint on model fidelity in representing SAI.

6.1 INTRODUCTION

There is growing recognition that the 21st Conference of the Parties (COP21) to the United Nations Framework Convention on Climate Change limits of 1.5 °C (IPCC, 2018) or 2 °C above preindustrial levels are going to be extremely difficult to achieve under even the strongest mitigation scenarios (e.g., Rogelj et al., 2016; Millar et al., 2017; IPCC, 2018; Tollefson, 2018). Reaching these temperature limits to avoid further climate impacts may require considering additional interventions, including solar radiation modification (SRM) and carbon dioxide removal (CDR). While CDR may be effective in the long run, this approach very likely does not prevent an overshoot of these surface temperatures limits for some time. Even a temporary overshoot of surface temperatures can lead to irreversible climate impacts (IPCC, 2021, 2022), and SRM may be the only option to prevent this.

Various SRM approaches have been discussed to deliberately cool the planet by reflecting more sunlight back to space (NAS, 2021). One such approach is injecting aerosols (or their gaseous precursors) to enhance the stratospheric aerosol layer and reflect additional sunlight back to space, thereby cooling the planet. This approach is referred to as stratospheric aerosol injection (SAI; NAS, 2021) and has been motivated by the observed temporary surface cooling after large explosive volcanic eruptions. Such eruptions periodically inject millions of tonnes of sulfur dioxide (SO_2) into the stratosphere, where it forms reflective sulfate aerosols (Robock, 2000). Since Earth system models (ESMs) have been used to study the effects of SO_2 injections from volcanic eruptions for decades, they have been adopted to also study the effects of SAI using SO_2 injections. Furthermore, the availability of extensive observations subsequent to these eruptions allows evaluation of the impacts of SO_2 injections in models. Besides the intended benefits of SAI to counter the effects of global warming, SAI produces unintended consequences and risks, including impacts on stratospheric ozone (e.g., Crutzen, 2006).

This chapter provides the first comprehensive stratospheric ozone-focused assessment of the state of SAI research. *Section 6.1* covers motivations and a brief history and defines specific terminology used in this assessment. *Section 6.2* provides background on important processes required for simulating SAI, sensitivities to the assumed injections on radiative forcing and aerosol surface area density, and model uncertainties in simulating these processes. *Section 6.3* assesses the general effects of SAI on ozone concentrations and sensitivities on ozone to the injection details. *Section 6.4* quantifies changes in total column ozone (TCO) for three specified future scenarios and briefly addresses additional side effects and climate impacts of SAI in the context of different future scenarios to place the impact on TCO in the context of the larger arena of this developing research field. The chapter abstains from addressing complex moral, ethical, and governance issues (e.g., Robock, 2008a; Preston, 2013; Lawrence et al., 2018). *Section 6.5* assesses the potential effects of using materials other than sulfate for SAI, and *Section 6.6* assesses the importance of natural analogues of aerosol injections for reducing uncertainties in process understanding and model representation for SAI projections.

6.1.1 Motivation for Assessing the Effects of SAI on Stratospheric Ozone

Global warming has continued over the last decade and currently (in 2021) stands at approximately 1.2 °C above preindustrial levels (IPCC, 2021). Each of the observed global annual mean temperatures over the last seven years has been among the warmest on record, and the global mean temperature in 2020 tied with 2016 as the warmest year on record (IPCC, 2021). All climate model simulations suggest continued global warming throughout the next two decades (IPCC, 2021; **Figure 6-1**). Future global modeling scenarios known as Shared Socioeconomic Pathways (SSPs) range from a very strong mitigation scenario that includes negative carbon emissions (SSP1-1.9) to a limited or no-mitigation pathway (SSP5-8.5), which leads to an acceleration of global warming to around 5.5 °C above preindustrial conditions by 2100 (**Figure 6-1**). The range of surface temperature changes per scenario is indicated by the colored shaded area in **Figure 6-1**.

The multi-model mean from even the strongest mitigation pathway (SSP1-1.9) overshoots the 1.5 °C target, peaking around 2050 before falling below 1.5 °C above preindustrial levels by 2100. A growing body of evidence shows that climate-induced damages frequently scale exponentially rather than linearly in key variables such as the frequency of extreme precipitation (e.g., Myhre et al., 2019), heatwaves (e.g., Christidis et al., 2015), and droughts (e.g., Samaniego et al., 2018) and that the accelerated warming of the high latitudes causes thawing of permafrost, melting of glaciers, and reductions of sea ice leading to sea level rise. Tipping points might also be reached whereby key elements of the climate system such as the Amazon rainforest or the West Antarctic ice sheet could irreversibly collapse (e.g., Lenton et al., 2019). The application of climate intervention methods may be the only option to prevent the future climate from reaching critical temperatures and potential tipping points (e.g., NAS, 2021).

Climate intervention (CI) is defined in this report as "the deliberate large-scale manipulation of an environmental process that affects the Earth's climate, in an attempt to counteract the effects of global warming." We adopt the terminology "climate intervention" (NRC, 2015), although we recognize that "climate engineering" (Hamilton, 2013; Keith, 2013), "climate geoengineering" (Lawrence et al., 2018), and "geoengineering" (Shepherd, 2009; NAS, 2021) are also commonly used throughout the scientific literature. Two very different CI strategies have been proposed: carbon dioxide removal (CDR) and solar radiation modification (SRM) (**Box 6-1 Figure 1**). CDR methods seek to actively remove carbon dioxide from the atmosphere, while SRM seeks to reduce global warming by increasing the reflectivity of the planet.

CDR methods include afforestation, ocean alkalinization, and iron fertilization to promote marine carbon uptake, as well as technologies such as bioenergy with carbon capture and storage (BECCS), capturing carbon from biofuels in the form of charcoal to use as a fertilizer (biochar), and direct air capture (Shepherd, 2009; Lawrence et al., 2018; NRC, 2015 Lee et al., 2021; Josep et al., 2021). These methods have not yet been developed at a scale large enough to reduce carbon dioxide concentrations significantly within the next one to two decades (Keller et al., 2018; Fuss et al., 2020), but they have the potential to contribute significantly to global warming abatement in the second half of the 21st century. Some CDR approaches have their own side effects that may limit their large-scale deployment, including substantial costs or implications for, e.g., water availability or food production (Smith et al., 2016). Such concerns further strengthen the motivation to understand the implications of SRM.

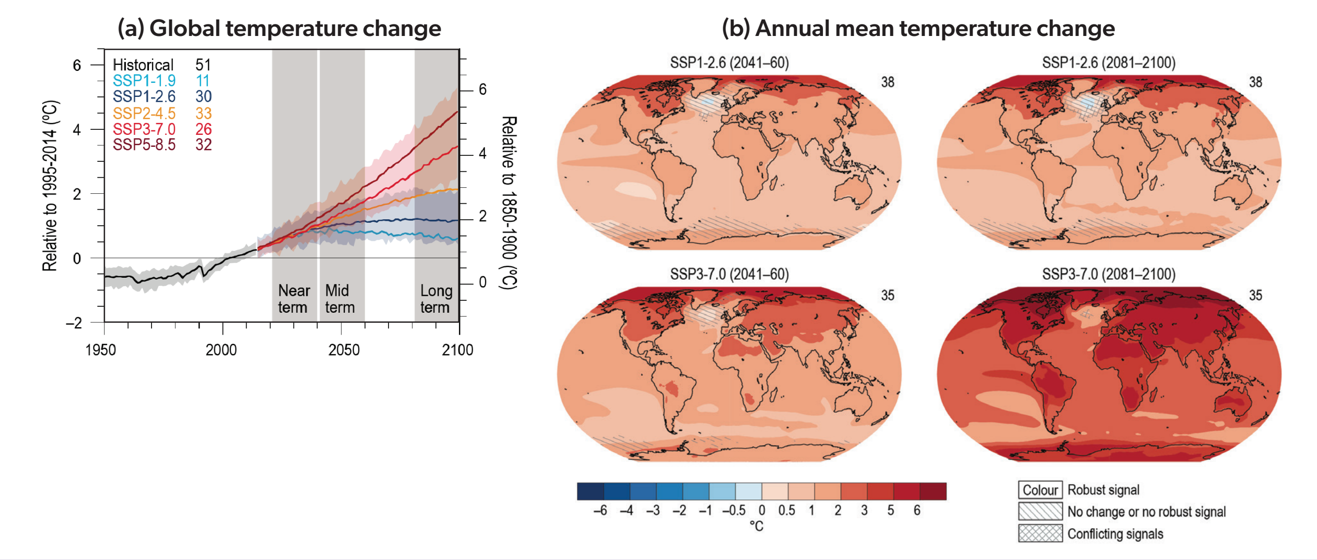

Figure 6-1. (a) Multi-model simulated time series from 1950 to 2100 for global annual average surface air temperature changes relative to the 1995–2014 average (left axis) and the 1850–1900 average (right axis). The curves show averages over the CMIP6 simulations, the shadings around the SSP1-2.6 and SSP3-7.0 curves show 5–95% ranges, and the numbers in the legend after each experiment show the number of model simulations used. (b) The global mean distribution of mid-term (2041–2060) and long-term (2081–2100) changes in annual mean surface temperature. The number of model simulations used is indicated in the top right of the maps. No overlay indicates regions where the change is robust and emerges from internal variability (i.e., 66% of the models show a change greater than the internal-variability threshold, and at least 80% of the models agree on the sign of change). Diagonal lines indicate regions with no change or no robust significant change. Crossed lines indicate areas of conflicting signals. [Both panels reproduced from Lee et al., 2021.]

SRM methods include utilizing mirrors in space; increasing the reflectivity of land or ocean surfaces (surface albedo); increasing the reflectivity of marine clouds (marine cloud brightening, MCB); and increasing the reflectivity of the stratospheric aerosol layer via stratospheric aerosol injection, SAI. We adopt the term "stratospheric aerosol injection" throughout this report but recognize that "stratospheric aerosol intervention" and "stratospheric aerosol geoengineering" are also frequently used in the scientific literature. Cirrus cloud thinning (CCT) is also frequently considered under SRM, although this method is based more on reducing cirrus cloud impact on outgoing terrestrial radiation rather than on reflecting sunlight (e.g., Lohmann and Gasparini, 2017). Based on assessments of the potential cooling impact, readiness, cost-effectiveness, and risks (e.g., Shepherd, 2009; NAS, 2021), SAI is potentially one of the most effective global methods. SAI involves the long-term injection of aerosols, or their precursors, into the stratosphere, where their atmospheric lifetime can reach one to two years. The resulting enhanced aerosol layer reflects sunlight back to space, thereby cooling the planet (Shepherd, 2009; Lawrence et al., 2018; NAS, 2021). While the technology for SAI does not yet exist, it has become the most discussed SRM technique in the scientific literature. A portfolio of CI strategies has been suggested in addition to mitigation and adaptation, which could include a temporary application of SAI to avoid the worst impacts of global warming until emissions reductions and CDR reduce and stabilize atmospheric GHG concentrations (e.g., Long and Shepherd, 2014; Sugiyama et al., 2018).

In many studies, SO_2 has been considered as the injection material for SAI because volcanic eruptions serve as natural analogs to SAI (see *Section 6.6* for more details). Observations after large explosive volcanic eruptions that injected large amounts of SO_2 into the stratosphere have conclusively demonstrated a measurable reduction in global surface temperatures within a year or two (e.g., Angell and Korshover, 1984; Hansen et al., 1992; Soden et al., 2002). Multiple smaller eruptions during the early 21st century are also thought to have contributed to the observed masking of some of the global warming at that time (e.g., Santer et al., 2014; Haywood et al., 2014). Explosive volcanic eruptions that emit sulfur species into the stratosphere allow benchmarking of current-generation aerosol and climate models against a wealth of observations of the impacts of volcanic emissions on ozone concentrations and sulfate aerosol properties, including their temporal and spatial evolution. However, in most cases, volcanic eruptions also inject other materials, including dust, halogens, and water, which result in different effects compared to those from sulfur injections alone (e.g., Zhu et al., 2020). There are also clear limits to this analogy, because explosive eruptions are pulsed injections of material into a relatively small area of the stratosphere, which contrasts with continuous or repeated injections (or a slow ramp-up) of SO_2 in strategically selected locations under SAI scenarios (e.g., Duan et al., 2019). These differences can make it difficult to project SAI impacts on ozone and climate response based on volcanic eruptions.

Another analog of SAI is the injection of aerosols into the stratosphere in vigorous wildfire events that result in the formation of pyrocumulonimbus clouds (pyroCbs). A number of satellite observations have recently shown that biomass-burning aerosols embedded in pyroCbs can reach the stratosphere. Enhanced

Box 6-1. Overview of Climate Intervention Methods

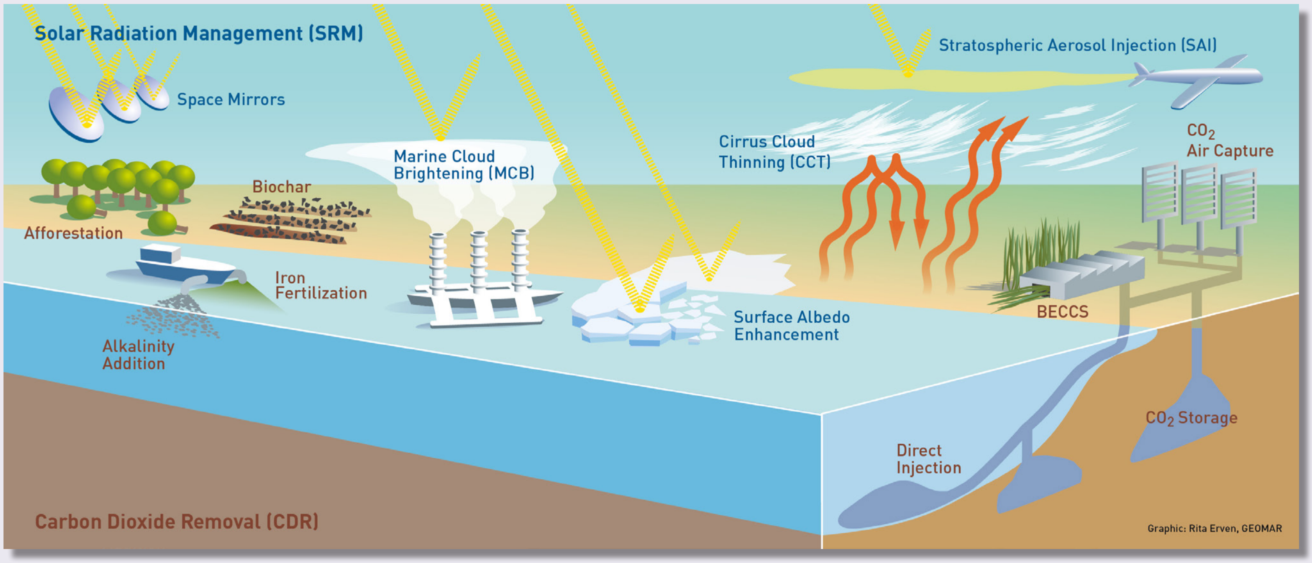

Box 6-1 Figure 1. Schematic diagram showing some prominent proposed climate intervention methods. CDR methods include afforestation, biochar, BECCS, iron fertilization, and alkalinity addition to the ocean. SRM methods represented are SAI, MCB, space mirrors, CCT, and surface albedo enhancement technologies. *Courtesy of Rita Erven, GEOMAR.*

Glossary of Climate Intervention Terminology

BECCS*: bioenergy with carbon capture and storage. A CDR technique using energy derived from any form of biomass or its metabolic by-products whereby a relatively pure stream of carbon dioxide (CO_2) from industrial and energy-related sources is separated (captured), conditioned, compressed, and transported to a storage location for long-term isolation from the atmosphere.

Biochar*. A CDR technique producing a stable carbon-rich material produced by heating biomass in an oxygen-limited environment. Biochar may be added to soils to improve soil functions and to reduce greenhouse gas emissions from biomass and soils, as well as for carbon sequestration.

CCT: cirrus cloud thinning. A proposed climate intervention technique often classified under SRM, although it relies on increasing emissions of terrestrial radiation to space.

CI: climate intervention. Defined in this report as the deliberate large-scale manipulation of an environmental process that affects the Earth's climate, in an attempt to counteract the effects of global warming. This includes both SRM and CDR.

CDR*: carbon dioxide removal. Anthropogenic activities that remove CO_2 from the atmosphere and durably store it in geological, terrestrial, or ocean reservoirs, or in products. This includes existing and potential anthropogenic enhancement of biological or geochemical sinks and direct air capture and storage but excludes natural CO_2 uptake not directly caused by human activities.

MCB: marine cloud brightening. An SRM climate intervention strategy aimed at brightening low marine clouds through the injection of aerosol particles, thereby increasing the planetary albedo.

Planetary albedo. The ratio of the amount of solar radiation reflected by the planet to that incident upon it. The global broadband planetary albedo is approximately 0.3.

SAI: stratospheric aerosol injection. A proposed SRM technique to enhance the stratospheric aerosol layer to increase the reflectivity of the planet and hence reduce global mean surface temperatures.

Space mirrors. A proposed SRM technique to block some sunlight by placing mirrors at the Lagrangian point between Earth and the sun to decrease the global surface temperature.

SRM*: solar radiation modification. The intentional modification of the Earth's shortwave radiative budget with the aim of reducing warming. Stratospheric aerosol injection, marine cloud brightening, and land surface albedo modification are examples of proposed SRM methods.

Surface albedo. The ratio of the solar radiation reflected by Earth's surface to that incident upon it. The broadband mean surface albedo is approximately 0.15.

**Adopted from IPCC (2018).*

solar absorption by black carbon and the organics-dominated chemical composition of these smoke particles can impact ozone and climate differently from sulfate aerosols (e.g., Rieger et al., 2021).

6.1.2 A Brief History of SAI Research

The earliest suggestion of injecting sulfur into the stratosphere to combat global warming was proposed by Budyko (1974). This topic was then only occasionally discussed in the scientific literature for the next three decades (e.g., Rasch et al., 2008a, and references therein). Crutzen et al. (2006) was one of the first to suggest possible impacts of SAI on stratospheric ozone. He used simple scaling arguments derived from the Pinatubo eruption to estimate that stratospheric injections of around 10 Tg $SO_2\,yr^{-1}$ (1 Tg = 1 million tonnes) would be needed to balance the warming impact of doubled atmospheric concentrations of carbon dioxide. Wigley (2006) used a simple energy balance model and derived a similar estimate, suggesting a combined mitigation and SAI approach for stabilizing climate. These and other early simple model approaches were improved upon by introducing models that represent the sulfur cycle more explicitly using single-moment aerosol models and that include the representation of oceans either through slab-ocean (Rasch et al., 2008b) or fully coupled ocean models (Robock et al., 2008b). The first studies that quantitatively assessed the impact of deliberate SAI upon the ozone layer also appeared, finding a considerable delay in the Antarctic ozone hole recovery (Tilmes et al., 2008; Heckendorn et al., 2009).

Thereafter, more and more SAI modeling studies began to appear using fully coupled global atmospheric-ocean models. These models often did not include interactive stratospheric chemistry (e.g., Kravitz et al., 2009; Jones et al., 2010; 2011; Niemeier et al., 2011; English et al., 2012). A few studies attempted to compare the impacts of similar SAI simulations performed across different climate models (e.g., Jones et al., 2011; Rasch et al., 2008b; Schmidt et al., 2012), but comprehensive attribution of differences in results from climate models proved to be hampered by the lack of standardization of the objectives of the SAI approaches and the related emission scenarios. These problems led to the first comprehensive attempts to standardize model scenarios by the Geoengineering Model Intercomparison Project (GeoMIP; Kravitz et al., 2011).

GeoMIP formulated idealized model experiments to aid understanding of the effects of SAI on the Earth system (Kravitz et al., 2011) and provides the most comprehensive multi-model assessment of the effects of SRM to date (e.g., Kravitz et al., 2015). Different GeoMIP experiments have evolved over time, from solar dimming experiments where the solar constant was turned down to offset instantaneous quadrupling or steadily increasing carbon dioxide concentrations (referred to as the G1 and G2 scenarios, respectively; Kravitz et al., 2015) to more complicated and policy-relevant SAI experiments (the G3, G4, and G6 scenarios; Kravitz et al., 2015). Simulations were run using fully coupled global climate models (CMIP5 and CMIP6 generations), with most models performing the relatively simple solar dimming experiments (e.g., Kravitz et al., 2011; 2021; Niemeier et al., 2013). Fewer models were able to directly simulate sulfur injections, which requires comprehensive stratospheric aerosol microphysical modeling. The first GeoMIP-coordinated multi-model assessments of impacts on stratospheric ozone and surface ultraviolet radiation were documented by Pitari et al. (2014). Two model experiments, G3 and G6, include both SAI and solar dimming versions (G3, G3S, G6solar, and G6sulfur; Kravitz et al., 2015), allowing comparisons of the impacts of the two methods (Niemeier et al., 2013; Xia et al., 2017; Visioni et al., 2021a; Jones et al., 2021). These studies have shown that solar dimming is an imperfect analog for modeling the climate impacts of SAI and assessing its effects on stratospheric ozone (see *Section 6.3*). Other multi-model comparisons are in progress, based on the Chemistry-Climate Model Initiative (CCMI; Morgenstern et al., 2017; Plummer et al., 2021); these use a prescribed aerosol distribution to examine the effects of SAI on stratospheric ozone.

Besides additional single-model studies that use simple equatorial injection strategies, more complex SAI deployment strategies to minimize residual climate impacts have been developed and applied (Kravitz et al., 2017) and used as the basis for other studies, including the Geoengineering Large ENSemble project (GLENS; Tilmes et al., 2018a; 2020; see **Box 6-2**). A new large-ensemble model study using a similar strategy to GLENS, the Assessing Responses and Impacts of Solar climate intervention on the Earth system with stratospheric aerosols project (ARISE; Richter et al., 2022), has recently been documented.

In parallel with the development of individual and coordinated modeling studies, there has been limited research into potential delivery mechanisms. SAI would require the long-term delivery of millions of tonnes of SO_2 or other suitable materials into the stratosphere for any substantive global cooling (e.g., Smith et al., 2020; Robock, 2020); currently, no scalable delivery system exists. A fleet of specially designed high-altitude aircraft has been suggested as a feasible delivery system (McClellan et al., 2012; Smith and Wagner, 2018), although tethered balloons, rockets, artillery, and rigid towers have also been suggested (Robock et al., 2009; Davidson et al., 2012). Each of these is hampered by technological constraints, in particular when it comes to delivery of significant payloads above 20 km altitude. There have also been suggestions for enhancing stratospheric aerosol concentrations through lower-altitude tropospheric injections, both using photophoretic levitation (Keith, 2010) and absorption of sunlight to loft the particles into the stratosphere (Gao et al., 2021). Other suggestions include injecting carbonyl sulfide in the upper troposphere where it is transported to the stratosphere and slowly forms sulfate (Quaglia et al., 2022). However, the technical logistics of practical deployment through such means have not been sufficiently explored. No outdoor field experiments have been conducted up to this point, and detailed discussions about requirements and issues regarding field experiments are presented in the recent NAS (2021) report.

6.1.3 SAI Scenarios and Strategies

Just as the impacts of future global warming (including the evolution of stratospheric ozone) strongly depend on future emissions pathways, the impacts of SAI are strongly dependent on the details of the SAI scenario and the underlying future greenhouse gas emissions pathway (the baseline scenario; e.g., Niemeier et al., 2011; Tilmes et al., 2017; Richter et al., 2017, Jones et al., 2018; Irvine et al., 2020, Tilmes, 2020). Multiple hypothetical SAI scenarios and strategies have been developed for modeling studies, based on the goals of the specific project or the purpose of the research; some were designed for understanding specific processes in the climate system and others for impact relevance.

In this section, we define the terms "scenario" and "strategy".

6.1.3.1 SAI Scenarios

We define "SAI scenario" as the desired global mean outcome. While IPCC (2021) defines its scenarios in terms of the global mean radiative forcing by 2100, SAI scenarios are most frequently defined in terms of the global mean temperature or degree of cooling. Current SAI scenarios do not include socioeconomic feedbacks of the implementation of SAI. Examples of SAI scenarios include maintaining global mean temperatures at 1.5 °C or 2 °C above preindustrial conditions or reducing the global mean temperature from a high-end global warming scenario to a more moderate global warming scenario. Three different SAI scenarios are assessed with regard to effects on total column ozone in *Section 6.4*.

Without SAI, only very drastic and immediate mitigation and significant CDR can prevent overshoot of an assumed stabilization surface temperature (**Figure 6-2**, grey, dashed lines). The global mean surface temperature from most projected future scenarios exceeds the 1.5 °C and 2 °C COP21 limits (**Figure 6-1**; IPCC, 2021). Here, we assess modeling studies that investigate the effects of SAI on ozone based on three SAI scenarios. Each of these scenarios considers different baseline GHG scenarios and temperature targets and therefore has different impacts on total column ozone (TCO). While many possible SAI scenarios have been studied, the most comprehensive large-ensemble or multi-model studies relevant for TCO impacts can be summarized in the three scenarios analyzed here. The first two scenarios are based on ensemble simulations from one modeling framework, while the results of the last scenario are based on a multi-model study using three different ESMs. All scenarios discussed here inject SO_2 into the stratosphere to form sulfate aerosols; comprehensive ESM studies using other injection materials currently do not exist. Schematic diagrams of the three scenarios, together with the temporal evolution of the quantity of SO_2 injected, are provided in **Figure 6-2**, and each of the injection strategies is discussed in detail in the subsections that follow. Note that the resulting temperature change from specific baseline scenarios are themselves very uncertain owing to differences in climate sensitivity of the various models. In addition, there is significant uncertainty about how much cooling can be achieved with a specific amount of SAI (*Section 6.2.2.*). Consequently, the amount of injection needed to reach specific temperature targets is very uncertain.

Peakshaving Scenario. The peakshaving scenario prevents overshoot of global mean surface temperature above assumed temperature limits by applying a limited amount of SAI to avoid the worst impacts of global warming during the period it takes for strong mitigation and decarbonization efforts to reduce and stabilize greenhouse gas concentrations (e.g., Wigley, 2006; Long

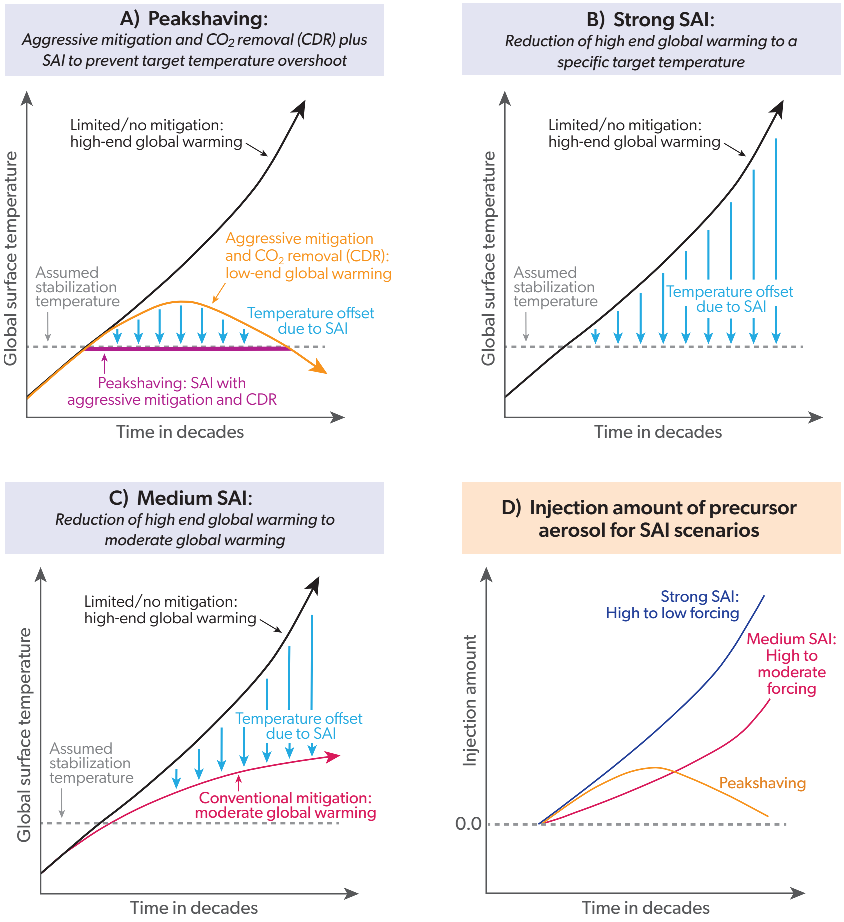

Figure 6-2. Schematic diagram representing the concept of three policy-relevant SAI scenarios: peakshaving scenario, strong SAI scenario, and medium SAI scenario. Different lines illustrate global mean surface temperatures for future scenarios: a limited or no mitigation scenario leading to strong future global warming (black line); a so-called "overshoot scenario" that assumes strong mitigation and Carbon Dioxide Removal (CDR), and leads to a temporary overshoot of global mean temperatures above sustainable limits for some time (orange); a peakshaving scenario that applies temporary SAI to the overshoot scenario in order to prevent the increase in global mean temperature from exceeding these sustainable limits (purple line); and a moderate warming scenario (red). The blue arrows represent the approximate relative magnitude of the temperature impact of the applied SAI. The bottom right panel shows the stratospheric injection that is applied under each of these three scenarios.

and Shepherd, 2014; Sugiyama et al., 2018). For this scenario, SAI is slowly phased in and later phased out to keep temperatures from rising above the target temperature (**Figure 6-2**, top left panel). Depending on the effectiveness of mitigation and decarbonization efforts, SAI application may be required for several decades or even centuries before atmospheric greenhouse gases have been sufficiently reduced to stabilize surface temperatures (e.g., Tilmes et al., 2016, 2020; Jones et al., 2018). A peakshaving scenario that requires strong mitigation and CDR may pose the least risk to the climate system among the scenarios analyzed in this assessment, since the relatively limited deployment time and injection rate reduce potential side effects and any termination effect (see *Section 6.4.2*). Currently, the impacts on ozone for this scenario can be assessed based only on a single model (Tilmes et al., 2020), using a baseline scenario SSP5-3.4-OS (**Box 3-4 Figure 1**) that follows the SSP5-8.5 high-forcing scenario until 2040 and after that deploys large-scale CDR and strong reductions in methane. SAI is applied to keep surface temperatures at 1.5 °C above preindustrial levels while minimizing inter-hemispheric and pole-to-equator gradients. This scenario requires maximum injections of up to ~15 Tg SO_2 yr^{-1} around 2060; 15 Tg SO_2 is approximately the amount injected by the explosive 1991 Mount Pinatubo eruption. An additional scenario to keep surface temperatures at 2.0 °C above preindustrial levels, which would reduce injections of sulfur by approximately 50% relative to stabilizing temperatures at 1.5 °C above preindustrial levels, has also been performed (Tilmes et al., 2020).

Strong SAI Scenario. The strong SAI scenario prevents high-end global warming under a scenario with high projected greenhouse gas emissions (Representative Concentration Pathway [RCP] 8.5 / SSP5-8.5, **Box 3-4 Figure 1**), with the objective of meeting the COP21 targets. Large ensembles of this scenario have so far been performed using only CESM (WACCM) within the GLENS simulations (Kravitz et al., 2017, Richter et al., 2017, Tilmes et al., 2018a; *Section 6.1.*) and CESM2 (WACCM6) (Tilmes et al., 2020), although a more limited number of ensembles have been performed with other models (Jones et al., 2018). To prevent surface temperature from increasing under this greenhouse gas scenario using SAI, steadily increasing sulfur injections between 2020 and 2100 are required (**Figure 6-2**, top right panel). Injections were simulated to reach between 30 Tg SO_2 yr^{-1} (Jones et al., 2018) and 55 Tg SO_2 yr^{-1} (Tilmes et al., 2018a) by 2100. This is between three and five times the mass of sulfur injected per year by the Mount Pinatubo eruption in 1991 (assuming Pinatubo injected 10 Tg SO_2; Mills et al., 2017). Different SAI strategies (*Section 6.1.3.2*) have been applied to this SAI scenario, using a feedback controller (**Box 6-2**) and varying the altitude of injections or injecting only at the equator. These different strategies lead to different impacts on stratospheric ozone (Jones et al., 2018; Kravitz et al., 2019; Tilmes et al., 2021). As the SO_2 injection increases with time, the risks of side effects and any termination effect (see *Section 6.4.2*) also increase with time.

Medium SAI Scenario. As in the strong SAI scenario, the medium scenario also prevents the high-end global warming projected under a scenario with high greenhouse gas emissions, but its target surface temperature is that of a more moderate greenhouse gas emissions scenario (RCP4.5 / SSP2-4.5). This scenario leads to moderate global warming that is significantly above COP21 targets. Six GeoMIP models have performed this type of modeling experiment using SSP5-8.5 as the baseline scenario and temperatures under the SSP2-4.5 greenhouse gas scenario as the target; this is known as the GeoMIP G6 scenario (e.g., Jones et al., 2021; Visioni et al., 2021a; Tilmes et al., 2022). Only three of the participating six models (CNRM-ESM2-I, UKESM1-0-LL, and CESM2(WACCM)) include interactive chemistry and calculate the effect of SAI on TCO (*Section 6.4.2*). The SAI strategy for achieving these scenarios was defined by injections in a region around the equator. Progressively larger SO_2 emissions are required between 2020 and 2100, ranging from 3 to 7 Tg SO_2 yr^{-1} in 2050 and reaching between 20 and 30 Tg SO_2 yr^{-1} by 2100 (see **Figure 6-2**, bottom left panel). This scenario is similar to halving future global warming (e.g., Irvine et al., 2019, 2020). Analysis based on GLENS simulations show that for this scenario only, 1.3% of land areas would see a significant change in water availability compared to present day, and those regions would experience wetting, not drying, contradicting the assumption that solar climate intervention leads to a general drying (Irvine et al., 2020).

6.1.3.2 SAI Strategies

The underpinning deployment assumptions for achieving specific climate goals are defined here as "SAI strategies". Strategies are understood here as the specifics of SAI applications, injection locations (including latitude, longitude, and altitude), injection timing (continuous or pulse injections), and injection material. Model simulations have revealed several robust side effects if global solar dimming or injections at the equator are applied, which include overcooling of tropical regions, continued residual warming in polar regions, and overcompensation of global mean and regional precipitation reductions (Bala, 2008; Robock et al., 2008b; Schmidt et al., 2012; Niemeier et al., 2013; Kravitz et al., 2013; Tilmes et al., 2013; Huneeus et al., 2014; Kravitz et al., 2021). Additional side effects on the climate system may include a shift in the intertropical convergence zone (ITCZ) and hurricane frequency and intensity in simulations that apply SAI to a single hemisphere (Haywood et al., 2013; Jones et al., 2017; see *Section 6.4.2*). Model experiments have therefore applied specifically designed strategies to minimize some of these deleterious side effects. These strategies include injections at multiple locations and seasons in order to reduce impacts on, e.g., inter-hemispheric and pole-to-equator surface temperature gradients, using a feedback control algorithm (see **Box 6-2**). Other examples of SAI strategies include the use of sulfate or chemically inert materials instead of SO_2 (*Section 6.5*). Thus, different SAI strategies could deliver the same SAI scenario but result in different impacts on climate and stratospheric ozone.

6.2 IMPACTS OF SAI ON RADIATIVE FORCING, TEMPERATURES, AND AEROSOL SURFACE AREA DENSITY

To cool the Earth's surface using stratospheric aerosol injection (SAI), sulfate aerosols or their gaseous precursors (e.g., SO_2) would be deliberately injected into the stratosphere. Transport by stratospheric winds associated with the Brewer–Dobson circulation (BDC) can result in near-global coverage of the resulting sulfate aerosol layer. Transport processes are coupled to microphysical processes, as they determine sulfur concentrations, sulfate particle numbers, and size distributions. These nonlinear processes make the impact of SAI very dependent on the injection strategy. For example, model simulations show that stratospheric

Box 6-2. Reaching Climate Targets Using Feedback Control

Earlier SAI studies often modeled injection of SO$_2$ or sulfate aerosols within a region around the equatorial stratosphere, resulting in a nonuniform global distribution of stratospheric sulfate with a maximum concentration at the equator (*Section 6.2*). This results in an overcooling of the tropics and an undercooling at high latitudes compared to a scenario without SAI. In a new approach, changes in surface temperature are modulated through injections of sulfur at four predefined locations, 15°N, 15°S, 30°N, and 30°S. The resulting stratospheric sulfate distribution is more evenly spread across latitudes (**Box 6-2 Figure 1**, top panels). Multiple stratospheric injection latitudes coupled with a feedback control algorithm has been used to maintain 2020 surface temperatures while following the high-GHG emissions RCP8.5 baseline scenario (Kravitz et al., 2017). The so-called feedback loop successfully responds to changes in climate feedbacks by adjusting the injection amounts for each of the predefined injection locations. Model simulations that use this approach are able to keep global mean surface temperatures at predefined levels with regional surface temperatures more similar to present day compared to using equatorial injections (**Box 6-2 Figure 1**, middle and bottom panels).

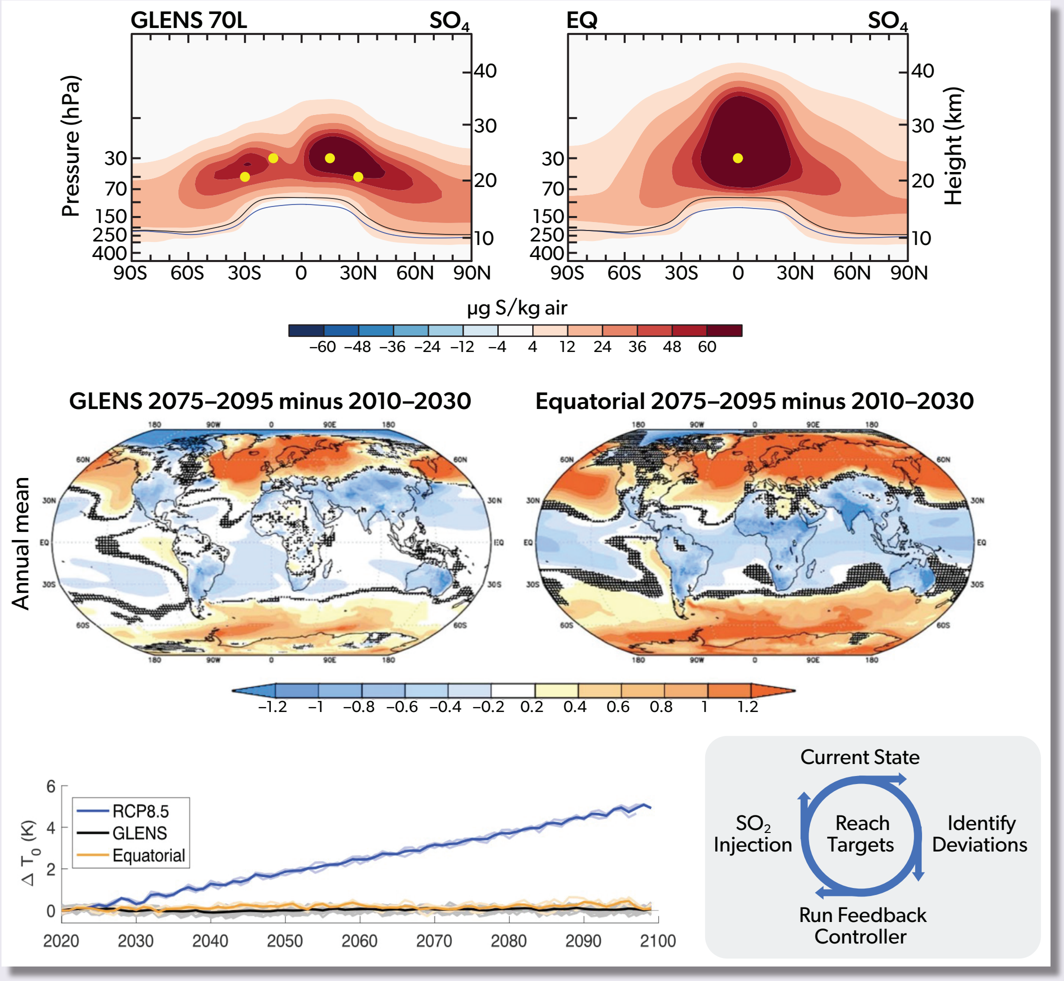

Box 6-2 Figure 1. *(top)* Zonal mean changes in sulfate concentrations between simulations with and without SAI over the period 2070–2089 using GLENS four-point injections *(left)* and equator injections *(right)*. Both simulations use a feedback controller *(bottom right)* that iteratively adjusts the injected sulfur amount in each location in order to stabilize the global, annual average surface temperature (for the equatorial injection) and in addition the inter-hemispheric and pole-to-equator surface temperature gradients for the four-point injections *(bottom left)*. The tropopause location in the control (no injection) run is shown in black and for the SAI experiment in blue; injection locations are indicated as yellow dots. *(middle)* Maps of surface temperature change (K) for the GLENS four-point injections *(left)* and for equatorial injections *(right)*, where the change refers to the difference in the mean over the periods 2075–2095 and 2010–2030. Stippling indicates regions that are not statistically significant at the 95% confidence level, as calculated using Welch's t-test. *(bottom left)* Change in annual mean surface temperature from the 2010–2030 average following the RCP8.5 (blue) scenario and with SAI following the GLENS four-point injection strategy (black) and equatorial injection strategy (orange). Faint lines indicate individual model run ensemble members, and thick lines indicate ensemble means. *(bottom right)* Illustration of the feedback control loop. [Adapted from Tilmes et al., 2020, and Kravitz et al., 2019.]

A feedback control algorithm in climate models was first applied to maintain global mean surface temperatures by reducing the solar constant (MacMartin et al., 2014a, 2014b; Kravitz et al., 2014). Later, this method was applied to meet three climate objectives at the same time: the targeted global mean surface temperature, inter-hemispheric temperature gradient, and pole-to-equator temperature gradient (Kravitz et al., 2016). This method was then integrated into a more complicated framework using the Whole Atmosphere Community Climate Model (WACCM; Mills et al., 2017, MacMartin et al., 2017). Such an approach requires precalculated response functions for each injection latitude. Emissions adjustments have been tested for different time periods. For example, injections were adjusted annually for the GLENS model runs, while seasonal injection adjustments were performed in later studies (Visioni et al., 2019, 2020a). Different climate targets have also been suggested, including precipitation-based climate metrics and targets for sea ice extent, although these strategies are still in their infancy (Lee et al., 2021).

injection at the equator or at four points at 30°N, 15°N, 15°S, and 30°S, will result in very different spatial and size distributions of the aerosols (see **Box 6-2**) and cause different impacts on ozone. In addition, model-specific differences in physics and simulated tracer transport add to simulated nonlinearities, and both are responsible for large differences between model results. It is therefore still uncertain how much surface temperature reduction would be obtained for 1 Tg yr^{-1} of SO_2 injection. This section provides the foundation for understanding related microphysical and transport processes, as well as SAI interactions with radiation (*Section 6.2.1*). *Section 6.2.2* summarizes model differences and shortcomings in representing processes important for SAI and assesses the effects of SAI on radiation and surface temperatures, based on multiple model comparisons. *Section 6.2.3* assesses uncertainties in the radiation and temperature effects as a result of using different injection strategies. A summary of the important SAI processes and uncertainties based on existing model studies is then given in *Section 6.2.4*.

6.2.1 Aerosol Processes Relevant for SAI Efficacy

The life cycle of sulfate in the stratosphere is governed by chemistry, aerosol microphysics, transport, and interaction with radiation. All of these nonlinear interactions, together with details of the injection strategies, determine the final aerosol spatial distribution, burden, aerosol optical depth, and aerosol surface area density (SAD). A brief summary of processes and interactions important for SAI is included in the following section, mainly based on Kremser et al. (2016).

6.2.1.1 Sulfate Aerosol Chemistry and Microphysical Processes

Six major processes are important for the formation and the life cycle of stratospheric sulfate aerosols: oxidation, nucleation, coagulation, condensation, evaporation, and sedimentation (**Figure 6-3**). These processes impact the total aerosol number concentration and size distribution, as well as the aerosol lifetime and radiative properties. Natural sources of stratospheric sulfuric acid (H_2SO_4) include oceanic and terrestrial emissions of carbonyl sulfide (COS) and dimethyl sulfide (DMS). COS is stable in the troposphere and is oxidized to form gaseous precursors of sulfate aerosols in the stratosphere. The main natural sources for the other stratospheric gaseous precursor, SO_2, are large explosive volcanic eruptions and large forest fires. SO_2 can be oxidized to H_2SO_4 and then condenses to form sulfate aerosols, which have a lifetime of 1–1.5 years in the stratosphere both under unperturbed conditions (Weisenstein et al., 2006; Mills et al., 2016) and with SAI (Heckendorn et al., 2009; Niemeier et al., 2011; English et al., 2012; Visioni et al., 2017a). In the stratosphere, new aerosols are mainly formed by the co-condensation of H_2SO_4 and water via binary homogeneous nucleation (e.g., Vehkamäki et al., 2002). Low temperature, high relative humidity, and low particle SADs provide optimal conditions for homogeneous nucleation (Kremser et al., 2016). The primary nucleation regions within the stratosphere are the tropical tropopause layer (TTL) region and the polar middle stratosphere. The location and amount of any SAI application impacts the speed of the nucleation processes. Particle growth of newly formed aerosols occurs mainly through coagulation, particle collision, and condensation. The growth due to condensation of H_2SO_4 vapor on particles is mainly controlled by H_2SO_4 concentrations and occurs throughout the life cycle of the stratospheric aerosol particles. Coagulation is most effective between fine (aerosol radius $r < 0.01$ μm) and coarse ($r > 1$ μm) particles (Seinfeld and Pandis, 2007), as large particles have a large surface and are a good target for smaller particles. This behavior has consequences for SAI. In contrast to sporadically erupting large volcanoes, SAI requires continuous injections to sustain an aerosol layer over many years. The consequent formation of new fine particles occurs in regions populated by particles from previous injections. In such conditions, coagulation becomes the dominant microphysical process affecting aerosol size, especially for continuous injections (Heckendorn et al., 2009). Injections over short time periods and small areas (e.g., one grid box) confine small freshly nucleated particles to a smaller region (in time and space). This reduces the relevance of coagulation, resulting in smaller particles (Niemeier and Timmreck, 2015). In any case, the particle size becomes larger with increasing injection rate as freshly formed particles coagulate and sulfur condenses on larger existing particles (Weisenstein et al., 2022).

The main removal processes for stratospheric aerosols are sedimentation of large particles and evaporation in warmer regions of the stratosphere above 32 to 35 km (Kremser et al., 2016). The evaporated gases may later re-nucleate and re-condense in cold stratospheric areas, mostly at high latitudes and high altitudes, after being transported within the BDC (see *Section 6.2.1.2*). Sedimentation or gravitational settling through the tropopause depends strongly on particle size, as well as the local vertical updraft velocity, which counters sedimentation. In regions with strong vertical advection, such as the tropical pipe, both vertical advection and sedimentation play important roles in the resulting particle number and size. Thus, Earth system models (ESMs) have to accurately model the transport processes, as well as growth processes, of aerosols. The resulting aerosol particle size distribution influences the aerosol optical properties (for

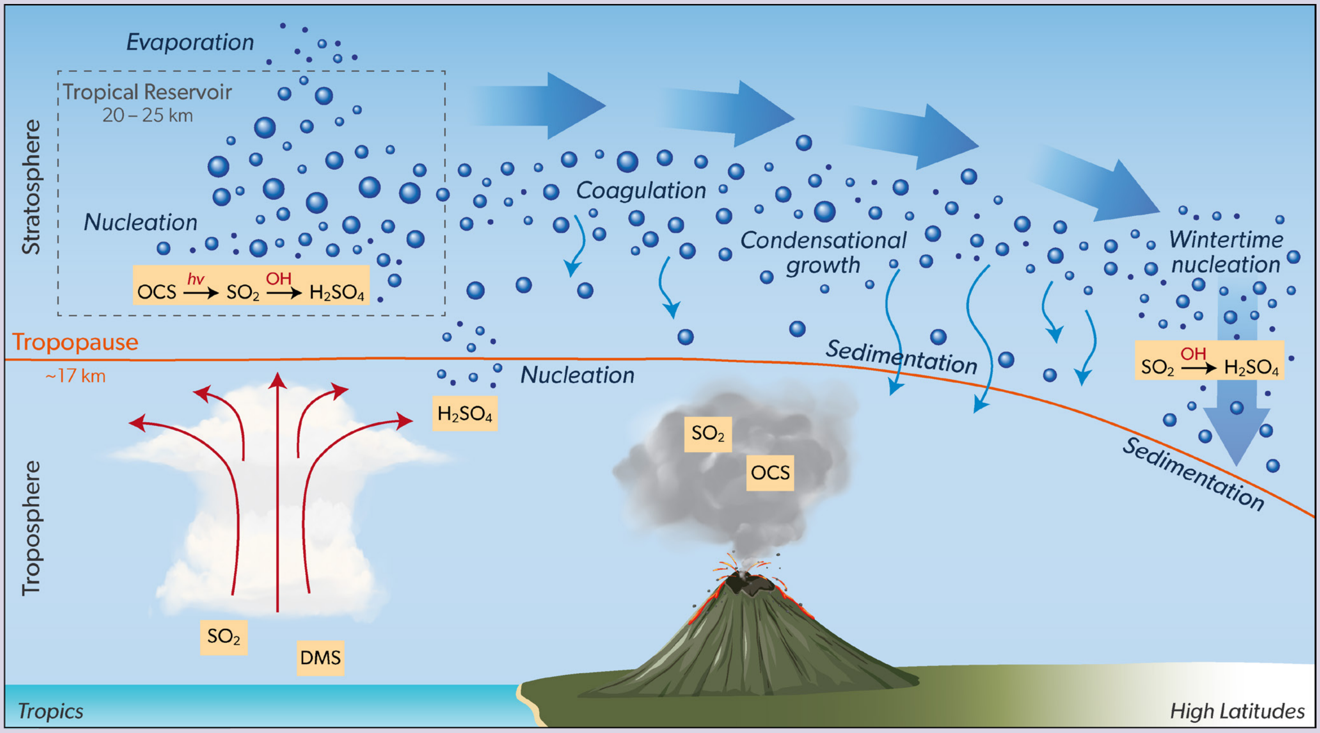

Figure 6-3. Life cycle of stratospheric sulfate, relevant aerosol microphysical processes, and stratospheric transport processes. [Adapted from Kremser et al., 2016.]

both solar and terrestrial radiation), the residence time, and the dispersion and transport of the aerosols.

6.2.1.2 Transport

Sulfur injected into the lower stratosphere is transported zonally with strong stratospheric winds and vertically and meridionally by the BDC, which is a large hemispheric circulation with an ascendant branch in the tropics and subsidence over the poles at high latitudes (**Figure 6-3**). In the extratropics, poleward motion dominates, with fast meridional mixing in the "surf zone" in the lower stratosphere (15 to 30 km altitude) and a slower meridional motion above. The surf zone is bounded by transport barriers around the winter polar vortex and in the subtropics (Butchart, 2014). Equatorial injections into the lower part of the tropical stratosphere result in the transport of aerosols towards the poles and mixing in the surf zone leads to a globally distributed aerosol layer. The main descending branch at high latitudes in the winter hemisphere (and the related transport out of the stratosphere), is a sink for the sulfate aerosols. In the wintertime, the air in the polar vortex is isolated, so sulfate aerosols reach the poles in spring and summer only after the breakdown of the polar vortex.

The resulting aerosol distribution differs with the location of the injection and the injection strategy (Heckendorn et al., 2009; Pierce et al., 2010; Niemeier et al., 2011; English et al., 2012; Tilmes et al., 2017). The injection of sulfur into the ascending branch of the BDC in the tropics results in the longest sulfate lifetime and global coverage. Injections at high latitudes result in a much shorter lifetime, and the aerosol is mostly confined to the hemisphere of injection (Robock et al., 2008a, Jones et al., 2017). The subtropical transport barriers hinder exchange between the hemispheres. Therefore, continuous injections poleward of ~30° latitude in one hemisphere will result in the transport of only a small amount of aerosol into the other hemisphere (e.g., Tilmes et al., 2017). Within the equatorial tropics, wind patterns are determined by the Quasi-Biennial Oscillation (QBO), a pattern of strong easterly or westerly jets, which change direction with a phase of roughly two years. The heating of the stratosphere from aerosols can alter the QBO and with that other transport patterns (see *Section 6.3*). It is impossible to create a persistent regional stratospheric sulfate layer over only a small region or a single country because of the nature of stratospheric transport.

6.2.1.3 Interaction with Radiation

Sulfate aerosols scatter solar (shortwave [SW]) radiation and absorb at terrestrial (i.e., infrared [IR] and near-IR) wavelengths. The addition of sulfate aerosols in the stratosphere therefore causes an intentional cooling of the troposphere as a result of reduced incoming SW radiation and an unintentional warming in the lower stratosphere through the absorption of IR and near-IR radiation (Timmreck and Graf, 2006; Aquila et al., 2014). This results in a change in the temperature gradient within the stratosphere and troposphere. For a realistic size distribution of stratospheric aerosols, as determined from observations following volcanic eruptions, scattering of sunlight is most efficient for aerosols with effective radii between 0.3 and 0.4 μm; aerosols below 0.1 μm and above 1 μm are inefficient at interacting with radiation at solar wavelengths (Mie, 1908; Dykema et al., 2016). Absorption of terrestrial radiation increases strongly for sulfate aerosols larger than 1 μm owing to increases in the imaginary part of the refractive indices at these wavelengths (Laakso et al., 2022).

For reference, stratospheric aerosol effective radii, observed at Laramie, Wyoming (USA), were in the range of 0.1 to 0.15 µm before the Mount Pinatubo eruption and around 0.4 to 0.5 µm one year after the eruption (Kleinschmitt et al., 2017; Deshler et al., 2019). For SAI, the resulting effective radii of aerosols depend on the injection strategy, varying between 0.2 and 0.6 µm for injection rates between 2 and 100 Tg SO_2 yr^{-1} (Kleinschmitt et al., 2018; Laakso et al., 2022).

Radiative forcing provides a useful metric for assessing the magnitude of the climatic response from a particular perturbation, as the temperature response to a perturbation is approximately proportional to its forcing (IPCC, 2021). Following the IPCC definition, the effective radiative forcing (ERF) is the change in net (solar plus terrestrial) irradiance at the top of the atmosphere (TOA) caused by the stratospheric aerosol as measured in W m^{-2} after the stratosphere has adjusted to radiative equilibrium. General circulation models (GCMs) using prescribed sea surface temperatures (SSTs) calculate ERF as an estimate of the TOA radiative imbalance. For simply comparing the effects of different sulfate distributions, models are able to internally calculate the radiative forcing of the sulfate for each model time step: the radiation module performs a second calculation without considering stratospheric aerosols. In this way, the instantaneous radiative forcing (IRF) of the aerosol can be determined without considering the impacts of adjustments on climate. IRF is not directly comparable to the radiative forcing changes derived from ESMs that are coupled to an ocean module, as they include adjustments of stratospheric and surface temperatures.

The effectiveness of SAI varies with season and latitude because it depends on the amount of incoming solar radiation. Therefore, very little SW reduction is expected from SAI at high and mid-latitudes in winter, while more continuous radiative changes occur in the tropics. In contrast, the radiative forcing of greenhouse gases (GHGs) varies only a little with latitude as it is mostly caused by absorption of terrestrial radiation, which is less dependent on the season (Govindasamy and Caldeira, 2000; Kravitz et al., 2011). GHG temperature impacts also have a different vertical profile compared to that from SAI due to the heating of the sulfate aerosols in the lower stratosphere (Ferraro et al., 2014; Henry and Merlis, 2020). Therefore, uniformly applied SAI across the globe does not completely offset the warming of GHGs, and residual warming still occurs, particularly at high latitudes.

Secondary feedbacks, such as modifications in the concentration of stratospheric water vapor and ozone due to SAI, may also affect the overall radiative forcing. A stratospheric water vapor increase, produced by the warming of the lower stratosphere and the tropopause, would have a positive radiative effect (Richter et al., 2017; Krishnamohan et al., 2019; Huang et al., 2020; Visioni et al., 2021b). The stratospheric lifetime of methane (CH_4) and its concentration may also be affected by tropospheric and stratospheric hydroxyl radical (OH) changes. Both contributions would result in a minor positive forcing that would offset only a fraction of the large negative forcing produced by the aerosols (Visioni et al., 2017a).

6.2.2 Model Uncertainties and Simulated Global Radiative Forcing and Surface Temperature Response to SAI

Variations in modeled radiative forcing and surface temperature response to SAI arise from differences in the simulated

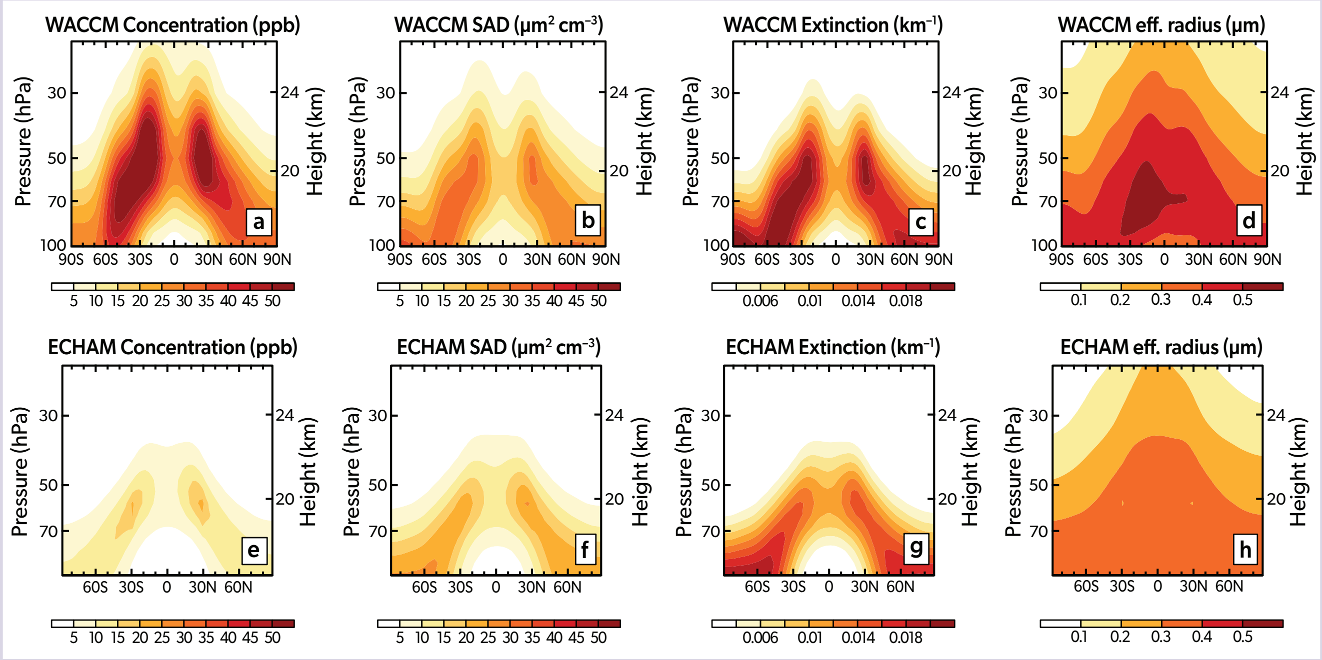

Figure 6-4. (a, e) The concentration of total sulfur (gas and aerosols), (b, f) surface area density (SAD), (c, g) light extinction, and (d, h) effective radius, averaged zonally and over time, as simulated with the CESM (WACCM) (a–d) and MAECHAM5-HAM (e–h) models. In both models, 10 Tg SO_2 yr^{-1} is continuously injected into two single grid boxes at 30°N and 30°S at an altitude of 18–21 km. [Adapted from Weisenstein et al., 2022.]

sulfate aerosol geographic distribution and particle size, which result from details of the injection strategy and the complex and nonlinear interplay between transport, oxidation chemistry, and microphysical processes (*Section 6.2.1*). Most existing climate models neglect at least some of the couplings between these processes, and variations across models in what processes are accounted for may also feed back onto impacts on chemistry and ozone. First, we outline the range of existing stratospheric aerosol descriptions in models and the differences in their complexity that contribute to the uncertainty in our understanding of the effects of SAI on stratospheric ozone. After that, an assessment of the range of changes in radiative forcing and surface temperature from different GCMs is given.

6.2.2.1 Aerosol Representation in Models, Complexity, and Uncertainties

The simplest way to approximate the effects of SAI in models is to turn down the solar constant. However, the impacts of these global solar dimming experiments differ substantially from SAI applications using sulfate aerosols. Besides resulting in very different climate outcomes, these experiments do not consider the increase in stratospheric SAD and do not simulate the associated chemical effects. Furthermore, in contrast to SAI, solar dimming does not heat the lower tropical stratosphere (Niemeier et al., 2013; Kalidini et al., 2015; Irvine et al., 2017; Jones et al., 2021); hence, the effect on stratospheric ozone is quite different from simulations where aerosols are added to the stratosphere (see *Section 6.3*). Slightly more complicated approaches prescribe a thin stratospheric aerosol layer at a constant geopotential height (Krishnamohan et al., 2019) or scale aerosol microphysical and optical properties via imposed aerosol optical depth (AODs), taken from aerosol microphysical simulations or observations after the Mount Pinatubo eruption. In this case, the models simulate aerosol radiative interactions and climate impacts but no feedback on particle transport and chemistry (e.g., Niemeier et al., 2013; Ferraro et al., 2015). The next step up in complexity is an online representation of bulk aerosol properties via single-moment schemes: this accounts for the transport of aerosol mass but not for the evolution of the aerosol size distribution, which is prescribed (e.g., Jones et al., 2017). Much more complex aerosol parameterizations describe processes such as nucleation, condensation, and coagulation and include explicit treatment of both aerosol mass and number distributions assuming lognormal distributions (e.g., Mills et al., 2016; Niemeier and Timmreck, 2015). The most general, but computationally expensive, representations of aerosol properties are size-resolving sectional aerosol schemes, which often use a high number of size bins with fixed widths (Kokkola et al., 2009; English et al., 2012; Kleinschmitt et al., 2018; Laakso et al., 2022).

Different aerosol microphysical parameterizations can result in significantly different aerosol distributions and radiative forcing. Comparisons of two different aerosol microphysical schemes within one GCM (Laakso et al, 2022), a modal scheme with four sulfate modes and a sectional scheme with ten bins, indicate that the modal scheme requires a roughly five-times-larger sulfur injection than the sectional scheme to reduce the radiative forcing to preindustrial levels by the end of the century (see *Section 6.2.3*).

Differences in simulated transport also have an impact on the resulting sulfate concentrations. **Figure 6-4** shows results from two GCMs that apply the same SAI strategy (Niemeier et al., 2020). Both models are coupled to modal aerosol schemes. The model with the strongest vertical uplift results in an aerosol concentration twice as large as in the model with weaker vertical uplift (compare **Figure 6-4a** and **e**). The stronger vertical uplift also results in larger SAD and light extinction and larger effective radii (**Figure 6-4b–d**, **f–h**), with consequences for aerosol light scattering efficiency and heterogeneous chemistry.

The interaction between the injected sulfur and other stratospheric chemical components can also impact the simulated

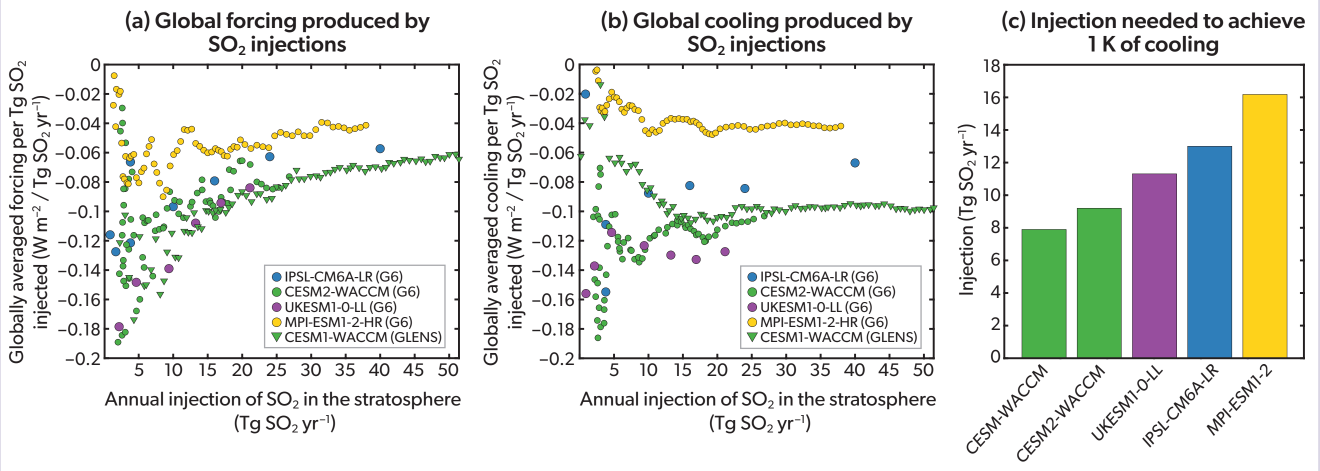

Figure 6-5. Radiation and temperature response from different Earth system model simulations of the GeoMIP scenario G6sulfur (medium SAI) and of CESM1 (WACCM) simulations in the GLENS (strong SAI) scenario. The injection rate is in Tg SO_2 yr^{-1} (after Visioni et al., 2021a). (a) Globally averaged top-of-the-atmosphere all-sky radiative forcing (which includes the response of all ESM components) normalized by the SO_2 injection rates. (b) Annual mean global surface temperature anomaly normalized by the SO_2 injection rates. A five-year running mean has been applied to the results. (c) Injection rate of SO_2 needed to cool the globally averaged surface temperature by 1 K.

results of SAI (Richter et al., 2017). For example, a decrease in stratospheric ozone and the associated relative cooling owing to reduced absorption of UV radiation partially counters the warming due to the aerosols. This influences stratospheric dynamics and causes a different dynamical response, including in the QBO, compared to a model with prescribed ozone concentrations (Brenna et al., 2021; Franke et al., 2021), and this can also affect the ozone concentration (*Section 6.3.2.2*). The understanding of these interactions is still limited. Also, the complexity and treatment of chemical processes in different models affect the simulated impacts on other chemical species such as OH and CH_4 (Visioni et al., 2017b), which in turn affect ozone. The omission of very-short-lived halogen species in models may lead to an underestimation of the impacts of SAI on ozone (Tilmes et al., 2012). Other model shortcomings include missing processes or interactions, such as how aerosols from SAI might affect cirrus clouds as they settle out of the stratosphere (Visioni et al., 2022). An overview of model improvements needed to narrow uncertainties in SAI is summarized in Eastham et al. (2021).

6.2.2.2 Simulated Surface Temperature and Radiative Forcing

The aim of SAI is to reduce temperatures at the Earth's surface to reduce the risk of climate change through a small reduction in the amount of solar radiation reaching the surface. **Figure 6-5** shows the cooling per mass of SO_2 injected in SAI simulations in six different Earth System models (ESMs) under the medium and strong SAI scenarios (**Figure 6-2**). For the medium SAI scenario, not all models used the same injection strategy; some models injected sulfur between 10°N and 10°S and between 18 and 20 km, while CESM2-WACCM injected at the equator at around 25 km altitude. Some models simulated the sulfate evolution with interactive stratospheric aerosol microphysics, while other models used an imposed sulfate distribution that had been calculated using a GCM coupled with a microphysical aerosol module (see Visioni et al., 2021a, for details). Some models included interactive stratospheric chemistry, while others did not. Differences across the models in radiative forcing efficiency (forcing per injected unit mass) and efficiency of temperature reduction are largest for smaller simulated injection amounts (<20 Tg SO_2 yr^{-1}; **Figure 6-5a**, **b**) and somewhat smaller for larger injections. The forcing efficiency ranges from −0.04 to −0.1 W m^{-2} per Tg SO_2 yr^{-1} and the temperature efficiency from −0.04 to −0.14 K per Tg SO_2 yr^{-1} for an injection of 20 Tg SO_2 yr^{-1}. This implies that sustained injection rates of 8–16 Tg of SO_2 yr^{-1} would be needed in order to cool the Earth by 1 K (**Figure 6-5c**; Visioni et al., 2021a). This range in the amount of sulfur that would be injected annually in this SAI scenario is approximately equal to the observationally-based estimate of the mass of sulfur injected into the stratosphere by Mount Pinatubo in a single event in 1991.

6.2.3 Sensitivities of Aerosol Distribution to Injection Strategy and Consequences for Radiation

Various SAI strategies have been studied with models that include aerosol microphysical processes. Different injection

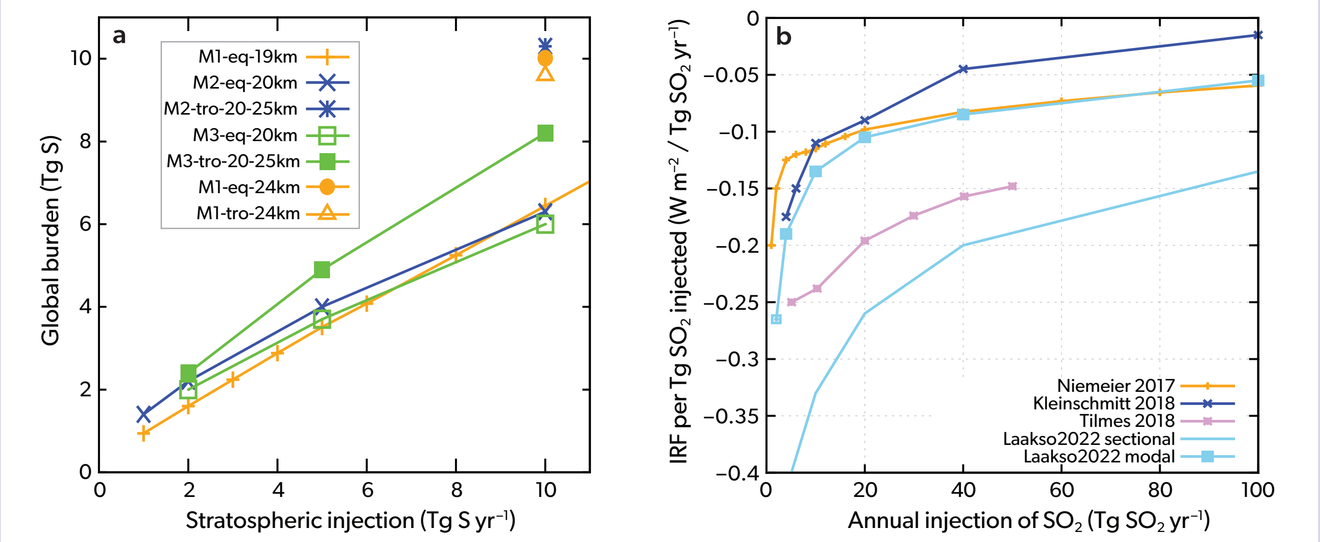

Figure 6-6. (a) Globally averaged sulfur burden for varying injection rates based on simulations in different models (after Niemeier and Timmreck, 2015). M1: results of Niemeier and Timmreck (2015) for injections of SO_2 at the equator (5°N, 120°E) at altitudes of 19 km and 24 km. M2: injections of SO_2 between 5°N and 5°S at an altitude of 20 km and between 30°N and 30°S between altitudes of 20 and 25 km (English et al., 2012). M3: same injection method as M2, but results after Pierce et al. (2010). (b) Internally derived stratospheric instantaneous aerosol radiative forcing (IRF) at the top of the atmosphere scaled per mass of injected SO_2, based on three GCMs (Niemeier and Schmidt, 2017; Kleinschmitt et al., 2018; Laakso et al., 2022) and one ESM (Tilmes et al., 2018a). All models include aerosol microphysical processes. IRF is calculated as the difference between two calls to the model radiation scheme, one including and one excluding sulfate aerosols, and does not allow the stratosphere to equilibrate to the new radiative equilibrium. While IRF is a measure of the change in radiative balance caused by the aerosols, it cannot be directly translated into surface temperature changes because it does not include the additional longwave radiation that is retained by a warmer stratosphere, which negates part of the cooling produced by aerosol scattering.

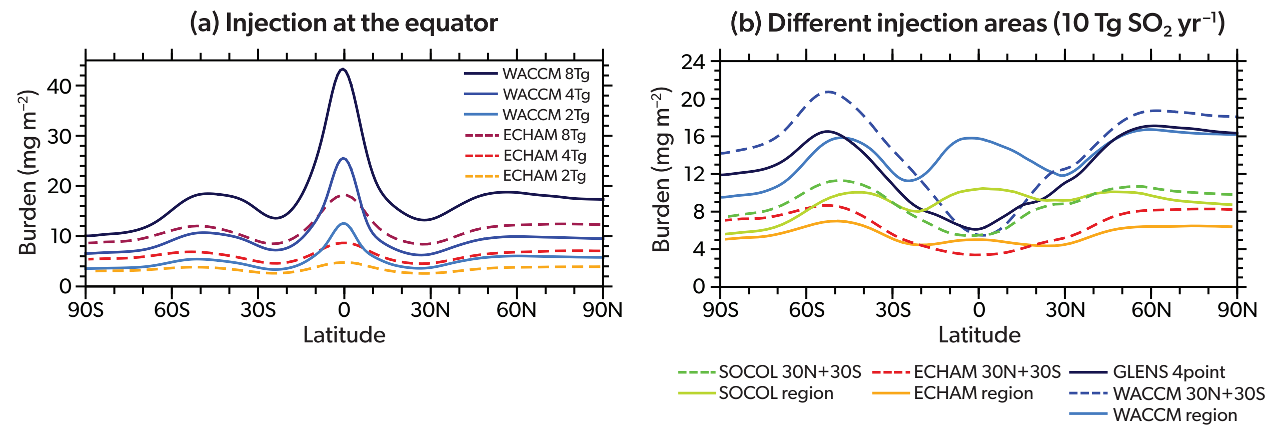

Figure 6-7. (a) Zonally averaged sulfur burden in two different models for three different injection rates, for runs where SO_2 was injected continuously into one grid box at the equator (after Niemeier et al., 2020). (b) Zonally averaged sulfate burden in three different models with 10 Tg SO_2 yr^{-1} injections employing three different strategies: 2 grid boxes at 30°N and 30°S, a belt between 30°N and 30°S along the equator (region; after Weisenstein et al., 2022), and at four different grid points: 30°N, 15°N, 15°S, 30°S (GLENS four-point; after Tilmes et al., 2018a).

strategies result in different spatial aerosol distributions and particle sizes and consequently cause different impacts on climate and ozone. The following subsections give an overview of the sensitivity of the aerosol distribution to SAI injection strategy using GCMs coupled to aerosol microphysical modules and using fixed sea surface temperatures (SST). These studies used continuous or pulsed injections of a constant mass rate (Tg yr^{-1}) at different altitudes and locations. Consequences for the impact on ozone are given in *Section 6.3.2* and **Table 6-2**.

6.2.3.1 Sensitivity to Increasing Injection Rates

Increasing injection rates result in a sublinear increase of the globally averaged sulfate aerosol burden (i.e., diminishing returns), as shown in **Figure 6-6a**. The four models agree quite well on the factor of increase (times ~1.8 for a doubling of the injection rate). Comparing the instantaneous radiative forcing (IRF) of four different studies shows a much wider spread in the model results (**Figure 6-6b**). The IRF efficiency (forcing gain per injected mass unit) ranges between −0.09 and −0.26 W m^{-2} per Tg SO_2 yr^{-1} for an injection of 20 Tg SO_2 yr^{-1}. The resulting forcing of 20 Tg SO_2 yr^{-1} would therefore be between −1.8 and −5.2 W m^{-2}, which shows that the forcing produced by a given injected mass of sulfur is currently very uncertain.

The models consistently show that the forcing efficiency decreases exponentially with increasing injection rate (Niemeier and Timmreck, 2015); e.g., quadrupling the injection of the most efficient model from 10 to 40 Tg SO_2 yr^{-1} decreases the forcing per unit mass from 0.33 to 0.2 W m^{-2} per Tg SO_2 yr^{-1}. This behavior results from the increase in particle size with increasing injection rate (*Section 6.2.1.1*), producing aerosols with a less optimal size for scattering sunlight, increased absorption of terrestrial radiation, and a greater sedimentation rate through the tropopause and therefore reduced effectiveness (Heckendorn et al., 2009; Pierce et al., 2010; English et al., 2012; Niemeier and Timmreck, 2015). One main reason for the larger differences between aerosol forcing and mass is the difference in simulated particle sizes in models, as shown by the light blue curves in **Figure 6-6a** and **b**, simulated with the same GCM, but different microphysical parameterizations. Diminishing returns may have important consequences that influence the efficacy of any SAI strategy: to offset more forcing, relatively more injected mass is needed, producing more heating in the tropical stratosphere with larger impacts on stratospheric ozone and climate.

6.2.3.2 Sensitivity to Injection Altitude

Several studies have shown that the cooling efficiency of stratospheric aerosols is larger for injections into tropical regions at altitudes well above the tropopause (around 25 km or 30 hPa in tropical regions) than at lower altitudes closer to the tropopause (around 20 km or 75 hPa; e.g., Jones et al., 2017; Niemeier and Timmreck, 2015; Tilmes et al., 2017, 2018b). This is because injection at higher altitudes prevents the fast removal of aerosols and their precursors, and it allow aerosols to reach even higher altitudes through the vertical updraft of the BDC. For tropical injections, the global sulfate burden increases by 30–50% when the injection altitude is increased by 5 km (**Figure 6-6a**). However, this is not true for all SAI injection strategies such as injections outside the tropics (Niemeier and Schmidt, 2017; Laakso et al., 2022; see **Table 6-1** for altitude dependency), because the injection location influences the simulated meridional distribution of the aerosols, which also depends on the injection amount. Injections at higher altitudes may be more efficient in terms of radiative forcing but are not necessarily more desirable for ozone. High-altitude injections have a larger impact on ozone via the catalytic nitrogen cycle, which dominates in the middle stratosphere. With lower altitude injections, a more concentrated aerosol distribution closer to the tropopause results in stronger heating in the tropical stratosphere, with consequences for transport and stratospheric water vapor changes (Tilmes et al., 2018b).

6.2.3.3 Dependency on Injection Latitude for Point Injections

The globally averaged sulfur burden is maximized for aerosol injections in the inner tropics (i.e. in the vicinity of the equator)

Table 6-1. Estimates of globally averaged top-of-the-atmosphere sulfate radiative forcing from different studies. The results are grouped based on whether the studies focused on responses to injection at specific altitudes, longitudinal areas, or a zonal area, the use of regional and point injections, pulsed injections, and the use of stable injections versus a feedback control strategy. Injection rates refer to the total stratospheric injections per year.

Study	Injection rate (Tg S yr^{-1})		W m^{-2}	W m^{-2}	W m^{-2}	Net (SW+LW) or SW only
Altitude			**Low (<20km)**	**Middle (~20km)**	**High (>20km)**	
Kleinschmitt et al., 2018	10	one-lon, 2° N – 0° S	–1.5	–1.8	–1.5	Net (SW+LW)
Laakso et al., 2022	5	band, 10° N – 10° S, sectional aer. model	–3.26	–3.29	–3.79	Net (SW+LW)
Laakso et al., 2022	5	band, 10° N – 10° S, modal aer. model	–1.75	–1.33	–1.59	Net (SW+LW)
Niemeier and Timmreck, 2015	10	one-lon, 2.8° N to Eq	–2.03		–3.02	Net (SW+LW)
Niemeier and Timmreck, 2015	10	one-lon, 30° N to 30° S	–1.81		–2.76	Net (SW+LW)
Niemeier and Schmidt, 2017	10	one-lon, 2.8° N to Eq	–1.78		–1.92	Net (SW+LW)
Vattioni et al., 2019	1.87	band, 15° N – 15° S, 20 km	–0.96		–1.22	SW
Longitudinal area			Narrow (<10°)	Middle	Broad (>50°)	
Kleinschmitt et al., 2018	10	one-lon	–1.5		–1.5	Net (SW+LW)
Laakso et al., 2022	5	band, sectional model	–3.81	–3.29	–3.09	Net (SW+LW)
Laakso et al., 2022	5	band, modal model	–1.21	–1.33	–1.53	Net (SW+LW)
Niemeier and Timmreck, 2015	10	one-lon	–2.03	–2.06	–1.81	Net (SW+LW)
Vattioni et al., 2019	1.87	band	–0.96	–0.93	–1.00	SW
Zonal area			**One-lon**	**Band over longitudes**		
Laakso et al., 2022	5	2° N – 2° S, 21 km, sectional aer. model	–4.13	–3.81		Net (SW+LW)
Laakso et al., 2022	5	2° N – 2° S, 21 km, modal aer. model	–1.96	–1.21		Net (SW+LW)
Niemeier and Timmreck, 2015	10	2.8° N to 0°, 19 km	–2.03	–1.79		Net (SW+LW)
Vattioni et al., 2019	1.87	3.75° N – 3.75° S, 20 km	–1.51	–0.96		SW
Regional / point injections		**(30° S – 30° N, band) / (30° S and 30° N one-lon)**	**Region**	**2-model grid points**		
Weisenstein et al., 2022	5	Model: CESM2(WACCM)	–2.4	–2.2		Net (SW+LW)
Weisenstein et al., 2022	5	Model: MAECHAM5-HAM	–0.8	–1.1		Net (SW+LW)
Weisenstein et al., 2022	5	Model: SOCOL-AER	–1.6	–1.7		Net (SW+LW)
Pulsed			**Low rate (2 yr^{-1})**	**High rate (≥6 yr^{-1})**	**Continuous**	
Kleinschmitt et al., 2018	10	one-lon, 2° N – 0° S, 17 km	–1.6		–1.5	Net (SW+LW)
Laakso et al., 2022	5	band, 10° N – 10° S, sectional model	–4.36	–3.58	–3.29	Net (SW+LW)
Laakso et al., 2022	5	band, 10° N – 10° S, modal model	–2.08	–1.36	–1.33	Net (SW+LW)
Heckendorn et al., 2009	5	band, 5° N – 5° S, 20 km	–1.64	–1.29	–1.06	SW
Vattioni et al., 2019	1.87	10° N – 10° S, 20 km	–1.51		–0.96	SW
Stable injections / Feedback-control strategy (GLENS)			**Region**	**GLENS**		
(Weisenstein et al., 2022 /	5	30° S – 30° N, band / Feedback-control	–2.4	–2.16		Net (SW+LW)
Tilmes et al., 2018b (GLENS))	25	30° S – 30° N, band / Feedback-control	–7.1	–7.21		Net (SW+LW)

(Jones et al., 2017; Niemeier and Schmidt, 2017; Tilmes et al., 2018b; Franke et al., 2021). However, this might not be the optimal injection strategy because the tropical confinement of the aerosols causes a local burden maximum in the tropics (**Figure 6-7a**). Injections outside the inner tropics have been simulated in recent studies targeting changes beyond global mean surface temperature, including pole-to-equator and inter-hemispheric temperature gradients (e.g., Kravitz et al., 2017). **Figure 6-7b** shows results of simultaneous two point-like injections at 30°N and 30°S of a total of 10 Tg SO_2 yr^{-1} (Franke et al., 2021; Weisenstein et al., 2022). The injection outside of the subtropical transport barrier reduces the sulfate aerosol transport into the tropics and therefore results in a minimum aerosol burden in the tropics (**Figure 6-7b**). The global coverage of the aerosols is more homogenous for injections in the outer tropics, and this reduces tropical heating of the sulfate aerosols due to less equatorial confinement (Kravitz et al., 2019). Consequently, surface cooling is spatially more even, and the increase of stratospheric water vapor, as well as the impact on the QBO, are reduced (Aquila et al., 2014; Niemeier and Schmidt, 2017; Richter et al., 2017; Franke et al., 2021).

6.2.3.4 Dependency on Single Points / Regional Injections (Area)

Whether the injection of sulfur is concentrated in one area or distributed across different locations plays a crucial role for the simulated burden and radiative forcing. Injections into a larger region, between 30°S and 30°N and over all longitudes (solid lines in **Figure 6-7b**), still produce a peak in the aerosol column burden over the equator, but the peak is smaller than for injections at one grid point at the equator (**Figure 6-7a**). Many models (Heckendorn et al., 2009; Niemeier and Timmreck, 2015; Vattioni et al., 2019; Laakso et al., 2022) agree that injections into one grid point in the inner tropics result in less coagulation and therefore smaller particles than injections into multiple grid points, either along the equator (see "zonal area" group of studies in **Table 6-1**) or over multiple latitudes toward the extratropics ("longitudinal area" group of studies in **Table 6-1**). This results in slower removal (i.e., larger burden) and larger radiative forcing. However, the impact of widening the injection area latitudinally is not consistent across models, with disagreements on what is the most effective approach. This is because of inconsistencies in the injection locations among simulations or differences in representing stratospheric dynamical processes (e.g., the QBO) across models.

6.2.3.5 Dependency of Injection Timing

Studies agree that pulsed injections into the tropics, e.g., injections over one month twice a year, result in stronger radiative forcing per injected mass than continuous injections (see "pulsed" group of model runs in **Table 6-1**). Continuous sulfur injections lead to a continuous formation of sulfuric acid (H_2SO_4) and a continuous supply of freshly nucleated small particles (Heckendorn et al., 2009). These coagulate with larger particles, leading to the quicker formation of large particles and a shift of the aerosol size distribution to larger effective radii. Aerosols that grow to larger than the optimal optical size (*Section 6.2.1.3*) scatter sunlight less efficiently and are removed faster from the stratosphere owing to higher sedimentation rates. Pulsed injections reduce the formation of freshly nucleated small particles to a short period in time, consequently forming an aerosol size distribution with smaller effective radii. These processes also explain the higher efficiency in terms of radiative forcing per injected mass for single grid point injections compared to injections along several longitudes.

SAI aims to reduce incoming solar radiation, which is the largest for overhead sun and is dependent on the length of day. Injecting into the region where the sun reaches the zenith can lead to stronger radiative forcing at mid-latitudes and weaker radiative forcing in the tropics. This may result in a 5–60% stronger global mean forcing per emitted mass (Laakso et al., 2017, 2022). Visioni et al. (2019) found that injections at 15° latitude in the spring of the corresponding hemisphere result in the largest reductions in incoming solar radiation per mass injected.

6.2.3.6 Gaseous Versus Particulate Injection

Aerosol mass and size distributions with SAI are also dependent on whether the SAI strategy prescribes the injection of accumulation-mode H_2SO_4 aerosol or gas-phase SO_2 (Vattioni et al., 2019; Franke et al., 2021; Weisenstein et al., 2022). Increasing the rate of SO_2 injections increases particle size, which, as noted above, decreases stratospheric aerosol lifetime and radiative forcing efficiency (*Section 6.2.3.1*). This problem could be combated by directly injecting optimally sized accumulation-mode particles. It has been suggested that if H_2SO_4 or SO_3 (sulfur trioxide) vapor are were released into an aircraft wake, nucleation and coagulation in the confined plume would result in a distribution of sulfate particles in the accumulation size range (0.05–0.2 μm radius; Pierce et al., 2010; Benduhn et al., 2016; Vattioni et al., 2019). Due to their coarse horizontal resolution, GCMs are not able to simulate the rapid initial formation of accumulation-mode sulfate particles after the injection of H_2SO_4 vapor. Therefore, in these simulations the injection of H_2SO_4 is modeled as direct injection of SO_4 (sulfate) aerosol into the accumulation mode (Vattioni et al., 2019). Results from three GCMs consistently show a higher aerosol burden and smaller particle sizes for injections of accumulation-mode SO_4 compared to SO_2 considering different injection strategies and models (Weisenstein et al., 2022). The higher aerosol concentration causes a stronger impact on stratospheric dynamics, but less H_2SO_4 injection would be necessary to achieve the same climate impact. All three models show a reduced increase in particle size with increased injection rate if using accumulation-mode SO_4 injections.

6.2.4 Summary of SAI Processes and Model Uncertainties

Many processes that determine the effects of SAI on both the climate and ozone are often simplified or missing from climate models. This includes the coupling of chemistry, aerosols, and radiation, as well as aerosol microphysical processes. Simplified, and therefore computationally cheaper, aerosol schemes are used for centennial simulations in ESMs. A more detailed representation of the life cycle of sulfate would require computationally expensive sectional microphysical modules. In addition, the grid resolution of current global models is far too coarse to simulate processes that take place right after an injection from a small pipe of an aircraft or other delivery system; instead, injections are assumed to occur uniformly into one model grid box. An additional shortcoming is the representation of aerosol-cloud interactions, in particular the impact of the injected material on cirrus clouds.

Besides differences in physical processes, another major reason for the disagreement across models in simulated aerosol burden and radiative forcing is the different representation of large-scale dynamic processes in the stratosphere. For example, different horizontal and vertical grid resolutions result in different grid-box mean vertical velocities within the models, even without SAI. Those differences, in addition to specifics of the aerosol microphysics schemes in the model, result in different aerosol size distributions, which induce different amounts of heating, vertical lifting, and sedimentation. Consequently, the models react differently to the varying injection strategies.

Despite these uncertainties, the models consistently show that increasing injection rates result in diminishing returns for both aerosol burden and radiative forcing, as well as an exponential decrease in radiative forcing efficiency. There is also general agreement that the global coverage of the aerosols is more homogenous for injections outside of the immediate equatorial band than for injections close to the equator. Nevertheless, there is poor agreement between the models on the amount of sulfur needed to achieve cooling of the Earth's global mean temperature by 1 °C. This relates both to the SAI-induced radiative forcing response in models and to differences in the climate sensitivity of

ECMs, which strongly influence the simulated global mean temperature change under climate scenarios without SAI (see also **Figure 6-1**).

6.3 IMPACTS OF SAI USING SULFATE ON STRATOSPHERIC OZONE, CHEMISTRY, TRANSPORT

In this section, we assess the relevant processes driving SAI impacts on ozone. We identify differences in the impacts of SAI (using sulfate, or its precursors) on stratospheric ozone under specific SAI strategies (*Section 6.1.3*) as projected in recent climate modeling studies. Here, the effects of SAI on stratospheric ozone are mostly based on comparisons of simulations with and without SAI.

6.3.1 Effects of SAI on Stratospheric Chemistry

As evidenced from explosive volcanic eruptions (e.g., Solomon, 1999), enhancements of the stratospheric sulfate aerosol layer from continuous SAI would result in elevated aerosol surface area density (SAD), which directly influences chemical production and loss of stratospheric ozone through heterogeneous reactions and their impact on catalytic ozone cycles (**Figure 6-8**, middle row). The SAD amounts and geographic distributions depend on the details of the injection strategy, including altitude above the tropopause, latitudinal injection location, and the seasonality of injections (*Section 6.2*).

One effect of enhanced stratospheric SAD is increased nitrogen pentoxide (N_2O_5) hydrolysis at the interface of the liquid acidic sulfate particles, resulting in the production of nitric acid (HNO_3): ($N_2O_5 + H_2O_{(aq)} \longrightarrow 2\ HNO_3$). HNO_3 is a low-reactive nitrogen reservoir; therefore, the increase of HNO_3 at the expense of nitrogen oxides reduces the catalytic ozone loss cycles (Fahey et al., 1993). The reactive nitrogen cycle is most important in the mid- and upper stratosphere (altitudes above 30 hPa; **Figure 6-8**, top row). The strongest reductions in ozone loss rates based on this cycle are therefore simulated for the upper part of the aerosol layer (with a peak around 15 hPa in the tropics; e.g., Tilmes et al., 2017). These effects are present at all latitudes, with the largest importance in the tropical and mid-latitude stratosphere. Ozone loss rates from the reactive nitrogen cycle are reduced the most for high-altitude injection (**Figure 6-8**, green dashed versus solid lines).

In the lower stratosphere, ozone loss cycles involving the reactive chlorine (ClO_x), bromine (BrO_x), and hydrogen (HO_x) families are most important. An enhanced stratospheric SAD results in the activation of halogens from reservoir species such as chlorine nitrate ($ClONO_2$) and hydrogen chloride (HCl) to chlorinated species such as chlorine (Cl_2) and hypochlorous acid (HOCl) via reactions such as $ClONO_2 + H_2O \longrightarrow HOCl + HNO_3$, $ClONO_2 + HCl \longrightarrow Cl_2 + HNO_3$, and $HOCl + HCl \longrightarrow Cl_2 + H_2O$. In the presence of sunlight, Cl_2 and HOCl photolyze rapidly to form reactive halogen species that drive catalytic ozone-destroying reactions. Reactions with nitrogen dioxide (NO_2) convert halogen and hydrogen radicals back into reservoir species. Thus, the combined effect of activating halogens and reducing NO_2 results in increased ozone loss via the halogen and HO_x catalytic ozone loss cycles as a result of increased stratospheric SAD (Drdla and Mueller, 2012). These processes are most effective at temperatures lower than 200 K and are thus most efficient in the polar regions.

The ozone loss cycles described above are strongly dependent on the halogen and nitrogen loading in the atmosphere. Chlorine and bromine cycles are expected to be reduced with the projected future decline in halocarbon atmospheric abundances, and hence the role of these cycles in stratospheric ozone loss is expected to decrease. On the other hand, nitrous oxide (N_2O) may become the dominant ozone-depleting substance in the future (Ravishankara et al., 2009). The net effect of increased stratospheric SAD on the ozone column will depend on the balance of decreased net chemical production from hydrogen and halogen catalytic cycles versus the increased net chemical production from nitrogen oxide catalytic cycles (e.g., Xia et al., 2017). The altitude dependence of the importance of these cycles could result in changes in the vertical distribution of ozone even with small overall changes in the ozone column (Heckendorn et al., 2009 Tilmes et al., 2017).

Ozone loss cycles involving hydrogen oxide radicals (HO_x) are important in both the lower and the upper stratosphere. Changes in the hydrogen cycles would be influenced not only by changes in NO_x but also by SAI-induced changes to stratospheric water vapor (Richter et al., 2018; Tilmes et al., 2018b; Visioni et al., 2021b). This increase occurs due to the warming of the lower stratosphere and tropical tropopause layer (TTL) by the aerosols (see *Section 6.2.2.1*) and leads to an increase of HO_x ozone loss cycles through the reaction $H_2O + O(^1D) \longrightarrow 2OH$. A secondary pathway for SAI to increase water vapor in the stratosphere is through an increase of the stratospheric methane lifetime and concentrations due to an increase in the transport of methane in the mid-stratosphere due to enhanced upwelling (Visioni et al., 2017b). Water vapor increases are greater with injections at low altitudes than at high altitudes because the former lead to more concentrated sulfate mass closer to the tropopause and therefore enhanced heating of the tropopause, which leads to reduced dehydration in the TTL (Tilmes et al., 2017). Finally, the reactive oxygen cycles would also be perturbed in the tropical region due to changes in the air temperature from SAI, but this would produce a minor loss in ozone compared to other cycles. Combined net chemical ozone production rates show an increase most pronounced in the mid-stratosphere tropics, and a decrease in the lower stratosphere, particularly at high latitudes, as well as in the upper stratosphere (**Figure 6-8**, right middle panel).

At mid-latitudes, Robrecht et al. (2021) explored the importance of a possible pathway through which increasing water vapor in the lowermost stratosphere during the North American summer monsoon season may increase ozone loss if conditions are cold and moist enough. As SAI would both warm and add water vapor to the layer where chlorine activation may happen, they found that less than 0.3% of ozone may be depleted through that pathway.

6.3.2 Effects of SAI on Ozone Via Changes in Stratospheric Dynamics and Transport

6.3.2.1 Large-Scale Impacts

In addition to the direct chemical effects produced by the increased SAD, an enhanced sulfate layer would also affect ozone through transport changes. These changes are predominantly

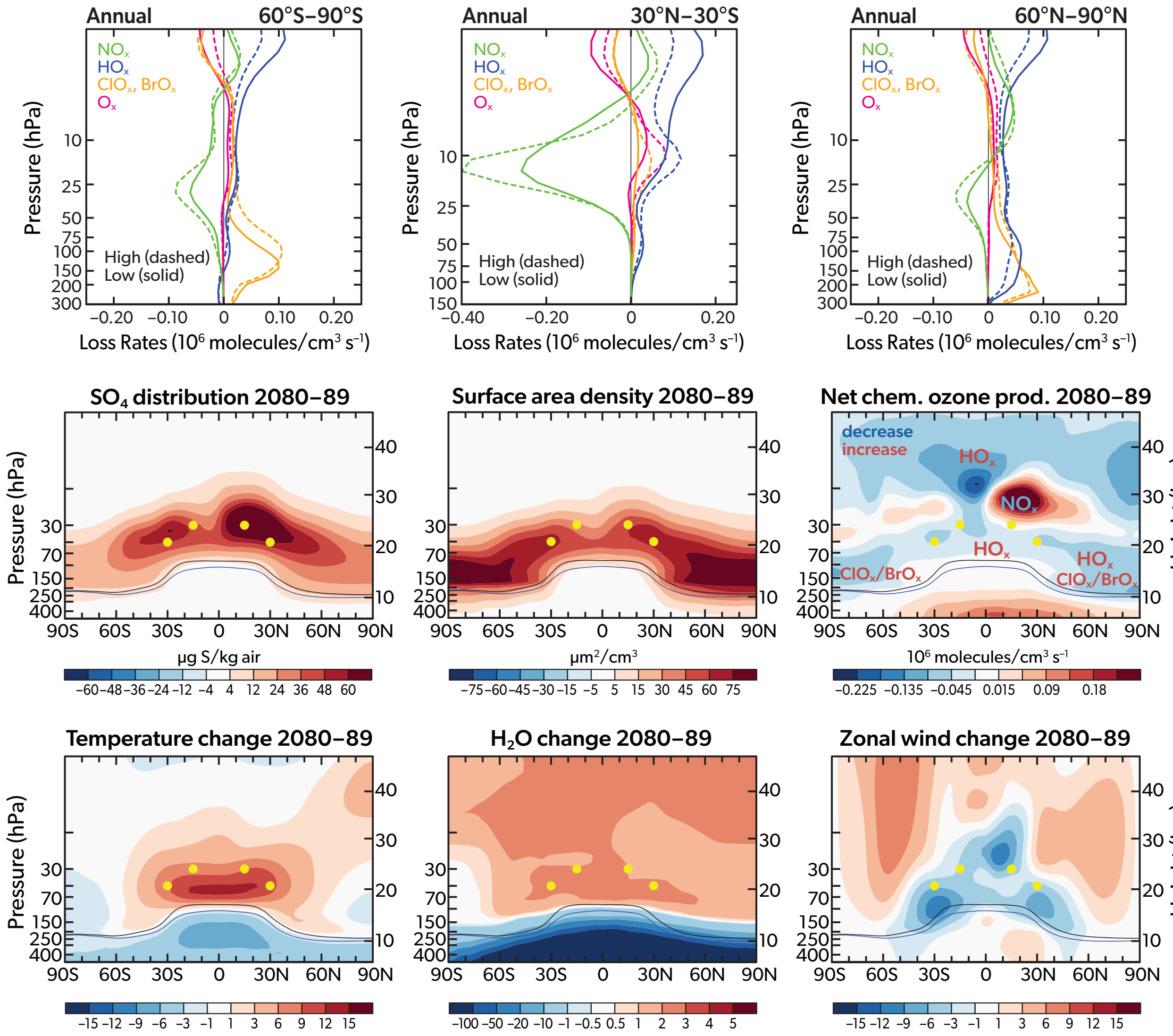

Figure 6-8. *(top row)* Chemical loss rates through different ozone loss cycles in two different SO_2 injection simulations relative to a baseline simulation without SO_2 injection. Values are annual averages of values between 30°N and 30°S and for the period 2042–2049 for a high-altitude injection case—"High (dashed)"—injecting 24 Tg SO_2 yr^{-1} at 30 hPa (~25 km altitude) and a low-altitude injection case—"Low (solid)"—injecting 32 Tg SO_2 yr^{-1} at 70 hPa (between 19 and 20 km altitude), with annual injections divided equally between 15°N and 15°S. The three panels show, from left to right, the latitudinal bands 60–90°S, 30°N–30°S, and 60–90°N. *(middle and bottom rows)* Differences between the ensemble average of an SAI scenario in the GLENS modeling study for the period 2080–2089 and the control (RCP8.5) for the same period for zonally and annually averaged quantities: sulfate burden *(middle left)*, aerosol surface area density *(middle center)*, net chemical ozone production rate *(middle right)*, temperature *(bottom left)*, water vapor *(bottom center)*, and zonal wind *(bottom right)*. The lapse rate tropopause is indicated as a black line for the control and a blue line for the SO_2 injection cases. Yellow dots indicate injection locations. [From Tilmes et al., 2021.]

induced by two processes: the heating of the tropical lower stratosphere and the cooling of the surface caused by the reduced incoming shortwave radiation. The magnitude of this lower-stratospheric heating depends on the sulfate mass and therefore the amount of sulfate injected. It is somewhat dependent on the latitudinal aerosol distribution, which is determined by the injection strategy (e.g., Richter et al., 2017). For example, in simulations using CESM1 (WACCM), equatorial injections have been shown to result in larger tropical stratospheric heating compared to injections outside the equator (Kravitz et al., 2019), and low-altitude injections have been shown to heat the tropopause more than high-altitude injections (Tilmes et al., 2017). The effect of SAI on stratospheric temperature anomalies in the tropical lower stratosphere shows a quasi-linear relationship to aerosol optical depth (AOD; **Figure 6-9**). Models show a large spread in the stratospheric warming produced by aerosols: an increased optical depth of 0.1 results in a warming of 2.8 ± 1.6 °C (range between 0.8 and 4.9 °C for the G6sulfur runs done with GeoMIP models and in runs with CESM1(WACCM) in the GLENS simulations. This translates into an approximate tropical lower-stratospheric temperature increase of 4.6 ± 2.7 °C per degree of surface cooling achieved through SAI. This range in stratospheric warming may arise not only from differences in the simulated size distributions but also from different radiative approaches across models, as well as from differences in the radiative effects of affected chemical species such as ozone and water vapor (Visioni et al., 2021b).

Several robust effects have been identified to result from SAI-induced stratospheric heating (**Figure 6-9**). The updraft in the tropics is reduced below the injection locations and increased above the injection locations (Pitari et al., 2014; Tilmes et al., 2017; Franke et al., 2021). The reduced updraft of ozone-poor air from the troposphere below the injection location drives an increase in ozone in the lower tropical stratosphere (Tilmes et al., 2009). The resulting decrease in the temperature gradient between the tropics and mid-latitudes above the subtropical jet produces a weakening in the subtropical jets and a weakening of the Eliassen-Palm (EP) flux divergence (which is caused by changes in large-scale planetary waves) at the top the subtropical jets (Tilmes et al., 2017; Franke et al., 2021). These changes are expected consequences of a weakening of the Hadley cell and a reduction in residual vertical velocity (w*) below the injection altitude. The simulated increase in momentum deposition in the middle and high latitudes is in accordance with the acceleration of the BDC and the strengthening of the polar jet streams in winter and spring of each hemisphere. A cooler polar vortex is expected to increase heterogeneous reactions and therefore ozone depletion.

The stratospheric heating perturbation and resulting effects depend on the horizontal and vertical extent of the aerosol layer and on details of the aerosol distribution (e.g., Richter et al., 2017; Tilmes et al., 2017). For example, injections at higher altitudes result in a stronger and cooler polar vortex than injections at lower altitudes, but there is a greater increase in horizontal transport

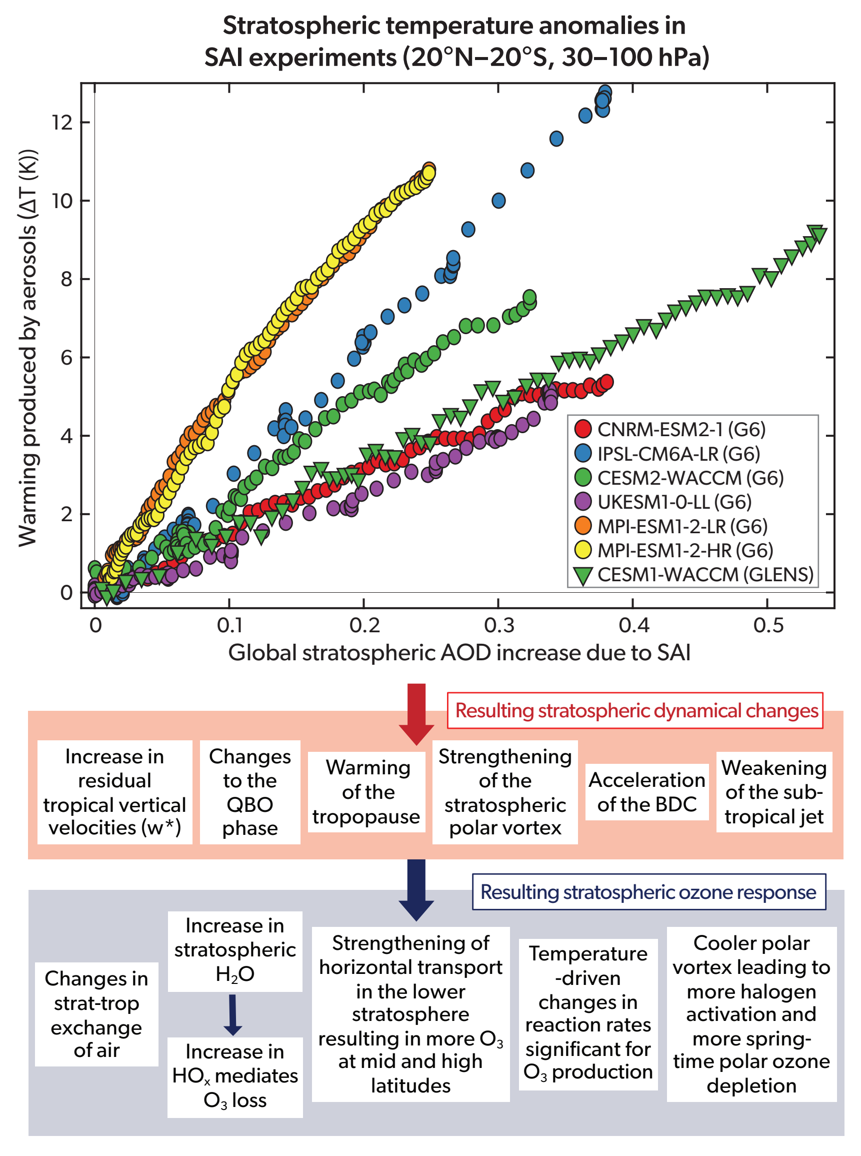

Figure 6-9. *(top)* Dependence of stratospheric temperature anomalies on an increase in global stratospheric AOD produced by the injection of sulfate, from simulations across different models. For all simulations, stratospheric AOD is calculated as a global annual mean, and stratospheric temperature anomalies are annual means calculated between 20°N and 20°S and between 30 and 100 hPa. Both values are the difference between the SAI experiment and the baseline experiment with the same GHG emissions. Circles represent differences between the G6sulfur and SSP5-8.5 simulations (Visioni et al., 2021a), and triangles represent differences between the GLENS SAI and RCP8.5 simulations (Tilmes et al., 2018a). A five-year running mean has been applied to the values. *(middle)* Dynamical changes in the stratosphere resulting from stratospheric heating. *(bottom)* Changes in ozone produced as a direct or indirect consequence of stratospheric heating.

from the tropics to the high latitudes in the low-altitude injection case. Furthermore, equatorial injections have been shown to result in larger tropical stratospheric heating than extra-equatorial injections (Kravitz et al., 2019).

6.3.2.2 Effects on the Quasi-Biennial Oscillation

The heating of the lower stratosphere caused by SAI would modify the thermal heat balance and produce a stronger residual vertical advection of zonal momentum. The changes in stratospheric temperature consequently modify zonal winds, and this effect weakens the downwelling propagation of winds in the Quasi-Biennial Oscillation (QBO) and ultimately lead to a prolonged westerly phase of the QBO (Franke et al., 2021). This effect would be relevant for ozone, as the QBO phase influences the stratospheric transport of chemical species (Niemeier and Schmidt, 2017). This mechanism, first theorized by Aquila et al. (2014), has been further confirmed in successive studies (Jones et al., 2016a; Niemeier et al., 2020; Franke et al., 2021; Jones et al., 2021, 2022) for equatorial injections. However, the simulated magnitude of the changes to the QBO period depends on the amount of injection, with notable inter-model differences: for instance, simulations with CESM1(WACCM) required only 4 Tg S yr^{-1} to lock the QBO in a permanent westerly phase, whereas twice as much was needed in simulations with the ECHAM model (Niemeier et al., 2020).

A recent assessment of six of the models participating in the GeoMIP G6sulfur experiment shows significant variability in the fidelity of the representation of the QBO even without SAI perturbations. It also shows a large model range in the amount of SO_2 injection at which the QBO phase becomes locked in a permanent westerly phase (Jones et al., 2022). The impact of equatorial injections of stratospheric aerosols is strongly dependent on the degree of aerosol absorption and hence stratospheric heating rates (Jones et al., 2016a; Haywood et al., 2022). However, for injections poleward of the inner tropics, which results in less localized tropical stratospheric heating, multiple models have simulated minor or no disruption of the QBO phase (Richter et al., 2017, 2018; Kravitz et al., 2019; Franke et al., 2021). Inter-model differences in the projections of the QBO behavior therefore strongly depend on model specifics: increasing the model vertical and horizontal resolution results in stronger tropical confinement of air masses, which impacts the simulated QBO phase (Niemeier et al., 2020). In addition, differences in the description of chemistry matters. SAI simulations with interactive ozone result in reduced stratospheric ozone production compared to simulations with fixed ozone. The resulting differences in the longwave and shortwave heating impact the QBO differently, which is assumed to be the reason for mainly westerly jets in a simulation with fixed ozone, and easterly jets in a simulation with interactive ozone (Richter et al., 2017; Franke et al., 2021). Changes in the QBO can also impact the transport of ozone, as a westerly phase of the QBO is associated with increased tropical confinement of air in the stratosphere (Niemeier and Schmidt, 2017). The importance

Table 6-2. Summary of different injection parameters that affect ozone changes in the stratosphere. All rows except the first discuss differences based on the injection of the same quantity of material.

Injection Details	Summary of Findings	Implications for Ozone
Sensitivity to increasing injection rates	Increasing sulfur dioxide (SO_2) injection rates lead to a sublinear increase of the aerosol burden due to the microphysical growth of the resulting aerosol particles. Dynamical changes from differences in stratospheric heating also contribute to nonlinear changes in transport (Kravitz et al., 2019).	Small injections are more efficient at increasing SAD than larger ones and therefore have a relatively stronger impact on ozone. The start of SAI can lead to an abrupt decrease in Southern Hemisphere (SH) polar ozone (Tilmes et al., 2021). Larger injections increase aerosol size and the heating of the tropical lower stratosphere and induce stronger effects on dynamics.
Sensitivity to injection altitudes	Injections at higher altitudes in general result in a higher aerosol burden and are therefore more efficient in terms of producing surface cooling. Lower-altitude applications may require significantly more mass to be injected. However, in some cases additional factors may cause the opposite result (see **Table 6-1**).	Injections at lower altitudes within the stratosphere result in stronger stratospheric heating and a greater water vapor increase than high-altitude injections. Transport changes from the equator to the poles are stronger for low-altitude injection cases, resulting in an increase of ozone in high latitudes in winter (Tilmes et al., 2017, 2021).
Sensitivity to single versus multiple injection points	Longitudinal band injections result in larger particles and reduce the aerosol burden and therefore the efficiency of SAI compared to point injections (*Section 6.2.3.4*). Effects on aerosol burden of distributing the injection across a broader latitudinal area are mixed across models.	Smaller particles with point injections result in larger SAD with stronger ozone depletion compared to regional or longitudinal band injections. However, other factors, including changes in aerosol mass and resulting dynamical changes, can result in an increase in ozone, which is model dependent and can also depend on the injection material (**Figure 6-11**).
Sensitivity to the injection latitude	Injections in the tropics, but away from the equator (i.e., 15°N/S) have higher forcing efficiency than injections at the equator and can result in more spatially uniform surface cooling and fewer side effects.	Equatorial injections lead to enhanced stratospheric heating and therefore a greater water vapor increase and a stronger SH polar vortex (Visioni et al., 2020b). This results in larger polar ozone depletion than for injections away from the equator (Tilmes et al., 2021).
Gaseous versus particulate injection	Sulfuric acid (H_2SO_4) injections increase the radiative efficacy, defined as the radiative forcing per unit of sulfur injection, relative to SO_2 injection. This is due to the production of smaller particles that scatter light more efficiently and have a longer lifetime.	H_2SO_4 injections lead to a very similar pattern of ozone impact as SO_2 injections. However, ozone depletion is 10–20% greater using H_2SO_4 due to larger sulfate aerosol burdens, smaller mean particle size, and consequently larger SAD throughout the stratosphere (Weisenstein et al., 2022). The need for a smaller injection mass to obtain a similar amount of radiative forcing may offset this, which means that for a given forcing, the two may have similar ozone impacts.
Sensitivity to injection timing	Pulse injections or selected seasonal injections improve the efficiency of SO_2 injections.	An increased SAD burden during spring would result in larger ozone depletion at high latitudes. On the other hand, the need for a smaller injected mass to obtain a similar amount of radiative forcing results in fewer changes to ozone (Visioni et al., 2019; Visioni et al., 2020a). The start date of SAI matters for ozone, due to the projected changes in the halogen and nitrogen content in the future, which influence ozone loss.

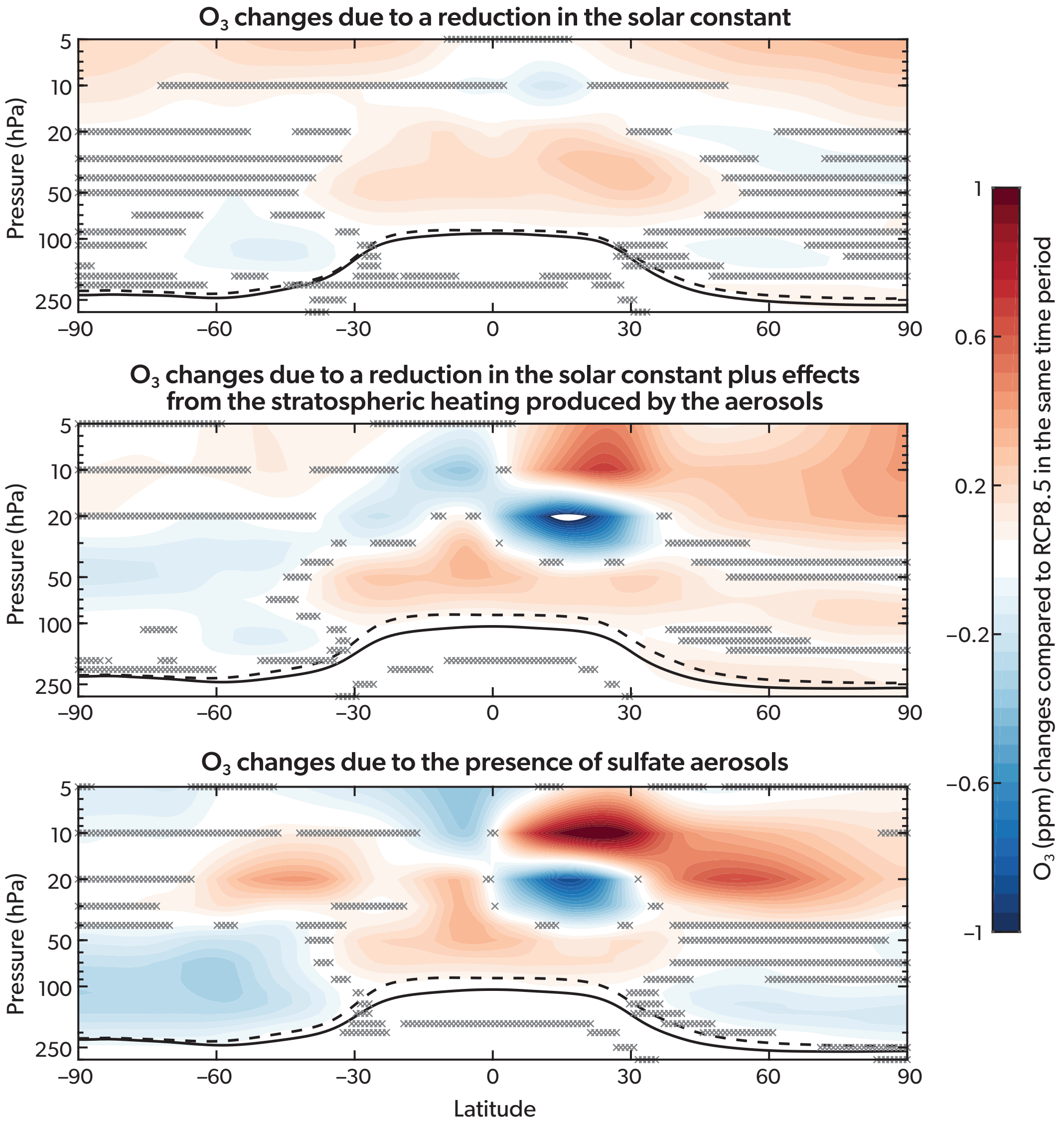

Figure 6-10. *(top)* Ozone concentration changes due to a reduction of the solar constant required to reduce the global, annual average surface temperature from that in the RCP8.5 scenario in the 2070–2090 period to that in the 2010–2030 period. *(middle)* Ozone concentration changes due to a reduction of the solar constant and an imposed stratospheric heating equivalent to that which would be produced by the aerosols in the simulations shown in the bottom panel. *(bottom)* Ozone concentration changes due to an increase in stratospheric sulfate aerosols at a concentration required to reduce the global, annual average surface temperature from that under the RCP8.5 scenario in the 2070–2090 period to that in the 2010–2030 period. The dashed black lines represent the tropopause height in RCP8.5 (2070–2090), and the continuous black lines represent the tropopause height in the geoengineering experiment. Hatched areas indicate regions where the differences are not statistically different from zero. [Adapted from Visioni et al., 2021b.]

of these effects depends on specifics of the injection locations and the potential breakdown of the QBO (Jones et al., 2022).

6.3.3 Combined Effects of Chemistry and Dynamical Changes with SAI on Stratospheric Ozone

Combined changes in chemical production rates, vertical and horizontal transport, and circulation influence the overall changes of stratospheric ozone concentration and therefore total column ozone (TCO). As outlined above and in *Sections 6.2.1* and *6.2.2*, changes in transport are more strongly influenced by the spatial distribution of sulfate mass, while chemical changes are more strongly influenced by the distribution of aerosol surface area density. Both depend on the details of the injection strategy and may scale differently (for instance, depending on latitude) with the injection amount (*Section 6.2*). In general, in the SH polar regions, ozone is largely controlled by chemical changes, particularly during winter and spring, resulting in reductions in ozone. Chemical changes are also important in the upper tropical stratosphere and mid-latitudes as a result of the reduced reactive nitrogen cycle.

Contrasting ozone changes across simulations that include different processes reveal the importance of the effects of sulfate aerosols on chemistry and transport. In **Figure 6-10**, changes in ozone are contrasted in three different model experiments. The first experiment is a simulation with solar dimming only (top panel), the second includes solar dimming and an imposed stratospheric heating effect by sulfate aerosols but does not include other effects of the aerosols (middle panel), and the third simulates the addition of sulfate aerosols and therefore includes both the heating and chemical effects of the aerosols (bottom panel; Visioni et al., 2021b). These experiments are compared to control simulations without perturbation. Simulations of solar dimming show a limited effect on annually averaged ozone concentrations, with some increase in ozone due to the cooling produced by the reduced solar constant. In the simulations representing aerosol effects, shifts in the aerosol distribution to one hemisphere (e.g., in the Northern Hemisphere, in the example in **Figure 6-10**) result in an uneven interhemispheric change in ozone. Heating-induced transport changes are most important in the tropics and the lowermost stratosphere outside the polar vortex. An increase in ozone in the lower tropical stratosphere is the result of reduced upwelling below the injections and is due to cooler temperatures in the troposphere. A decrease in ozone in the middle stratosphere is a result of stronger upwelling above the injection locations. Furthermore, increases in ozone at mid- to high latitudes are the result of stronger horizontal exchange toward the poles. In summary, the changes in ozone concentration depend strongly on the region (latitude) and season and result from both chemical and dynamical influences of increased stratospheric aerosols with SAI.

6.3.4 Response of Ozone to Different SAI Injection Strategies

Ozone concentration changes discussed in *Section 6.3.3* are shown for one specific injection strategy. However, details of the magnitude of the changes in chemistry and transport depend also on the specifics of the injection strategy and therefore the details of the simulated aerosol distribution (*Section 6.2.3*). A summary of the relationship between specifics of the injection strategy and responses to ozone concentrations based on single model studies is presented in **Table 6-2**.

Simulated ozone responses to SAI can vary with both injection strategy and model (Weisenstein et al., 2022). Responses to SAI are isolated by using fixed sea surface temperatures (averaged over 1988–2007) and fixed greenhouse gases and chlorofluorocarbons (from 2040) in all model experiments shown in **Figure 6-11**. Here, the same injection strategies are applied in two models, including simulations that injected sulfur at two grid points (30°N and 30°S) and at 20 km altitude, simulations that injected in a region (multiple grid points) between 30°N and 30°S and between 19 and 21 km altitude, and simulations that injected sulfur in the form of SO_2 or as accumulation-mode H_2SO_4 aerosols. All the simulations indicate a consistent response of TCO to SAI, with less TCO reduction in the tropics and more TCO reduction in mid- to high latitudes for two-point injections versus regional injections. A stronger TCO reduction occurs if using H_2SO_4 versus SO_2 injections due to a larger resulting sulfate aerosol burden. However, some differences between the SAI response on TCO occur, with the largest disagreement at high latitudes.

6.4 SCENARIO DEPENDENCIES OF SAI ON TOTAL COLUMN OZONE AND OTHER SIDE EFFECTS AND RISKS

The impact of stratospheric aerosol injection (SAI) on total column ozone (TCO) in an SAI scenario is the result of changes in both heterogeneous chemistry (through changes in surface area density [SAD]) and dynamics (including transport, temperature, and water vapor changes; *Section 6.3*). A strong dependency of reductions in TCO and SAD exists during the Antarctic ozone hole season, which is strongly chemically controlled (Tilmes et al., 2020). However, changes in SAD are nonlinearly dependent

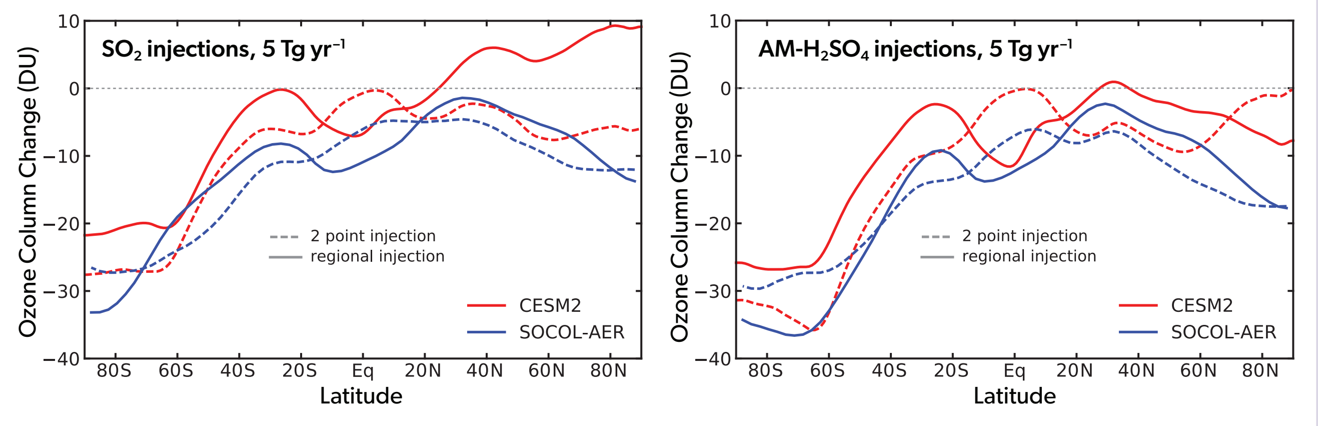

Figure 6-11. Simulated changes in stratospheric total column ozone from simulations in two models (CESM2(WACCM) and SOCOL-AER) with different aerosol microphysics and horizontal and vertical resolutions. Results are shown for different injection materials (gaseous SO_2 *[left]* and accumulation mode AM-H_2SO_4 *[right]*) and injection locations (two-point, 30°N and 30°S, 20 km altitude; regional, from 30°N to 30°S, 19–21 km altitude). [From Weisenstein et al., 2022.]

on the sulfur injection amount. The initial commencement of injections produces smaller aerosol diameters and thus relatively larger SAD per unit of mass than those from continued and larger injections (*Section 6.2*). The impact of changes in SAD on TCO also differs with region and season and is dependent on the associated emissions scenarios, because their effects depend on the concentrations of halogens, nitrous oxide, methane, and other constituents (*Chapter 7*). For example, declining stratospheric halogens in a model simulation with fixed annual amounts of sulfur injected between 2020 and 2070 lead to a decline in global TCO depletion during the 50 years of the experiment (Pitari et al., 2014; Xia et al., 2017).

While global and annually averaged changes in TCO per SAI injection amount for simulated future scenarios have been reported (e.g., Pitari et al., 2014; Weisenstein et al., 2015; Xia et al., 2017), simple measures do not reflect large seasonal and latitudinal ozone changes that can cancel each other out if averaged annually and globally. It is therefore more meaningful to report TCO changes with SAI as a function of season and for different regions, as done here.

Finally, conclusions on whether side effects may outweigh benefits under future SAI scenarios cannot be drawn by isolating any one aspect of the impacts of SAI (e.g., on stratospheric ozone). A more holistic assessment of the major benefits, impacts, and risks of different SAI implementation scenarios and strategies beyond their impact on stratospheric ozone is therefore required and assessed in *Section 6.4.2*.

6.4.1 SAI Response of Total Column Ozone in Different 21st-Century Scenarios

We assess the impacts of SAI on TCO using three SAI scenarios (peakshaving, strong SAI, and medium SAI; *Section 6.1.3.1*) based on recent modeling studies that include interactive aerosols and chemistry in the stratosphere. Simulations following the peakshaving and strong SAI scenarios (Tilmes et al., 2020) are

Table 6-3. Change in total column ozone between future scenarios with SAI and without SAI between the periods 2030–2039 and 2080–2099 for different sets of model experiments (see text for more information). Ranges given are the standard deviation of the ensemble/multi-model mean annual value for the selected 10 years and for different regions and seasons: tropics (20°N–20°S), January averages for NH mid-latitudes (40–60°N), and polar latitudes over the NH (60–90°N) in March and over the SH (60–90°S) in October. "EQ" represents equatorial injections and "Four Point" refers to four-point injections. Bold numbers indicate significant changes in TCO.

	Peakshaving (Four-Point) Minus Baseline (DU)	**Strong SAI (Four-Point) Minus Baseline (DU)**	**Medium SAI (EQ) Minus Baseline (DU)**	**Peakshaving (Four-Point) Minus Baseline (DU)**	**Strong SAI (Four-Point) Minus Baseline (DU)**	**Medium SAI (EQ) Minus Baseline (DU)**
	2030–2039 0.5 °C cooling	2030–2039 0.5 °C cooling	2030–2039 0.2 °C cooling	2080–2099 1.5 °C cooling	2080–2099 ~4 °C cooling	2080–2099 1.8 °C cooling
SH Pole (October)						
WACCM (RCP)		**–64 ± 10**			**–61 ± 10**	
WACCM6 (SSP)	**–52 ± 13**	**–52 ± 13**	**–17 ± 9**	–7 ± 13	**–48 ± 10**	**–31 ± 4**
CNRM-ESM2-1			–1 ± 8			**–17 ± 10**
UKESM1-0-LL			1 ± 4			**–8 ± 4**
NH Pole (March)						
WACCM (RCP)		**–22 ± 21**			4 ± 20	
WACCM6 (SSP)	**–13 ± 10**	**–13 ± 10**	2 ± 9	3 ± 20	–8 ± 21	6 ± 7
CNRM-ESM2-1			(–22 ± 14)*			7 ± 21
UKESM1-0-LL			–5 ± 18			7 ± 9
Mid-latitudes (NH January)						
WACCM (RCP)		**–7 ± 4**			**14 ± 8**	
WACCM6 (SSP)	1 ± 7	1 ± 7	4 ± 2	0 ± 7	6 ± 11	**16 ± 6**
CNRM-ESM2-1			0 ± 1			**18 ± 3**
UKESM1-0-LLI			–1 ± 2			**14 ± 4**
Tropics						
WACCM (RCP)		–1 ± 2			**9 ± 2**	
WACCM6 (SSP)	–1 ± 2	–1 ± 2	1 ± 1	**4 ± 1**	**8 ± 2**	**4 ± 1**
CNRM-ESM2-1			0 ± 1			**2 ± 1**
UKESM1-0-LL			–1 ± 2			**–3 ± 1**

*This value is not shown in **Figure 6-12** because changes in TCO in this simulation are not due to injections of sulfur, which started around 2040 in this model (for more details, see Tilmes et al., 2022).

performed with CESM2(WACCM6) using four-point injections at ~5 km above the tropopause with SSP5-8.5 and SSP5-3.4OS as the baseline scenarios. The strong SAI scenario has also been performed with CESM1(WACCM) as part of GLENS using the RCP8.5 baseline scenario. In both cases, injection rates per location were determined using a feedback control algorithm (**Box 6-2**). For the medium SAI scenario, we assess multi-model results based on three Earth system models (ESMs). The different ESMs used a similar injection strategy in a region around the equator, with one model (CESM2(WACCM6)) injecting at 5 km above the tropopause and the other two models (CNRM-ESM2-1, UKESM1-0-LL) at 1 km above the tropopause (Visioni et al., 2021a; Tilmes et al., 2022) but only two (CESM2(WACCM6) and UKESM1-0-LL) included interactive stratosphere aerosols, and one (CNRM-ESM2-1) used prescribed aerosol radiative properties. While there are additional differences in the specifics of the models, including chemistry and physics, some robust conclusions on the effects of SAI on TCO can be drawn, as summarized in **Table 6-3** and **Figure 6-12**.

For comparisons of the different experiments (and models), four selected cases (regions and seasons) of interest are defined: the tropics (20°N–20°S), January averages for Northern Hemisphere (NH) mid-latitudes (40–60°N), and polar latitudes over the NH (60–90°N) in March and over the Southern Hemisphere (SH) (60–90°S) in October. **Table 6-3** and **Figure 6-12** show differences in TCO for these cases in comparison to their respective baseline scenarios during the same period. Since changes are not linear with time, we illustrate different time periods: one in the near future (2030–2039 average) and one toward the end of the 21st century (2080–2099 average). To contrast differences in TCO evolution for the peakshaving and the strong SAI scenarios, we illustrate the TCO evolution (**Figure 6-13**) and differences with and without SAI (**Figure 6-14**) for the same model version CESM2(WACCM6) and the same injection strategy. Differences between three models for the medium SAI scenario are illustrated in **Figure 6-15**.

6.4.1.1 Changes in SH Spring Polar TCO

In the polar regions, particularly during austral winter and spring, chemical ozone depletion is the dominant process, while transport is important for ozone impacts in other seasons. In addition, changes in the strength of the polar vortex and resulting cooler temperatures can play an important role in the effects of SAI on column ozone (*Section 6.3*). The magnitude of ozone

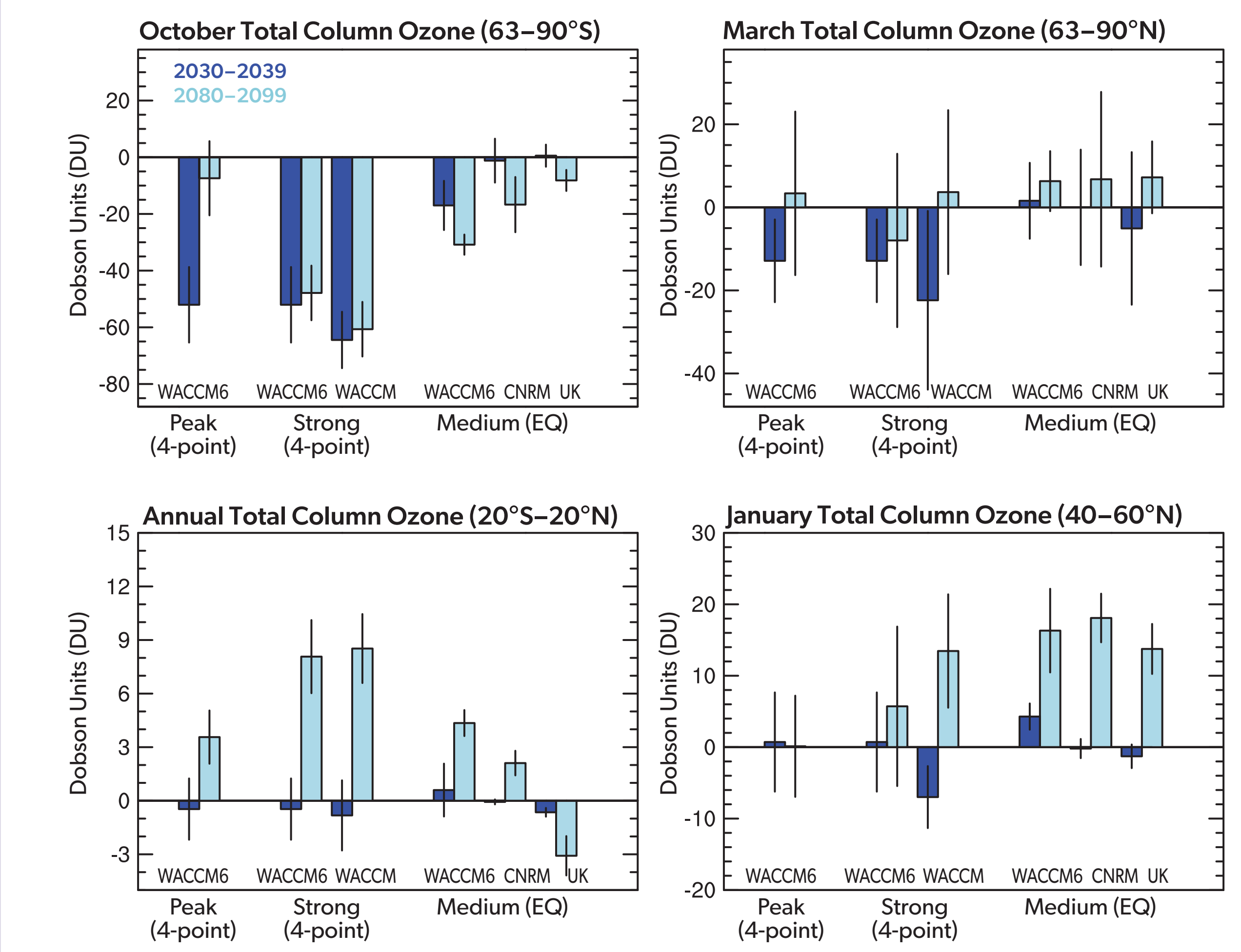

Figure 6-12. Bar chart of the TCO changes given in **Table 6-3**.

depletion is therefore strongly driven by the abundance of halogens in the stratosphere and changes in SAD. This can be seen in two features of past ozone trends: After 1980, Antarctic TCO exhibited a strong decline of over 80 DU (consistent with **Figure 4-4**), driven by increasing halogen concentrations. After the Mount Pinatubo eruption in 1991, and the associated increase in aerosol SAD, ozone decreased by a further 40–60 DU within the next five years (**Figure 6-13**, left top).

The reduction of the stratospheric halogen burden and changes in SAD also play a role in the projected future impacts under the peakshaving, medium and strong SAI scenarios. The gradual phasing in of sulfur injections in all three scenarios increases SAD quickly during the first 10 years, then moderately thereafter. This leads to a rather abrupt initial deepening of the Antarctic ozone hole, which is stronger under the peakshaving and strong SAI scenarios (following the same scenario until 2040) than under

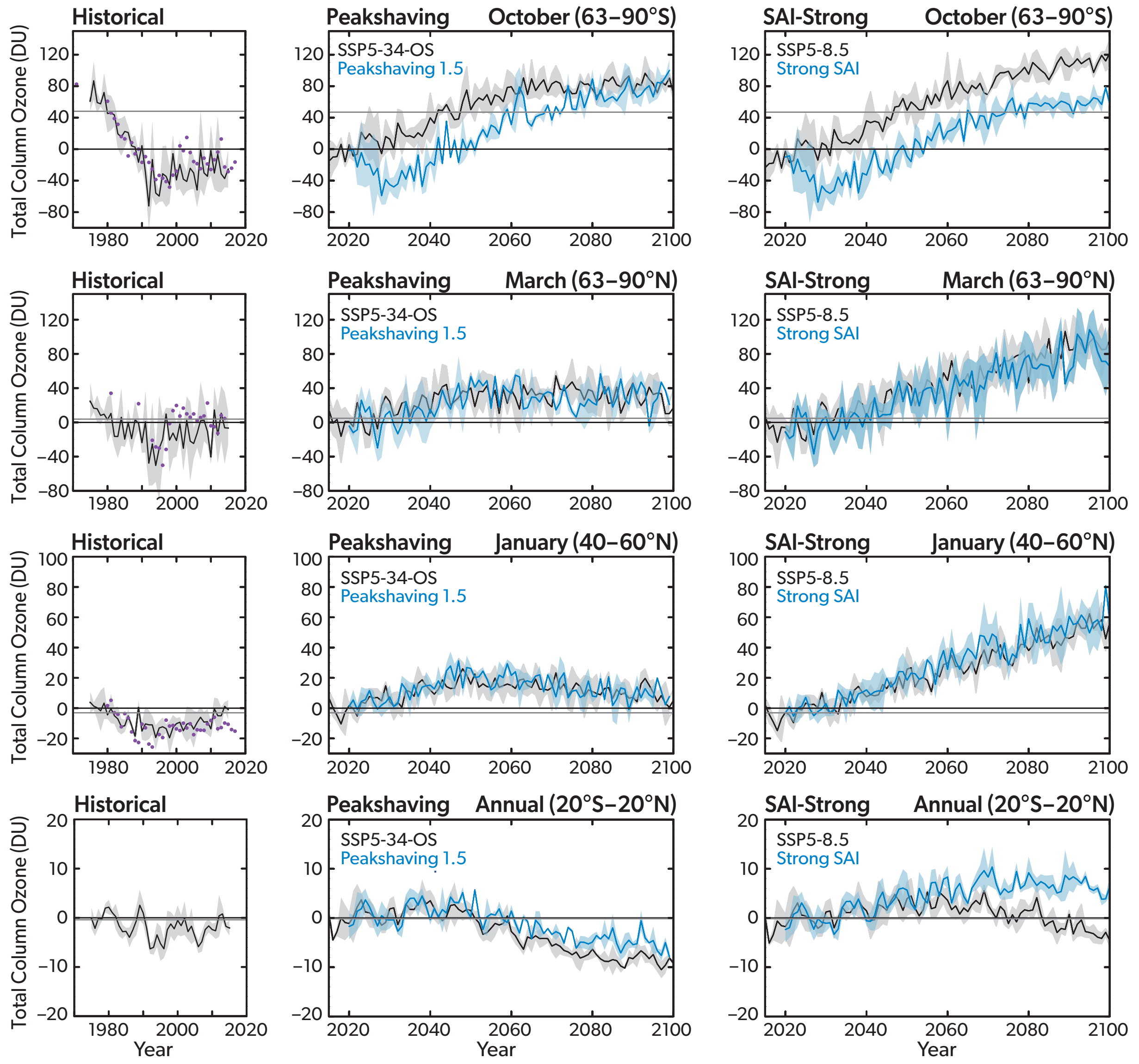

Figure 6-13. Simulated impacts on TCO in different latitude bands and seasons (*rows*), relative to the 2015–2025 TCO average, for the past (historical; *left column*) and projected for the peakshaving (*middle column*) and strong (*right column*) SAI scenarios. The ensemble means are shown for the baseline scenario (black) with standard deviation (gray shading) and for the SAI experiments (blue) with the standard deviation (light blue shading) based on simulations with CESM2(WACCM6) using SSP5-3.4-OS and SSP5-8.5 for the baseline scenarios, against which the peakshaving and strong SAI scenarios are compared, respectively. Black horizontal lines indicate the 2020 values and gray lines the 1980 values, based on the model simulations. In the historical TCO panels, a three-year running mean has been applied to the TCO observations from the Solar Backscatter Ultraviolet (SBUV) Merged Ozone Data Set (Frith et al., 2017; purple symbols) to facilitate comparison with the ensemble mean of the control simulation.

the medium SAI scenario (**Figures 6-14** and **6-15**). In the SH austral spring, for the peakshaving and strong SAI scenarios the initial ramp-up of the injections to cool 0.5 °C in 20 years leads to ozone depletion in 2030–2039 of 52 ± 13 DU in the CESM2(WACCM6) simulations and 64 ± 10 DU in the CESM1(WACCM) simulations. This results in an average depletion of 58 ± 20 DU, when accounting for additional uncertainties driven by the injection strategy (see below). Here, SAI is simulated to start in 2020, and the resulting TCO depletion in this early period is nearly as strong as was observed during the historic period with the deepest ozone holes. Injections in later years are likely to have a smaller effect because of the expected decline in the stratospheric halogen burden with time (see *Chapter 7* and **Figure 7-7**).

Reductions in TCO in SH austral spring are less strong for the medium SAI scenario because of a smaller required cooling in this experiment of about 0.2 °C for the first 20 years and smaller required SAI injections compared to the peakshaving and strong scenarios (**Figure 6-15**). The decline in TCO over SH Antarctic spring between 2030 and 2039 is only present in the CESM2(WACCM6) simulations (17 ± 9 DU ozone loss). The other two models did not require significant sulfur injection during the period 2030–2039 in this scenario and therefore did not show any ozone loss (see Tilmes et al., 2022, for more details).

Toward the end of the 21st century (2080–2099), the SH Antarctic spring TCO changes differ significantly between the three scenarios. For the peakshaving scenario, simulated SH polar TCO is reduced by only 7 ± 13 DU compared to the baseline. For this scenario, the recovery of the ozone hole is therefore expected to happen before the end of the 21st century. The strong SAI scenario assumes continuously increasing annual sulfur injection rates toward the end of the 21st century and decreasing stratospheric halogen content; the net result is that reductions in SH polar TCO are essentially the same in 2080–2099 for the two model versions (61 ± 10 DU and 48 ± 10) as they are in 2030–2039 (64 ± 10 DU and 52 ± 13 DU; **Table 6.3** and **Figure 6-12**). This results in a delay of the ozone recovery, which can vary from 25 to over 55 years depending on the injection strategy (latitude and altitude of injections, as discussed in Tilmes et al., 2021). For the medium SAI scenario, the stronger increase in injected mass toward the end of the century leads to increasing SH Antarctic spring ozone loss of up to 31 ± 4 DU in 2080–2099 in the CESM2(WACCM6) simulations and between 8 and 17 DU for simulations with the other models.

The results presented in this section are specific to the injection strategy used. Larger ozone loss up to 20 DU has been simulated for equatorial injections (Tilmes et al., 2021). This is because equatorial injections result in a more pronounced strengthening of the polar vortex and cooler vortex temperatures, as well as strongly enhanced stratospheric water vapor compared to four-point injections outside the equator. Furthermore, the smallest reductions in TCO during Antarctic spring (up to 20 DU) are expected for low-altitude injections, at around 20 km (Tilmes et al., 2021). Injections of sulfur at lower altitudes result in a shallower aerosol distribution than high-altitude injections, and aerosol that is more concentrated towards the tropopause. This results in changes in the importance of different ozone loss cycles, while the resulting increase in stratospheric water vapor increases HO_x-driven ozone loss cycles. Furthermore, the more-confined

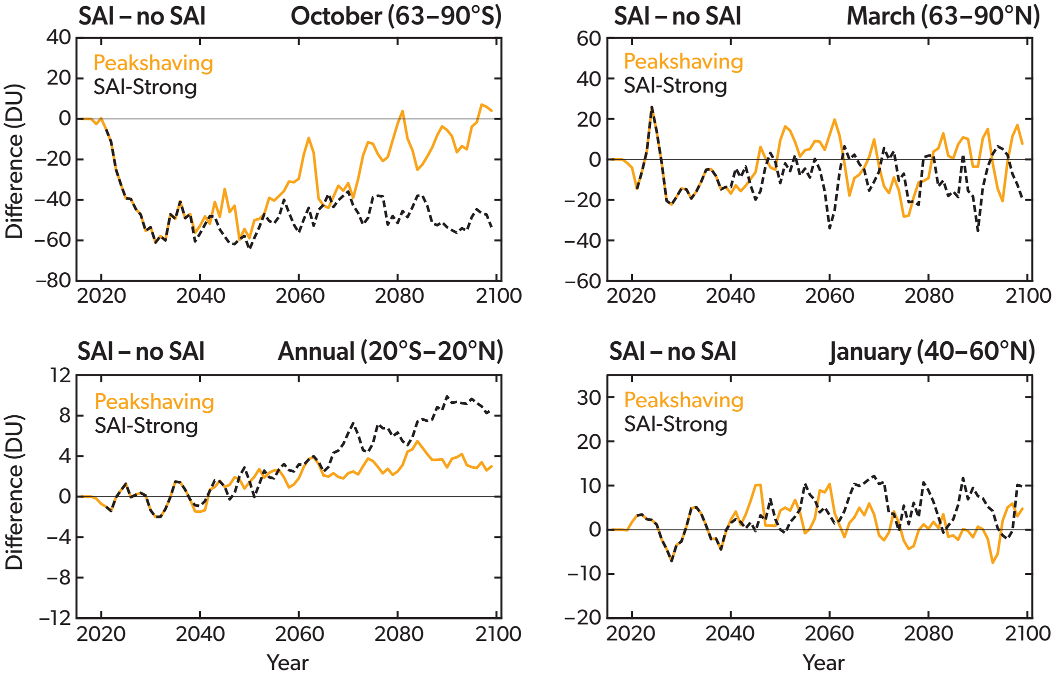

Figure 6-14. Ensemble mean differences in TCO between simulations that include SAI (in the peakshaving [orange] and strong [black] SAI scenarios) and TCO in the baseline simulation (no SAI), for different regions and seasons (different panels), as shown in **Figure 6-13**. A running mean of three years has been applied to the differences.

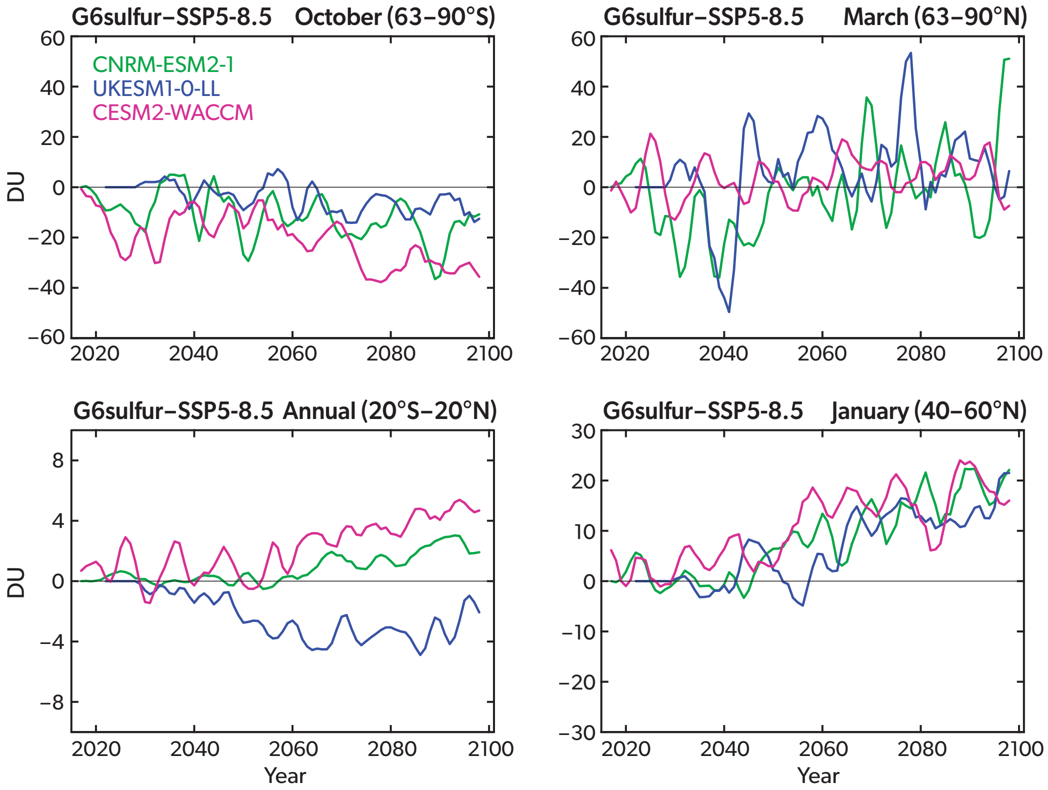

Figure 6-15. Differences between the ensemble mean of simulated total column ozone between 2020 and 2100 in the medium SAI scenario and in the baseline simulation (SSP5-8.5 with no SAI), for runs using the three different models (colored lines) and for four different seasons and regions (different panels). [From Tilmes et al., 2022.]

heating at the tropical tropopause in the low-altitude injection simulation induces a stronger transport of ozone toward mid- and high latitudes, which counters the larger reduction of net chemical ozone production rates.

6.4.1.2 Changes in NH Spring Polar Total Column Ozone

The strength and temperature of the Arctic polar vortex varies strongly from year to year. For the NH polar region in March, cooler winters can result in a stronger reduction in TCO in the polar vortex with increased SAD, relative to that in warmer winters (Tilmes et al., 2008). Changes in TCO in the NH polar region are therefore more strongly driven by transport changes than are changes in TCO at SH high latitudes. NH polar spring TCO reductions reached 50 DU between 1990 and 2000 based on observations using a three-year running mean. This is comparable to the ensemble mean of the model simulations (**Figure 6-13**). The large variability of Arctic ozone loss depending on the meteorological situation is not reflected in the monthly-mean zonal-average analyses. Much smaller reductions in NH polar spring TCO are projected for 2030–2039 in the three SAI scenarios considered here, with reductions of 13 ± 10 DU and 22 ± 21 DU in the peakshaving and strong SAI scenarios (where ranges reflect differences across model versions), for both the peakshaving and strong SAI scenarios (**Table 6-3** and **Figure 6-12**). TCO changes in the medium SAI scenario relative to the baseline scenario vary in the sign and so are not significant (Tilmes et al., 2022). Toward the end of the century, changes in TCO are not statistically significant for any of the three SAI scenarios. As for the historical period, ensemble means of monthly and zonally averaged TCO values over 63–90°N, as are shown here, do not reflect chemical changes during very cold or warm Arctic winters and therefore may lead to an underestimation of regional TCO changes. A more detailed investigation of TCO within the polar vortex over the Arctic on an annual basis has not been performed at this point.

6.4.1.3 Changes in Total Column Ozone at NH Winter Mid-latitudes

NH mid-latitude winter TCO declined by around 10–20 DU between 1980 and the 1990–2000 period in both the observations and in the model simulations (**Figure 6-13**). After the year 2000, the model simulates an increase in TCO, reaching amounts close to 1980 values around 2020. Later in the 21st century, with a strong future warming scenario the model simulates a super-recovery of ozone at mid- to high latitudes during NH winter due to stratospheric cooling and GHG-induced increases in downwelling of the Brewer-Dobson circulation (BDC; Butler et al., 2016). With SAI, simulations indicate that the lower-stratospheric heating and the resulting acceleration of the BDC can result in an additional increase in stratospheric ozone and other stratospheric trace species, such as nitrous oxide (N_2O), chlorofluorocarbons (CFCs), and methane (CH_4), particularly in the winter and spring of the corresponding hemisphere (Visioni et al., 2017b; Tilmes et al., 2017). These changes produce a mixed chemical response, with a reduction in the net chemical production of ozone in the lowermost stratosphere and the upper stratosphere and an increase in the mid-stratosphere due to the reduced reactive nitrogen cycle. Depending on the injection location, the largest change in mid-latitude ozone with SAI was simulated to occur between 40°N and 60°N in January (Tilmes et al., 2018b).

Changes in the first 20 years of the SAI applications in NH winter mid-latitudes in January are, for the most part, not significant. Toward the end of the 21st century, 2080–2099, the strong SAI scenario simulated using CESM2(WACCM6) and the medium SAI scenario simulated using all three models produce a significant increase in TCO, of between 14 and 18 DU (Tilmes et al., 2022). Considering different strategies for the strong SAI scenario, the largest and earliest simulated increase in TCO compared to baseline conditions was found for the equatorial injections (Tilmes et al., 2021).

6.4.1.4 Changes in Total Column Ozone in the Tropics

In the tropics, TCO declined from 1980 values between 1990 and 2000, with a maximum reduction of around 5 DU, and increased again thereafter to reach 1980 values around 2020. Future scenarios without SAI show either a decline or an increase in tropical TCO depending on the scenario (Keeble et al., 2021). Changes in TCO in the tropics with SAI result from a combination of increases and decreases in ozone concentration at different altitudes, depending on the chemical and dynamical changes (*Section 6.3*). In the earlier years of simulated SAI implementation (2030–2039), none of the three selected SAI scenarios indicate significant changes in tropical TCO. However, toward the end of the 21st century, significant increases in TCO are simulated for the peakshaving (4 ± 1 DU) and strong (9 ± 2 DU) SAI scenarios. The three different models used for the medium SAI scenario show a mixed signal, leading to no changes in the multi-model mean tropical TCO. Increases in ozone in the tropical mid-stratosphere are more pronounced with increasing injection amounts, while chemical reductions due to the HO_x and ClO_x cycles are more pronounced during the beginning of the injections. The largest increase in TCO is projected for a high-altitude injection case, consistent with an aerosol distribution that reaches higher in altitude and therefore has a larger chemical production of ozone through the nitrogen cycle (Tilmes et al., 2021).

6.4.2 Other Impacts and Risks Based on Different SAI Scenarios

The intended benefits expected from SAI are the reduction or stabilization of global and regional surface temperatures and, consequently, a reduction in climate change impacts. Model simulations uniformly demonstrate that solar dimming reduces global mean temperatures and therefore can counter surface warming under a range of different future scenarios (**Figure 6-16**; e.g., Govindasamy and Caldeira, 2000; Kravitz et al., 2013, 2021). Depending on the strategies used to reach specific surface temperature targets (**Box 6-2**), the benefits of SAI-induced cooling include reducing changes in extreme heat and rainfall events (Curry et al., 2014; Muthyala et al., 2018a, 2018b; Bhowmick et al., 2021). The reduction in extreme precipitation with SAI (Ji et al., 2018) has been shown to result in reductions in flood risks in most of the regions of the globe (Wei et al., 2018). Other benefits include the recovery of sea ice (Jones et al., 2018; Kravitz, 2020), and land ice area (by maintaining the ice sheet surface mass balance; Tilmes et al., 2020); an increase in ocean net primary productivity (Tilmes et al., 2020); and a decrease in the frequency of extreme storms in the North Atlantic and heatwaves in Europe (Jones et al., 2018).

In addition to these benefits, there are various unintended side effects (e.g., Robock et al., 2008a; Robock et al., 2020) beyond changes in ozone (*Sections 6.3* and *6.4.1*). Some of these side effects increase with SAI amount, including an overcompensating reduction in global precipitation compared to the baseline scenarios with increasing greenhouse gas warming. We note that global precipitation is only one measure for changes in the hydrological cycle, and other measures including evaporation and soil moisture should also be considered for detailed climate impact assessments. **Figure 6-16** shows the effects of applying SAI to different future scenarios with the objective of maintaining temperatures at or below 1.5 °C above preindustrial conditions, based on GHG scenarios ranging from strong mitigation to moderate mitigation, delayed mitigation, and no mitigation (Jones et al., 2018; Tilmes et al., 2020). The strongest reductions in global mean precipitation were simulated for the no-mitigation scenario coupled with strong SAI, while no significant precipitation changes occurred in the simulations where there is strong mitigation of GHG emissions and only a small amount of SAI is needed to keep temperatures from rising above the 1.5 °C limit (**Figure 6-16**). There are also various other plausible future SAI scenarios that have been discussed in the literature but are not discussed here. Other risks, including the termination effect (see below), also strongly increase with injection amount and therefore the cooling amount imposed with SAI. Other side effects, such as ocean acidification and impacts on land primary productivity, strongly depend on the GHG emissions scenario, while the selected SAI scenario affects these measures only to a small degree.

In the following, we give a brief overview of other side effects and risks beyond the effects on ozone. The list below is not intended to be comprehensive or exhaustive, as there are other risks and consequences besides those detailed here that are beyond the scope of this assessment.

The following are side effects of significant (climate changing) solar radiation modification (SRM) that are independent of the SRM strategy or approach that would be used (e.g., stratospheric aerosol injection, marine cloud brightening, or cirrus cloud thinning). These risks scale with the amount of SRM applied and hence depend on the specifics of the SRM scenario.

- **Termination risk:** If any significant SRM application was suddenly terminated, the Earth's climate would rebound to the baseline climate within a matter of years, and this could result in unprecedented rates of climate change (e.g., Jones et al., 2013). This could have severe consequences, such as warming rates beyond the adaptive capacity of vulnerable ecosystems (Trisos et al., 2018). However, a slower ramp-down or a continuation of SRM shortly after a sudden termination could potentially prevent these effects (Parker and Irvine, 2018).
- **Risks of uneven inter-hemispheric SRM applications:** SRM, if applied largely unevenly to the two hemispheres or applied in only one hemisphere, would introduce an inter-hemispheric cooling gradient across the equator. The resulting

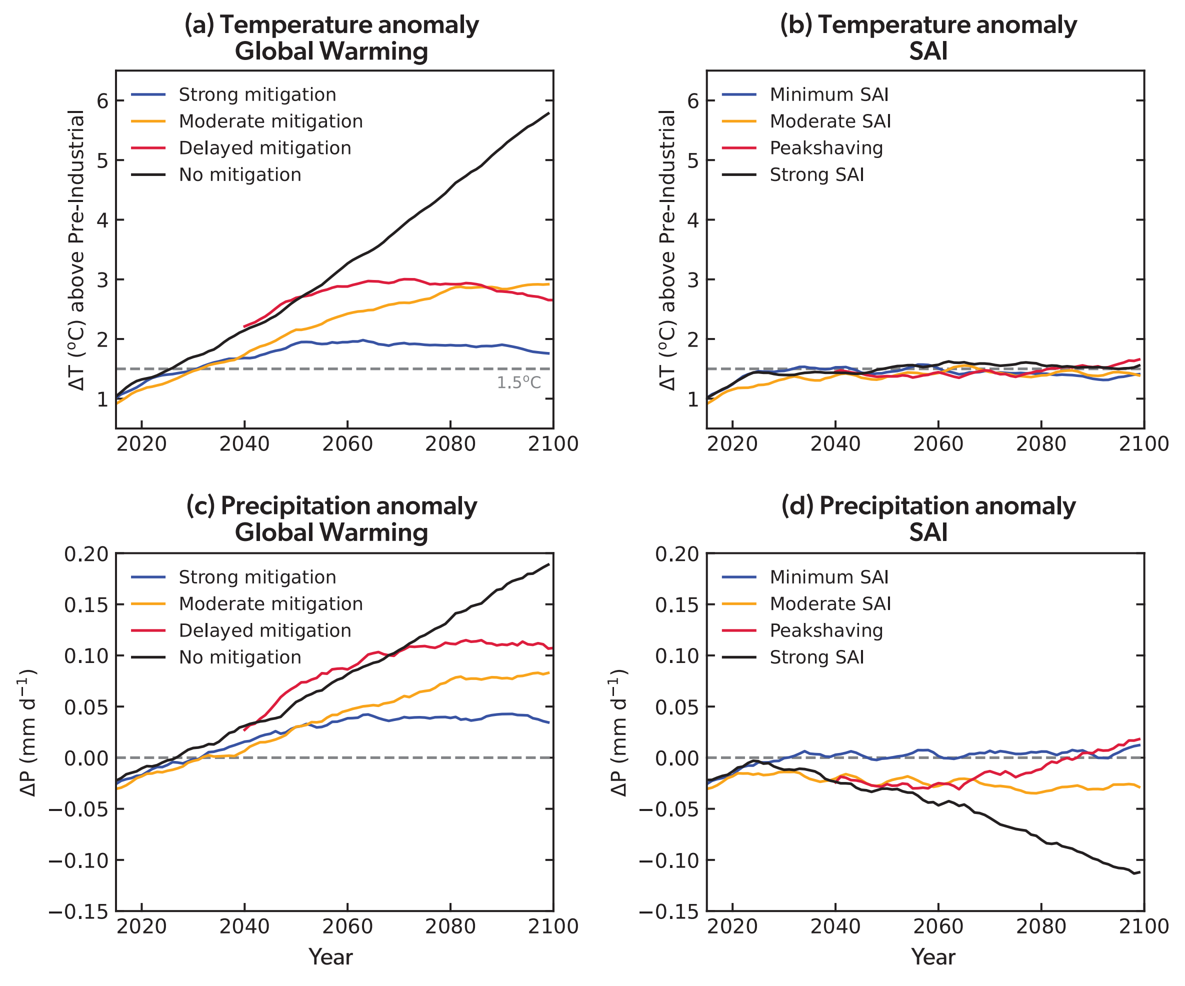

Figure 6-16. Global mean surface temperature anomaly in (a) global warming simulations and (b) corresponding simulations in which SAI is applied to maintain temperature at 1.5 °C above preindustrial levels, and (c, d) the equivalent global mean precipitation time series. "No mitigation / strong SAI" refers to the average of the RCP8.5 / GEO-8.5 simulations of Jones et al. (2018) and the SSP5-8.5 / SSP5-8.5 1.5 simulations of Tilmes et al. (2020). "Delayed mitigation / peakshaving" refers to the SSP-3.4-OS / SSP-3.4-OS 1.5 simulations of Tilmes et al. (2020). "Moderate mitigation / moderate SAI" and "strong mitigation / minimum SAI" refer to the RCP4.5 / GEO-4.5 and RCP2.6 / GEO-2.6 simulations of Jones et al. (2018), respectively. The baseline periods are RCP8.5 2020–2030 for Jones et al. (2018) and SSP5-8.5 2015–2025 for Tilmes et al. (2020), or approximately the decade in which the Paris threshold of preindustrial temperature +1.5 °C is exceeded in the respective climate model. All time series are smoothed by five-year running means.

cross-equatorial energy and moisture transport (Hwang and Frierson, 2013; Stephens et al., 2016; Hawcroft et al., 2017) would shift the intertropical convergence zone (ITCZ) toward the (relatively) warmer hemisphere and therefore change the rainfall pattern (e.g., Caldeira and Wood, 2008; Robock et al., 2008b; Haywood et al., 2013; Jones et al., 2017). Such impacts have been observed after high-latitude explosive volcanic eruptions that preferentially load the stratosphere in one hemisphere (e.g., Oman et al., 2006; Jones et al., 2017).

- **Ocean acidification:** Ocean acidification, which is induced by high CO_2 concentrations, cannot be mitigated significantly by SRM (Matthews and Turner, 2009). Coral bleaching, which is more strongly dependent on ocean temperatures than on ocean acidity, does appear to be somewhat mitigated by SRM (Kwiatkowski et al., 2015).

- **Sea level rise:** Stabilizing global mean temperature through SRM would substantially reduce sea level rise in the future (Irvine et al., 2017). However, keeping sea surface temperatures from rising does not completely offset the deep ocean heat uptake, which causes the net downwelling radiative flux at the top of the atmosphere to remain positive (Jones et al., 2018; Fasullo et al., 2018); thus, stabilizing global sea level rise would require overcooling the Earth system (Irvine et al., 2018).

The following are side effects and risks that are specific to global solar dimming or SAI, although some similar changes may also apply to other SRM methods:

- **Impacts on the hydrological cycle:** Solar dimming weakens the hydrological cycle (Tilmes et al., 2013; Niemeier et al., 2013; Fyfe et al., 2013; Ferraro et al., 2014), consistent with observations after volcanic eruptions (Trenberth and Dai, 2007). Using SAI may amplify this effect, especially if strongly absorbing aerosols are used (Ferraro et al., 2014; Visioni et al., 2021b; Haywood et al., 2022). Following a strong SAI scenario, an increase in global precipitation in the baseline scenario would be increasingly overcompensated by the growing amount of aerosol injection needed to compensate for GHG warming, as demonstrated in two independent model studies (**Figure 6-16**; Jones et al., 2018; Tilmes et al., 2020). This can result in reductions in rainfall and a weakening of monsoonal precipitation in some regions (Simpson et al., 2019). On the other hand, the precipitation increases in a low-forcing GHG scenario without SAI would be reversed to close to present-day conditions if a peakshaving SAI scenario were applied.

- **Tropospheric circulation and regional climate:** SAI using sulfate aerosols weakens storm tracks due to induced changes in the latitudinal temperature and humidity gradients, forcing a poleward shift of the storm tracks. This effect predominantly impacts the Northern Hemisphere (Gertler et al., 2020). Stratospheric heating using sulfate SAI can induce a positive anomaly of the North Atlantic Oscillation (NAO) during the Northern Hemisphere winter season and a winter warming over Eurasia, with associated increased rainfall in northern Europe and decreased rainfall in southern Europe (Banerjee et al., 2021; Jones et al., 2022). In addition, surface winds imposed by changes in stratospheric dynamics can change the upwelling of warm waters around Antarctica, thereby impacting the surface climate (McCusker et al., 2015).
- **Impacts on acid rain:** Aerosols (and precursors) injected into the stratosphere inevitably deposit back to the surface. Depending on the material injected (e.g., SO_2) this could contribute to acidification of precipitation. Even for the strong SAI scenario using sulfate, SAI would not significantly increase the amount of sulfate deposited over polluted regions on a decadal scale compared to current anthropogenic emissions of SO_2. However, more pristine areas at high latitudes may see significant increases in sulfate deposition (Kravitz et al., 2009; Visioni et al., 2020c). The effects of other aerosols (*Section 6.5*) that could potentially be used for SAI have not been investigated.
- **Impacts on tropospheric ozone:** Solar dimming applied to offset the effects of increasing GHG concentrations can lead to an increase in surface ozone due to the increase in stratospheric ozone from both the increasing GHGs, reductions in sunlight, and reductions in stratospheric water vapor (Nowack et al., 2016). On the other hand, SAI can lead to a reduction in global tropospheric and surface ozone, due to the decrease in stratosphere-troposphere exchange of ozone (if stratospheric ozone depletion has increased) and reduced tropospheric ozone production based on the ozone-destroying hydrogen cycle. The decrease in surface ozone may lead to a reduction in associated mortality (Nowack et al., 2016; Xia et al., 2017; Eastham et al., 2018).
- **Impacts on vegetation and crops:** Solar dimming experiments have shown that reduced surface heat stress from SRM-induced cooling can combine with the fertilization effect of increased CO_2 concentrations to lead to a reduction in some negative impacts of climate change on crops and vegetation (Xia et al., 2014; Glienke et al., 2015; Fan et al., 2021). In addition to the beneficial impact on crops from enhanced photosynthesis from higher CO_2 concentrations, SAI may enhance the terrestrial photosynthesis rate by increasing the ratio of direct to diffuse radiation at the surface (Xia et al., 2016, 2017; Cao, 2018), although the magnitude of this positive climate response is contested (Proctor et al., 2018).
- **Impact on surface ultraviolet (UV) and visible radiation:** Studies that have investigated the impact of SAI on UV irradiance at the surface have found little change in UV in the tropics and mid-latitudes and an increase in UV in polar regions (e.g., Tilmes et al., 2012, Pitari et al., 2014; Visioni et al., 2017). These impacts are due to the combined impacts of increases in ozone concentrations and the strong scattering of UV radiation back to space from the aerosol at tropical and mid-latitudes and ozone depletion at polar latitudes. The substantial increase of stratospheric aerosol for a strong SAI scenario towards the end of the 21st century has been simulated to result in a significant reduction of UV (around 20–30%) in the subtropics and higher latitudes compared to present day (Madronich et al., 2019). A simultaneous decrease in the biologically active irradiances for DNA damage by 25–33% was modelled, with comparable contributions from the effects of the aerosol scattering of UV radiation and of ozone recovery. On the other hand, the photosynthetically active radiation (PAR), which is mainly affected by the changes in diffuse-direct ratio of radiation, shows an increase of up 35–40% in high northern latitudes.

6.5 ALTERNATIVE SAI MATERIALS

The impact of sulfuric acid aerosol on stratospheric ozone results from its physical and chemical properties, i.e., its bulk complex refractive index, aerosol size distribution, and the chemical composition of the aerosol surface. Alternative materials with different properties could reduce ozone loss resulting from heterogeneous chemistry or from the dynamical response due to heating from absorption of solar and terrestrial radiation. The heating and resulting dynamical response depend on material bulk properties that can be observationally constrained with reasonable confidence. The heterogeneous chemistry responsible for activating halogen species and converting nitrogen oxides (NO_x) to nitric acid (HNO_3) depends on details of the surface composition and associated chemical mechanisms. Laboratory studies of these properties are challenging, and the large uncertainty is due to an imperfect understanding of the evolution of the surfaces of alternative materials over stratospheric lifetimes. Coatings of candidate aerosol particles by sulfuric acid and reactions with sulfuric acid, nitric acid, or hydrogen chloride may significantly impact the aerosol chemical and optical properties (e.g., Tang et al., 2014; Dai et al., 2020).

Alternative materials can potentially reduce impacts on stratospheric ozone, but uncertainty in their net radiative and chemical properties (or impacts) is currently considerable compared to that for sulfate (*Section 6.3*). The properties of sulfates and their impacts are comparatively well studied, and processes are more or less comprehensively included as a key stratospheric aerosol component in climate models, owing to the necessity of quantifying the periodic cooling from explosive volcanic eruptions (*Section 6.2.2.1*). Simulations of the impacts of stratospheric sulfate perturbations have been benchmarked against a relatively large set of observations and measurements (*Section 6.6*), providing more confidence in their representation than in any alternative materials. This section provides an assessment of the limited number of studies that have investigated alternative particles and how they might impact stratospheric heating rates, dynamics, and heterogeneous chemistry.

6.5.1 Motivation

Many materials, especially solid ones, do not have acidic or water-containing surfaces and thus do not have the same ozone-depleting surface heterogeneous chemical reactions as sulfate. The impacts of these particles on ozone will differ owing to different surface properties (e.g., their catalytic activity, hygroscopicity, pH, surface roughness, and the degree to which they become coated with naturally occurring sulfate) and how these vary over stratospheric lifetimes. There is little information on these properties for alternative materials. The bulk optical properties of numerous materials exhibit negligible absorption of solar or terrestrial radiation. Many, such as silicon carbide, alumina, and calcite, have other promising qualities, e.g., non-toxicity or ease of production at low costs. Few materials are truly transparent to terrestrial radiation in the atmospheric window; diamond is a notable exception. Some absorb only in the longwave infrared or in the terrestrial radiation spectral regions that coincide with absorption bands of other atmospheric constituents, which reduces their impact on stratospheric heating. These include alumina, calcite, zirconia, and titania (both rutile and anatase polymorphs), but titania is a well-known photocatalyst with strong ultraviolet absorption in the visible (UV-VIS). There is consensus that using pure materials with well-characterized optical properties and little absorption would reduce the dynamical response caused by the heating in the lowermost tropical stratosphere with sulfate aerosols, and with that the effects on stratospheric ozone would be reduced. However, additional complications of these materials can include toxicity; formation of coatings, as these aerosols mix with stratospheric aerosols from natural sources; and potential impacts on cirrus clouds. Such complexities have not yet been adequately addressed in the scientific literature.

While there are few studies on the impacts of alternative materials on ozone and certainly no complete treatment within climate models, an increasing number of studies are focusing on some aspect of alternative materials within the context of stratospheric climate intervention (Ferraro et al., 2011, 2012; Pope et al., 2012; Weisenstein et al., 2015; Jones et al., 2016a; Keith et al., 2016; Dykema et al., 2016; Moon et al., 2018 Cziczo et al., 2019; Dai et al., 2020; Huynh and McNeill, 2021).

6.5.2 Effects of Different Aerosols on Heating, Radiation, and Dynamic Response

The optical properties of alternative materials determine the radiative forcing they produce, which is central to their efficacy for stratospheric climate intervention, as well as how they would affect stratospheric heating rates and the resulting dynamical responses. Even for alternative particles with no absorption of radiation, minor stratospheric heating at altitudes above the aerosol results from the increased backscatter of solar UV-Vis radiation, which is then absorbed by ozone and other trace gases. This effect is more than an order of magnitude smaller than the direct heating from absorption by sulfuric acid aerosols (Dykema et al., 2016). Stratospheric heating and the associated dynamical responses result from materials with non-zero imaginary refractive indices in the solar UV-Vis (titania) or the atmospheric window in the terrestrial IR (sulfuric acid).

Standalone radiative transfer calculations have been used to investigate a range of materials (e.g., Ferraro et al., 2011, 2012; Dykema et al., 2016). **Figure 6-17** shows the stratospheric temperature change for loadings of some candidate alternative particles that produce a radiative forcing of -1 Wm^{-2}. The imaginary part of the refractive index for sulfate increases significantly at wavelengths larger than 1.2 µm, where the incident radiation is many orders of magnitude less than at the peak of the solar spectrum. However, it still causes significant stratospheric heating. Other materials, in particular diamond, have a much smaller effect on stratospheric temperature (Dykema et al., 2016).

Few studies have used general circulation models (GCMs) to study the impacts of using alternative materials for SAI. Jones et al. (2016a) imposed fixed size distributions for stratospheric aerosols within the HadGEM2-CCS climate model and compared the impacts of black carbon and titania to those of sulfate. Both of these materials have strong absorption bands in the solar UV-VIS range. Black carbon has a very large heating effect in the stratosphere. This absorption results in strong stratospheric heating, which is shown to result in a rapid collapse of the QBO (Jones et al., 2016a, Haywood et al., 2022). Ferraro et al. (2015) performed simulations similar to the G1 GeoMIP simulations, using stratospheric aerosol burdens sufficient to offset quadrupled carbon dioxide. Their simulations showed that the use of titania and sulfate both resulted in a strong intensification of the Northern Hemisphere polar vortex and a northward shift of the storm tracks. The heating of the tropical tropopause with titania was larger than with sulfate, due to the strong UV-VIS absorption of titania compared with sulfate (**Figure 6-18**). Ferraro's study, however, was highly idealized, with a very concentrated tropical aerosol layer. Dykema et al. (2016) demonstrated that diamond, moissanite (SiC), alumina

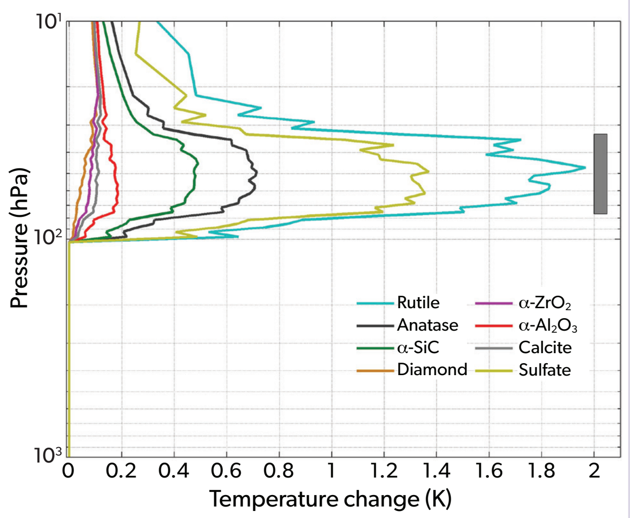

Figure 6-17. Equilibrium stratospheric heating produced by a mass of monodisperse solid aerosols of optimized radii sufficient to achieve -1 Wm^{-2} shortwave radiative forcing. The gray bar on the right shows the approximate location of the aerosol layer. [Adapted from Dykema et al., 2016.]

(Al_2O_3), and calcium carbonate ($CaCO_3$) as calcite should have greatly reduced dynamical impacts due to less radiative heating and thus may be favorable in the trade-off between radiative forcing and dynamical response when compared to sulfate aerosols. However, this assumes that the complex refractive indices of the aerosols remain unchanged over the stratospheric lifetime of the particles, which is not proven, especially for reactive materials such as calcium carbonate. Idealized climate model simulations, where the absorption from sulfate aerosols is increased in the solar spectrum, reveal significantly greater impacts on stratospheric heating with resultant strong impacts on the QBO, a strongly enhanced positive phase of the North Atlantic Oscillation and the associated rainfall patterns, enhanced stratospheric water vapor, and a delay in the recovery of the Antarctic ozone hole (Haywood et al., 2022).

In summary, compared to sulfate, the use of non-absorbing materials should effectively reduce stratospheric heating and associated dynamical responses, which should therefore reduce dynamically induced ozone changes. Large uncertainties result from 1) lack of confidence in the optical properties of materials over stratospheric lifetimes relative to their baseline and/or potentially idealized literature values, 2) limitations in quantitative knowledge of absorption coefficients (Dykema et al. 2016), 3) the small number of studies investigating dynamical responses with alternative materials, and 4) uncertainties in the potential impacts of different materials on other aspects of the climate system such as on cirrus clouds (Cziczo et al., 2019).

6.5.3 Chemical Effects on Ozone Using Alternative Materials

Sensitivity studies using a chemical-transport model indicate that non-absorbing materials such as diamond and alumina may greatly reduce stratospheric ozone loss compared to sulfate (Weisenstein et al., 2015; **Figure 6-18**).

Laboratory studies have found high uptake coefficients for the HCl + $ClONO_2$ reaction, together with reduced hydrolysis of nitrogen pentoxide (N_2O_5) for alumina compared to sulfuric acid (H_2SO_4) (e.g., Molina et al. (1997). Chlorine nitrate ($ClONO_2$) reactivity has been studied on titania at room temperature but without the addition of hydrogen chloride (HCl) or hypochlorous acid (HOCl) (which would both be present in the stratosphere), so the utility of the studies is limited (Tang et al., 2016). Similarly, N_2O_5 and hydroperoxy radical (HO_2) uptake on titania have been studied only at room temperature (Tang et al., 2014; Moon et al., 2018), with the latter study concluding that the uptake of HO_2 radicals on titania likely is too slow to impact ozone chemistry. The implications of the difference in heterogeneous chemistry of alumina compared to sulfuric acid remain uncertain.

Hypothetically, calcium carbonate stratospheric aerosol could increase ozone concentrations based on the potential rapid uptake of HCl and HNO_3 by calcium carbonate particles, changing the sign of the trade-off between radiative forcing and ozone present for sulfate (Keith et al., 2016). However, HNO_3 and HCl chemistry on calcium carbonate at room temperature suggest only moderate uptake rates. In addition, initial uptake rates of HCl and HNO_3 on calcium carbonate are low and decrease further via passivation under stratospheric conditions; i.e., there is rapid formation of a non-reactive surface layer that greatly slows down further reaction (Dai et al., 2020). Observed uptake coefficients orders of magnitude higher than those determined by Dai et al. (2020) were found at stratospheric temperatures (Huynh and McNeill, 2021), but the degree of passivation after HCl exposure, which determines the actual stratospheric reactivity, could not be determined.

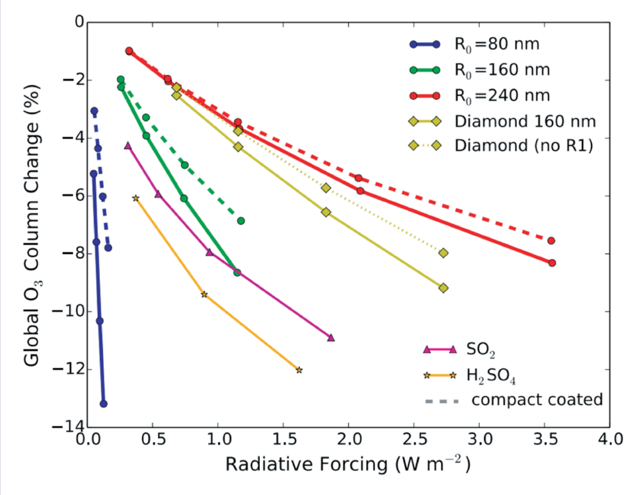

Figure 6-18. The trade-off between ozone depletion and radiative forcing for some alternative geoengineering materials and for sulfuric acid, based on simulations using the AER-2D chemical-transport model. Sulfuric acid is injected either as gas-phase SO_2 (pink) or 95 nm diameter sulfuric acid particles (orange). The blue, green, and red lines correspond to alumina particles with different radii, and the dashed lines assume that the fractal aggregates from coagulation become compact. For diamond (light green), the dotted line assumes that the $ClONO_2$ + HCl reaction does not occur (referred to as "no R1"). Generally, smaller particles result in greater ozone destruction, as their surface area for a specific radiative forcing is higher than for larger particles. The higher real part of the refractive index of diamond compared to alumina explains the smaller ozone change per radiative forcing compared to the case with the same size alumina particles. For both diamond and alumina, scenarios exist with lower ozone loss than for SO_2 or H_2SO_4. [From Weisenstein et al., 2015.]

The AER-2D model that includes the calcium carbonate chemistry of Dai et al. (2020) shows a small amount of ozone depletion (**Figure 6-19**, solid green line), in contrast to an enhancement in ozone at most latitudes when passivation is not accounted for (**Figure 6-19**, solid magenta line). In addition to the reactions studied in the lab by Dai et al. (2020; included in the solid lines in **Figure 6-19**), reactions involving $ClONO_2$ + HCl and $ClONO_2$ + HOCl would also affect ozone (green and magenta dashed lines in **Figure 6-19**). There is very limited understanding of this material under stratospheric conditions, so the rates of these unmeasured chlorine reactions, and additional currently unknown reactions, could have other potentially significant impacts on ozone, especially over the Antarctic regions (**Figure 6-19**). There are few experiments for how alternative materials could affect chemistry under more extreme polar vortex conditions. This complexity and the large number of heterogeneous surface reactions that are possible and the reactivity of materials such as calcium carbonate, whose surfaces will age and change composition over their

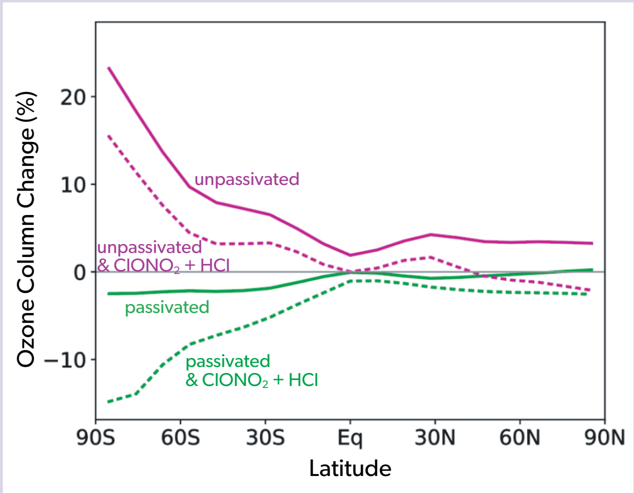

Figure 6-19. The impact on TCO of using calcium carbonate for SAI when considering the laboratory-observed passivation (green lines) or unpassivated assumption (magenta lines). Dashed lines show the relationship when accounting for the additional $ClONO_2$ + HCl reaction based on the Molina et al. (1997) alumina rates. [From Dai et al., 2020, Supplementary Material.]

stratospheric lifetimes, result in a high degree of uncertainty in the direct chemical impact of alternative materials on stratospheric ozone.

6.5.4 Paucity of Observations and Limited Model Capabilities

Overall, the state of knowledge of the impacts of alternative materials on stratospheric ozone is severely limited by a paucity of laboratory and field observations, particularly under stratospheric conditions. This limitation also has resulted in a very small number of modeling studies of alternative materials. Although it is likely that materials exist that result in decreased chemical and dynamical impacts on stratospheric ozone, any potential risks and tradeoffs are far from understood.

The impacts of SAI with the injection of alternative materials on ozone will depend on a number of additional uncertainties and higher-order effects. The coupling of chemistry and dynamics is just as important for alternative materials as it is for sulfate. Uncertainties are larger for alternative materials than for sulfate due to the much smaller number of studies; in addition, there is increased complexity resulting from the addition of a new component to the stratospheric composition. Interactions of alternative materials with background sulfate have not been quantified and could be significant. Unreactive materials such as diamond would become coated with sulfuric acid from coagulation and condensation, making them more reactive. Reactive species such as calcium carbonate would interact with sulfuric acid, nitric acid, and other constituents, affecting their properties. It is possible that coagulation of sulfuric acid particles with unreactive solid particles results in incomplete coatings. As with tropospheric aerosol mixtures, varying degrees of internal and external mixtures of composite aerosol particles are likely to be created. This increases the uncertainties in both optical and chemical properties of such particles and directly impacts the chemical and dynamical response of the perturbation. Thus, despite the potential for greatly reducing impacts on stratospheric ozone compared to sulfate, confidence in how alternative particles would affect the stratosphere and ozone, and therefore whether they are preferable to sulfate, is hindered by significant research gaps.

6.6 VOLCANOES AND PYROCUMULONIMBUS AS NATURAL ANALOGS TO SAI

As described in previous sections, ESM simulations show large uncertainties with regard to the effects of SAI on radiation, surface temperature, and other impacts, including ozone. Reducing these uncertainties would increase confidence in the projected impacts under different SAI scenarios and strategies. Natural analogs provide a unique opportunity for identifying shortcomings in models; these models are the only tools available to project future changes under SAI. The majority of coordinated ESM modeling experiments for studying the effects of SAI on the climate system use stratospheric SO_2 injections, thereby paralleling the periodic injections of SO_2 by explosive volcanic eruptions and their impacts on climate. Satellite measurements of radiative fluxes after the 1991 Mount Pinatubo eruption show a peak monthly-mean net top-of-atmosphere radiative flux anomaly between 60°S and 60°N of around -3 W m^{-2}. For context, by design the medium SAI GeoMIP G6sulfur simulations exert a continuous radiative forcing of approximately -4 W m^{-2} at the end of the 21st century (Kravitz et al., 2015).

Another natural analog of periodic aerosol injections into the stratosphere is when biomass burning creates pyrocumulonimbus (pyroCb) events. Such events occur when convection generated by the fire produces a cumulonimbus cloud that is sufficiently vigorous to transport both smoke and moisture into the lower stratosphere.

Both explosive volcanic eruptions and pyroCb events provide opportunities for benchmarking the current generation of aerosol and climate models against a wealth of observations (*Appendix 6A*). This includes testing the modeled spatial and temporal evolution of the aerosol distribution, microphysical properties, effects on radiation, and their impacts on stratospheric ozone. We restrict our assessment to the utility of analogies on aerosol microphysical and spatial distributions and their impacts on ozone. An assessment of how well the models represent the observed impacts of volcanic eruptions on climate impacts—such as surface cooling, a spin-down of the hydrological cycle, shifts in monsoon precipitation, and influences on key modes of climate variability—is provided in *Appendix 6A*, where the utility of pyroCb events in assessing models is also discussed.

6.6.1 Volcanic Eruptions as Analogs for SAI: Limitations and Opportunities

Measurements clearly show that large explosive volcanic eruptions, such as that of Mount Pinatubo in 1991, can perturb stratospheric ozone by increasing aerosol SAD for heterogeneous chemistry and catalytic ozone loss cycles, affecting ozone photolysis rates (e.g., Solomon, 1999, and references therein). In addition, there are indirect effects on ozone resulting from radiative heating of the stratosphere and subsequent circulation changes caused by the volcanic sulfate aerosol, similar to those described in *Sections 6.2* and *6.3*. Measurements after volcanic eruptions provide an opportunity to benchmark model performance and to understand the likely impact of SAI on ozone, because the same chemical and radiative heating processes are valid for volcanic eruptions and for SAI using SO_2 or other sulfate aerosol precursors (*Section 6.2*).

Detailed observations of SO_2 and resulting sulfate aerosols from small-magnitude eruptions between 2008 and 2019 using satellites, surface-based sun photometers, and surface-based lidars have provided insights into the microphysical evolution of stratospheric volcanic aerosols and their impacts on stratospheric transport (e.g., Muser et al., 2020; de Leeuw et al., 2021). These data have been used to assess and improve the representation of sulfur chemistry and microphysics in global climate models (e.g., Mills et al., 2016, 2017; Schmidt et al., 2018).

Measurements and model simulations of volcanic eruptions also provide a means for quantifying the expected stratospheric ozone changes resulting from SO_2 injections (*Section 6.2*). There are, however, clear limits to the analogy of volcanic aerosols with SAI, mainly because explosive eruptions produce pulsed injections of SO_2 into a relatively small area in the stratosphere, which contrasts with the continuous, decadal-long injection of SO_2 in strategically selected locations under most SAI scenarios. Continuous SAI applications contrast with the observations of a sudden increase in SAD, followed by a slow decline after a volcanic eruption. No large-magnitude volcanic eruptions during the satellite area have taken place during a very cold Arctic winter; as a result, current observations may underestimate the magnitude of polar ozone loss that could occur during long-term SAI applications (Tilmes et al., 2008). A continuously enhanced aerosol layer with SAI would have a longer-term impact on the stratospheric circulation than that from volcanic eruptions (see *Appendix 6A*). Other differences include the type of material injected under volcanic eruptions—which frequently inject volcanic ash, water vapor, and halogens, together with sulfur—and different climate response times to pulsed and continuous injections; these factors lead to differences in the ozone and climate response between volcanic eruptions and SAI (e.g., MacMynowski, et al., 2011; Duan et al., 2019).

In models, the availability of key oxidants such as OH becomes limited following volcanic eruptions (Bekki, 1996; Mills et al., 2017) due to the injection of large amounts of SO_2 into one or only a few model grid boxes. This affects the concentration and lifetime of SO_2, the rate of sulfate aerosol formation, and the growth of sulfate aerosol particles. Clyne et al. (2021) show that for pulsed SO_2 emissions, the injection strategy (i.e., single model grid box or along a band of longitudes) and the details of the OH chemistry representation (i.e., interactive or prescribed) lead to large differences in aerosol lifetime and stratospheric aerosol optical depth (AOD), similar to those across different SAI strategies (see *Section 6.3*). Many of the simulated differences between pulsed injections of SO_2 from volcanoes and continuous injections under SAI are caused by nonlinearities in sulfur oxidation chemistry and aerosol microphysics; SAI injections would occur in an already aerosol-laden atmosphere, which favors condensation and coagulation over nucleation (e.g., Laakso et al., 2017). Model simulations and observations reveal that aerosol dispersion during the initial stages of an eruption is strongly influenced by injection height and thus local meteorology (e.g., Bourassa et al., 2012; Jones et al., 2016b; de Leeuw et al., 2021). On the other hand, for continuous SAI, which takes place over several years, the interannual differences in the aerosol distribution are small and less dependent on initial meteorological conditions (e.g., Tilmes et al., 2017; Visioni et al., 2019).

With volcanic eruptions, there are commonly co-emissions of species other than sulfur (such as volcanic ash, halogens, and water vapor), whereas under SAI this would generally not be the case. Many co-emitted species can affect the aerosol lifetime, oxidation rates, and radiative heating rates and can cause lofting of sulfur species to higher altitudes (Zhu et al., 2020; Muser et al., 2020; Niemeier et al., 2020; Kloss et al., 2021; Stenchikov et al., 2021). Disentangling and quantifying the effects of co-emitted species on sulfate aerosol lifetimes and dispersion in observations is difficult. Modeling studies provide indications of the relative rate at which different co-emitted species affect heating rates and lofting (Muser et al., 2020; Kloss et al., 2021; Stenchikov et al., 2021). Some volcanic co-emissions such as halogens can also directly affect stratospheric ozone under present-day ozone-depleting substance levels, as well as indirectly affect stratospheric heating rates and thus water vapor concentrations (e.g., Staunton-Sykes et al., 2021, and references therein). In addition, future research may suggest that the optimum SAI strategy is to inject H_2SO_4 instead of SO_2 (*Section 6.2*) or to use a completely different substance (*Section 6.5*), further limiting the analogy between volcanic eruptions and SAI.

6.6.2 Model Simulations of Volcanic Effects on Ozone

Following the June 1991 Mount Pinatubo eruption, satellite and ozonesonde data show a loss of ozone in the lower stratosphere, particularly in winter and spring in polar regions between 1991 and 1993 (e.g., Grant et al., 1992; Randel et al., 1995; *Chapters 3* and *4*). Total column ozone was reduced by up to 8% in the first month after the eruption in the tropics and by up to 10% in the Northern Hemisphere. Ozone depletion in the aerosol plume was much higher, reaching around 20% at altitudes between 24 km and 25 km (McCormick et al., 1995). In the mid-latitudes of the Southern Hemisphere, increases in total column ozone of up to 10 DU were observed in the middle stratosphere between July and December 1991, likely caused by both chemical and dynamical changes (e.g., Koike et al., 1994; Van Roozendael et al., 1997). Recent modeling studies suggest that the volcanically induced dynamical perturbation played a key role in transporting ozone from the tropics to the extratropics of the Southern Hemisphere, thus explaining the lack of ozone depletion there (Pitari and Mancini, 2002; Poberaj et al., 2011; Aquila et al., 2013; Dhomse et al., 2014). The same modeling studies suggest that after about six months heterogeneous chemical ozone loss dominates, with additive effects of the initial dynamical perturbation and the chemical perturbation due to the volcanic aerosols. Following the eruption of Mount Pinatubo, a maximum decrease in total column nitrogen dioxide (NO_2) of about 35% in both the Arctic and at mid-latitudes in January 1992 is evident, with a recovery to background values by August 1995 (Van Roozendael et al. 1997). Maximum reductions in local NO_2 concentrations of up to 60% were measured in the lower stratosphere at around 22 km altitude in summer 1992 (Johnston et al., 1992; Van Roozendael et al., 1997; Danilin et al., 1999) and correlated well with the 40-fold (or more) increase in the aerosol SAD (Thomason et al., 1997). Similar measurements exist for nitric oxide (NO), suggesting a role for nitrogen pentoxide (N_2O_5) hydrolysis with increasing SAD, which has been found in various model studies applying SAI.

Studies that isolate the effect of increased volcanic aerosol find good correlation between modeled SAD and observed ozone depletion (Wilka et al., 2018); these increases in SAD are associated with large- and small-magnitude volcanic eruptions, suggesting that heterogeneous chemistry was the primary driver of increased ozone loss between 1980 and 2014 (when halogen stratospheric concentrations were high). The 1991 Mount Pinatubo eruption, which caused the largest observed polar ozone perturbation to date, did not emit significant amounts of chlorine or other halogen compounds that could have catalyzed ozone loss. Measurements after the 1982 El Chichón eruption support the same mechanisms for ozone loss, with increases in aerosol SAD of up to 50 μm^2 cm^{-3} at mid-latitudes between 18 km and 20 km in early 1983 (Hofmann and Solomon, 1989). In this case, the eruption might have injected HCl into the stratosphere, with observed column HCl enhancements above 12 km altitude between 22°N and 35°N on the order of 40% in the first six months post-eruption (Mankin and Coffey, 1984). This would have amplified the catalytic depletion of total column ozone, which reached more than 10% after the eruption (Hofmann and Solomon, 1989). The difference in **Figure 6-20** between the blue and the orange curves, which show the evolution of ozone in a model simulation with and without volcanic aerosols, respectively, supports this view. The aerosol-free simulation shows no increase in the rate of ozone depletion above the overall trend in the years affected by the 1991 Mount Pinatubo eruption and a significantly decreased effect in the years affected by the 1982 El Chichón eruption.

Measurements and modeling studies show that since the 1991 Mount Pinatubo eruption, a series of small-magnitude eruptions have contributed to polar ozone depletion in Antarctica (**Figure 6-21**; Solomon et al., 2016; Wilka et al., 2018; Stone et al., 2017; Zhu et al., 2018). Measurements show that in 2015, the Antarctic ozone hole was particularly large and long-lasting, which in models and observations has been attributed to the existence of a very cold and undisrupted stratospheric polar vortex combined with the impacts of the April 2015 Calbuco eruption

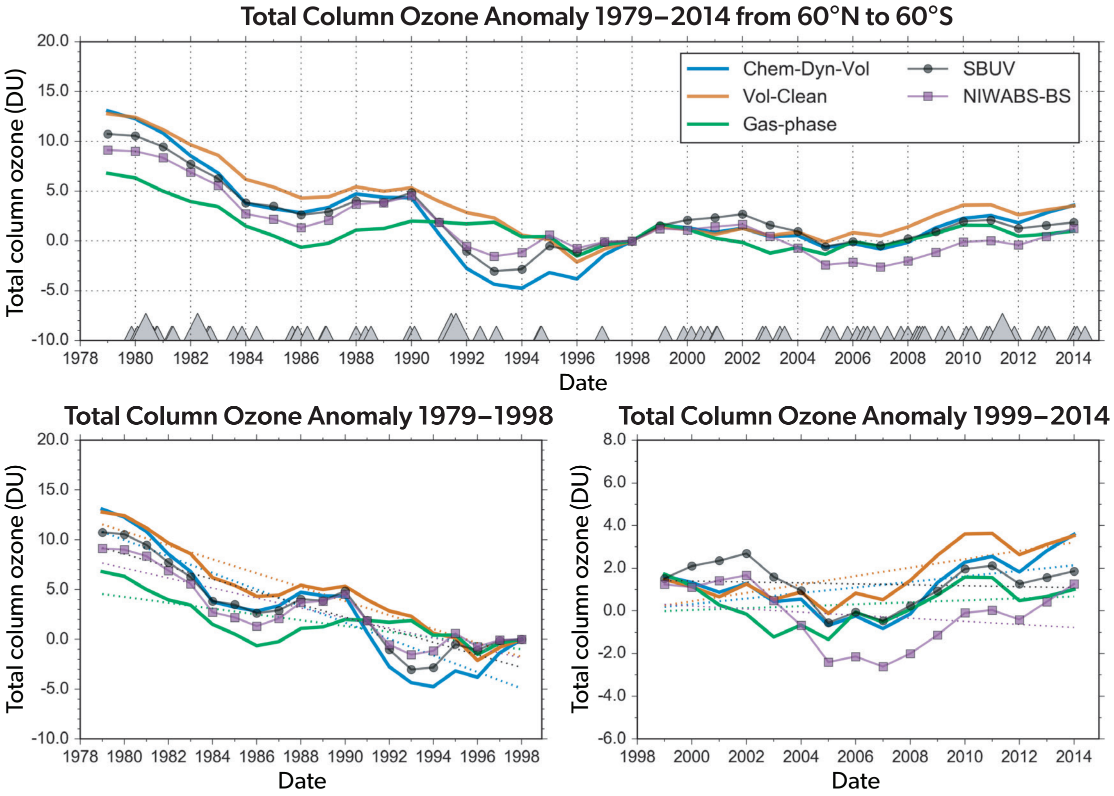

Figure 6-20. *(top)* Time series of model-simulated three-year running mean of 60°N–60°S total column ozone anomalies with respect to 1998 values from 1979 to 2014 with gas-phase, Vol-Clean, and Chem-Dyn-Vol runs shown as green, orange, and blue solid lines, respectively. The Chem-Dyn-Vol run includes full chemistry, specified dynamics, and volcanic aerosols taken from the Neely and Schmidt (2016) database; the Vol-Clean run has no volcanic aerosols but all other processes; and the gas-phase run turns off all heterogeneous chemistry. Solar Backscatter Ultraviolet and National Institute of Water and Atmospheric Research-Bodeker Scientific total column ozone data are shown by the black line with circles and the purple line with squares, respectively. Grey triangles at the bottom indicate volcanic eruptions, with the larger triangles indicating eruptions of Volcanic Explosivity Index 5 and 6. *(bottom)* Time series of anomalies in global mean total column ozone and their respective linear fits for the periods 1979–1998 *(left)* and 1999–2014 *(right)*. [From Wilka et al., 2018, with fit parameters given in Table 1 of that publication.]

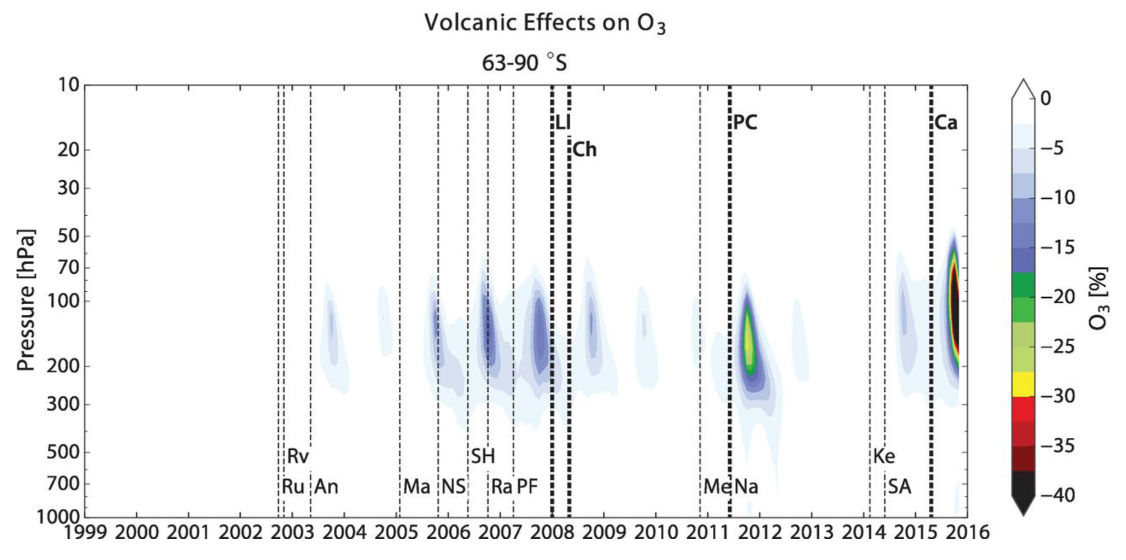

Figure 6-21. Model-calculated percentage changes in ozone concentrations in Antarctica (63–90°S) due to a series of small-magnitude volcanic eruptions. Tropical eruptions are shown at the bottom and higher-latitude eruptions at the top. Abbreviations: An, Anatahan; Ca, Calbuco; Ch, Chaitén; Ke, Kelut; Ll, Llaima; Ma, Manam; Me, Merapi; Na, Nabro; NS, Negra Sierra; PC, Puyehue-Cordón Caulle; PF, Piton de la Fournaise; Ra, Rabaul (also referred to as Tavurvur); Ru, Ruang; Rv, Reventador; SA, Sangeang Api; SH, Soufrière Hills. [From Solomon et al., 2016.]

in Chile (*Chapter 4*; Solomon et al., 2016; Wilka et al., 2018; Stone et al., 2017; Zhu et al., 2018; Rieger et al., 2021). Based on observations and model simulations, Berthet et al. (2017) show that after the 2009 Sarychev eruption, NO_2 was depleted to a similar degree as following the 1991 Mount Pinatubo eruption, but ozone loss was relatively limited at 16 km and smaller in magnitude than during Pinatubo by at least a factor of 10. These observations and model simulations provide useful guidance on the expected effects of SAI on ozone and indicate that even small aerosol injections, as during the onset period of SAI, can have a significant impact on ozone.

6.6.3 Model Simulations of Volcanic Aerosol Properties

Most Earth system models participating in the CMIP6 model intercomparison used in the latest IPCC assessment (Lee et al., 2021) use prescribed stratospheric volcanic aerosol datasets derived either from observations (e.g., Thomason et al., 2018; Kovilakam et al., 2020) or a blend of observations and models (Arfeuille et al., 2014). Model intercomparisons conducted under CMIP6 and dedicated to volcanic eruptions, such as the Volcanic Forcings Model Intercomparison Project (VolMIP), stipulate a

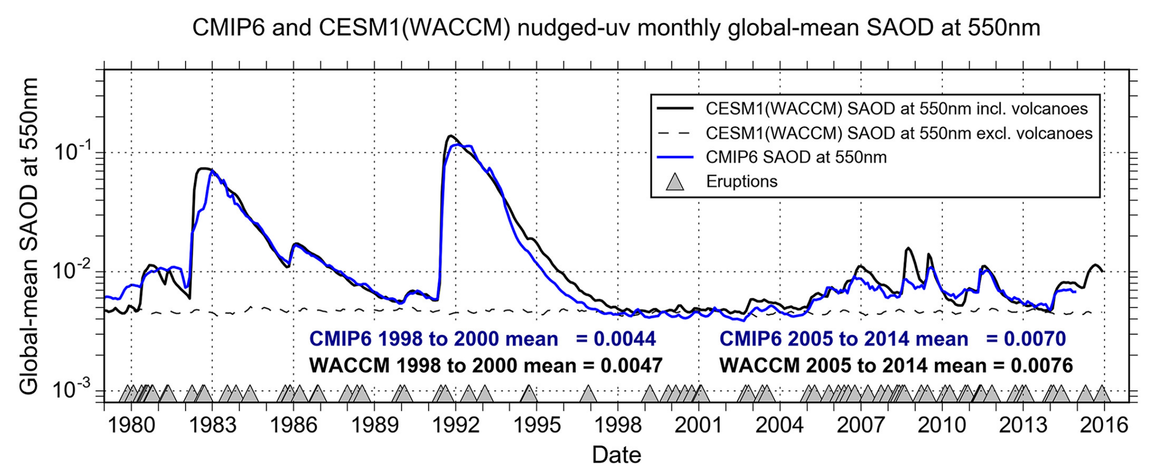

Figure 6-22. Comparison of satellite-based (blue line) and model-simulated (solid black line: including volcanic SO_2 emissions; dashed black line: omitting volcanic SO_2 emissions) monthly global mean stratospheric aerosol optical depth (SAOD) at 550 nm. [From Schmidt et al., 2018.]

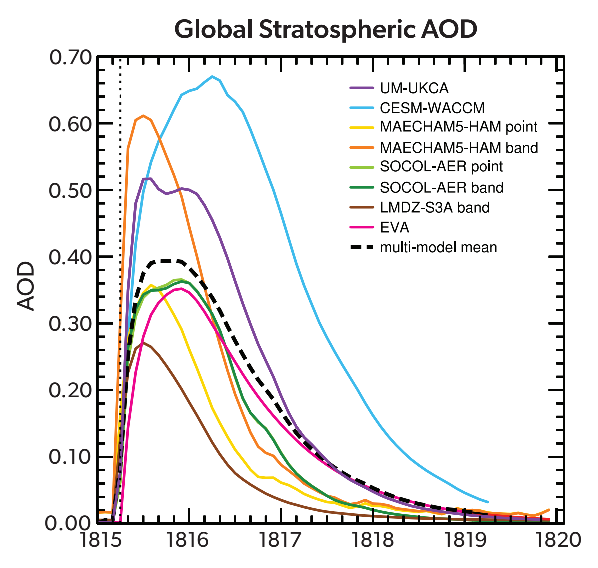

Figure 6-23. Ensemble averaged, global mean stratospheric AOD (at 550 nm) as simulated for an 1815 Mount Tambora–type eruption emitting 60 Tg of SO_2, using different models. The black line is the mean of the CESM-WACCM (blue), UM-UKCA (purple), SOCOL-AER point (light green), MAECHAM5-HAM point (gold), LMDZ-S3A band (dark brown), and EVA (red) models. Results for the SOCOL-AER band and MAECHAM5-HAM band models using different injection approaches are shown in dark green and orange, respectively. The vertical dotted line marks the date of injection of SO_2, which is slightly offset from the zero AOD in the models due to the temporal resolution of the model output and curve smoothing. [From Clyne et al., 2021.]

standardized protocol whereby prescribed aerosol datasets are used to ensure that the spatial distribution of aerosols is consistent. This allows quantification of model uncertainty in the response of ozone and climate to a volcanic forcing (Zanchettin et al., 2016) without confounding issues arising from, for example, differences in the implementation of volcanic emissions (Clyne et al., 2021).

Models with interactive aerosol and chemistry schemes use volcanic SO_2 emissions as input. **Figure 6-21** shows that climate models with detailed aerosol and sulfur chemistry schemes nudged to meteorological reanalyses can simulate stratospheric AOD under volcanically quiescent and perturbed conditions and are in good agreement with satellite-based measurements (Mills et al., 2016; Schmidt et al., 2018). After the two recent large volcanic eruptions of El Chichón in 1982 and Mount Pinatubo in 1991, models reveal that between 2005 and 2014, a series of small-magnitude eruptions doubled the total stratospheric AOD compared to volcanically quite periods (**Figure 6-22**; Kovilakam et al., 2020; Schmidt et al., 2018; Thomason et al., 2018; Mills et al., 2016).

No direct measurements exist for larger SO_2 perturbations, and confidence in interactive sulfate aerosol and sulfur chemistry schemes is much lower for SO_2 injections greater than 10–20 Tg of SO_2. For example, for very-large-magnitude eruptions emitting 60 Tg of SO_2 (which is representative of the 1815 Mount Tambora eruption), a model intercomparison reveals large inter-model differences in the simulated magnitude of the volcanic forcing and surface temperature response, despite the models using the same eruption source parameters (Zanchettin et al., 2016). Clyne et al. (2021) show that for eruptions emitting 60 Tg of SO_2, the magnitude and timing of the peak in global mean stratospheric aerosol optical depth and effective radius differ substantially across simulations (**Figure 6-23**). Such emissions levels are extremely large compared to those under the peakshaving and medium SAI scenarios and are at the extreme end of strong SAI scenario.

Recent studies also suggest that there is uncertainty in the effective radiative forcing diagnosed in models for large explosive eruptions such as Mount Pinatubo in 1991. Rapid adjustments and the cloud response to a volcanic forcing are particularly large sources of this uncertainty (e.g., Gregory et al., 2016; Marshall et al., 2020; Schmidt et al., 2018). There is also substantial uncertainty in the stratospheric heating rates and the subsequent dynamical response simulated in models following explosive eruptions (e.g., Driscoll et al., 2012; Zambri et al., 2017), as also reflected in SAI simulations (**Figure 6-9**). Uncertainties in heating rates and dynamical responses have implications for the hemispheric distribution of the sulfate aerosols, which in turn affects ozone chemistry (e.g., as discussed in Aquila et al., 2013, for Mount Pinatubo).

Model configuration and model specifics such as the vertical resolution in the stratosphere and the details of the radiative transfer scheme affect the magnitude of the diagnosed volcanic forcing, which is also the case for SAI studies (*Section 6.2.2*). Although no systematic uncertainty assessment has been carried out to date, Hansen et al. (2002) estimate that these model uncertainties equate to uncertainties in radiative forcing of between 15% and 50%, depending on the eruption specifics. Many of the discrepancies have common causes and can largely be explained either by missing first-order model physics, chemistry, or other processes (Clyne et al., 2021). As in SAI simulations, the use of sectional versus modal aerosol schemes can have a very large effect on the results (e.g., English et al., 2013; Laakso et al., 2021).

Overall and despite limitations, volcanic eruptions offer an opportunity to benchmark current-generation aerosol and climate models against a wealth of observations. In particular, small-magnitude volcanic eruptions that have occurred over the satellite era have the benefit of a greater number of higher-quality observations and can be used for refining emissions estimates and injection altitudes (e.g., de Leeuw et al., 2021) and for detailed assessment of the performance of models with respect to their predicted effects on ozone, as well as the temporal and spatial evolution of both SO_2 and the resulting sulfate aerosol plume (e.g., Haywood et al., 2010; Muser et al., 2020). These observations can help improve our understanding of the underlying physical and chemical processes, as well as the uncertainties involved in SAI proposals.

APPENDIX 6A : OBSERVATIONS AND VOLCANIC IMPACTS ON CLIMATE

6A.1 OBSERVATIONS

Observational constraints for model simulations of the evolution of stratospheric plumes of SO_2 and the resulting sulfate, as well as biomass-burning aerosol plumes from pyrocumulonimbus, are available from a number of sources. Satellite retrievals include estimates of the SO_2 injection amounts and altitudes from instruments operating in the UV (e.g., TROPOMI) and IR (IASI) spectral regions (e.g., Karagulian et al., 2010; Clarisse et al., 2012; Theys et al., 2017; de Leeuw et al., 2021).

Once SO_2 is oxidized and processed to optically active sulfate aerosol, limb-sounding instruments (e.g., SAGE I–III, Baumann et al., 2003; OSIRIS, Bourassa et al., 2012; OMPS, Kloss et al., 2021) and lidar instruments (e.g., CALIPSO, Vernier et al., 2011; CATS, Christian et al., 2019) are able to measure the spatial distribution and the altitude of the resulting aerosol plume. Detecting sulfate aerosols from traditional nadir-viewing instruments operating at visible wavelengths is difficult owing to the presence of underlying clouds. Absorbing aerosols can be detected using UV wavelengths, as is done for absorbing smoke aerosols (e.g., TROPOMI; Torres et al., 2020). Ground-based remote sensing instrumentation also provides essential validation for models in the form of lidar systems (e.g., Barnes and Hoffman, 1997; Chazette et al., 1995) and high-altitude sun-photometer sites such as Mauna Loa that are at a sufficiently remote location and at a sufficient altitude to be largely uninfluenced by tropospheric aerosols (e.g., Haywood et al., 2010). There are also a limited number of recent aerosol observations from routine long-haul flights of the IAGOS/CARIBIC network that are providing new insights into stratospheric aerosol evolution and modeling capabilities for both volcanic sulfate and biomass-burning smoke in the upper troposphere and lower stratosphere (e.g., Osborne et al., 2022). Balloon-borne measurements with optical particle counters yield additional high-quality stratospheric aerosol data that provide essential information on the microphysical evolution of aerosol size distributions (e.g., Deshler et al., 2003).

6A.2 VOLCANIC EFFECTS ON RADIATIVE FORCING AND TEMPERATURE

Since 1978, satellite remote sensing has provided measurements of volcanic SO_2 emissions from over 1000 volcanic eruptions, yielding an average SO_2 emissions rate from explosive and effusive eruptions of 3 Tg SO_2 yr^{-1} between 1978 and 2021, of which an average of about 1 Tg SO_2 yr^{-1} is injected into the stratosphere (Carn et al., 2016, 2017). However, there is significant interannual variability in the emissions into the stratosphere, with some years receiving negligible SO_2 from explosive volcanic eruptions and others having many times the longer-term mean annual injection rate. Between 2008 and 2019, small-magnitude eruptions such as those of Kasatochi in 2008 (Kravitz et al., 2010), Sarychev in 2009 (Haywood et al., 2010), and Raikoke in 2019 (Kloss et al., 2021; de Leeuw et al., 2021) have each injected around 1.5 Mt of SO_2 into the stratosphere.

The sudden increase in stratospheric sulfate aerosol mass and number concentration from volcanic SO_2 injections changes the size distribution of stratospheric aerosols and increases the aerosol SAD compared to volcanically quiescent periods. The latter largely explains heterogeneous chemistry-induced ozone changes, and the nature of the change in the aerosol bulk properties. In particular, the injected mass and particle size dictate the strength of the climate perturbations following eruptions (Pinto et al., 1989; Lacis et al., 1992; Timmreck et al., 2010). Compared to the volcanically quiescent period prior to the eruption, the eruption of Mount Pinatubo in 1991 caused a 60-fold increase in the stratospheric sulfate burden (McCormick et al., 1995), an increase in particle number concentrations of 2 orders of magnitude (Deshler et al., 2003), and a 40-fold increase in the SAD (Thomason et al., 1997). Satellite measurements of radiative fluxes after the 1991 Mount Pinatubo eruption show a peak monthly mean net top-of-atmosphere radiative flux anomaly between 60°S and 60°N of around -3 W m^{-2}. For context, by design the medium SAI GeoMIP G6sulfur simulations exert a continuous radiative forcing of approximately -4 W m^{-2} at the end of the 21st century (Kravitz et al., 2015). Measurements from the period of the Mount Pinatubo eruption have been used to test global model simulations, revealing reasonable model performance (Minnis et al., 1993; Mills et al., 2017; Schmidt et al., 2018). The relationship between the mass of SO_2 emitted and the resulting climate effect are nonlinear (Pinto et al., 1989; Timmreck et al., 2009) because of a combination of OH radical oxidation chemistry limiting H_2SO_4 vapor production (and thus sulfate aerosol burden) and an enhanced coagulation of numerous small particles leading to rapid shifts in the particle size distribution toward very large sizes. These findings predated similar findings from SAI climate intervention strategies (e.g., *Section 6.2.3.1*) and have been key to adjusting modeled emissions scenarios and strategies to minimize such impacts (e.g., *Section 6.2.3.2*).

Analysis of instrumental temperature records, for which low-frequency climate variations and the influence of El Niño-Southern Oscillation (ENSO) have been removed, suggest a maximum post-eruption global mean surface cooling of 0.2–0.3 K when averaged for the eruptions of Krakatau (1883), Santa Maria (1902), Katmai (1912), Agung (1963), El Chichón (1982), and Pinatubo (1991; Robock and Mao, 1995; Robock, 2000). The 1991 Mount Pinatubo and Cerro Hudson eruptions emitted approximately 10–15 Tg of SO_2 into the stratosphere, which resulted in a peak global mean near-surface cooling of ~0.3–0.5 K in mid-1992 (e.g., McCormick et al., 1995; Soden et al., 2002; Thompson and Solomon, 2009) and a warming of up to 3.5 K in the tropical stratosphere (Labitzke, 1994, Labitzke and McCormick, 1992). Note that the surface temperature response

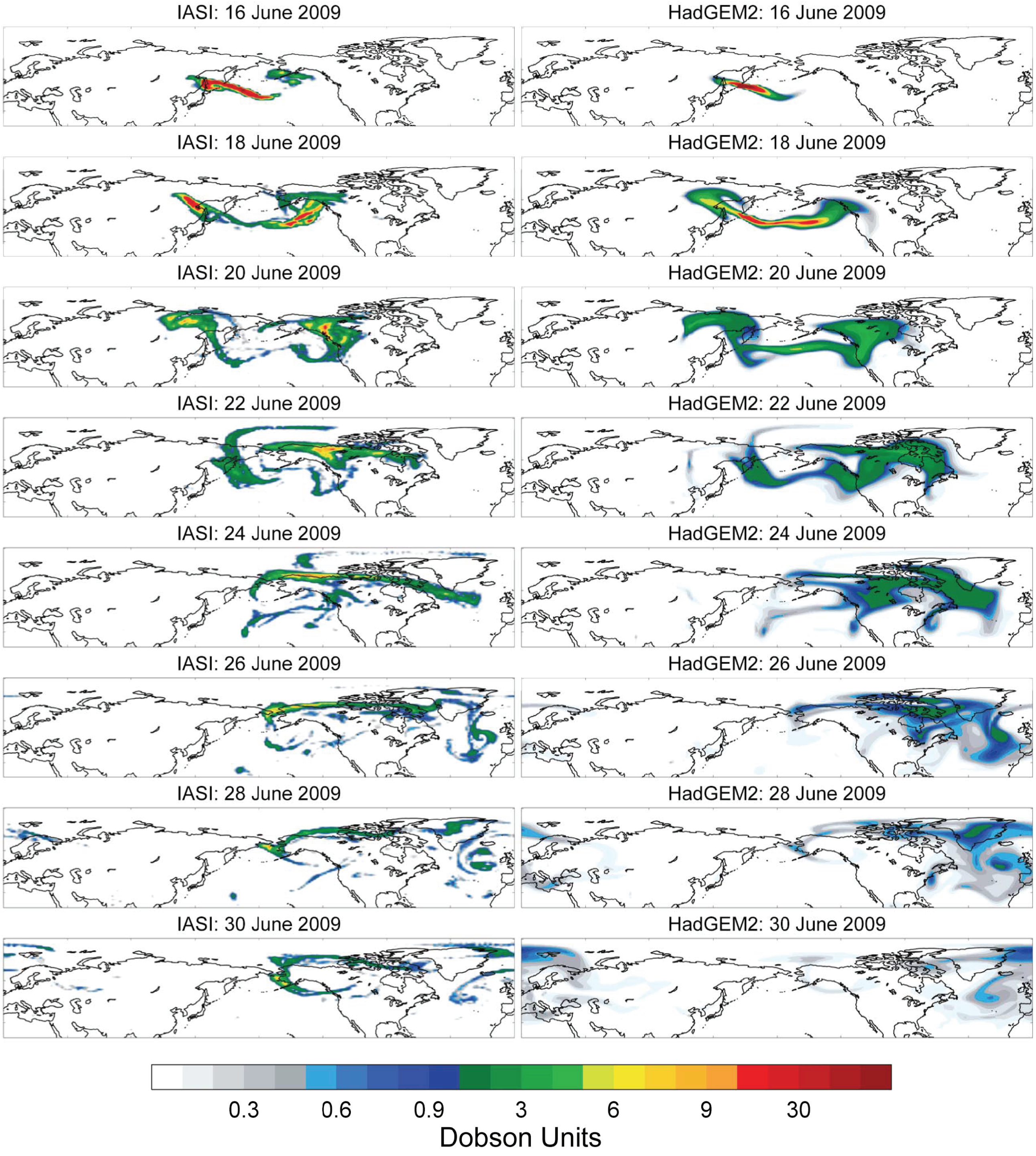

Figure 6A-1. Panels show the evolution of the plume of SO_2 from the Sarychev eruption. The column on the left represents observations from the IASI sensor, while that on the right represents model simulations from the HadGEM2 climate model. [From Haywood et al., 2010.]

was influenced by the strong El Niño event in 1991–1994 (e.g., Lehner et al., 2016) and other dynamical feedbacks (Soden et al., 2002). Typically, the surface temperature response over land is detectable for two to three years. Using SAI, continuous emissions of 8–16 Tg of SO_2 yr^{-1} would be required to cool the Earth by 1 K (*Section 6.2*); it is acknowledged that there are many differences in the atmospheric and climatic responses between pulse and continuous injections (e.g., Duan et al., 2019). The duration, magnitude, and spatial pattern of the surface temperature response following volcanic eruptions depends on eruption characteristics such as the mass of SO_2 emitted, eruption season and latitude (e.g., Marshall et al., 2020), and local meteorology (Jones et al., 2016b) and climatological conditions prior to the eruption (e.g., Robock and Mao, 1995). Instrumental records also show a warming of the North American and Eurasian continents by 2 K or more during the first or second winter after large explosive eruptions (Robock and Mao, 1992), which is consistent with a forced positive North Atlantic Oscillation (NAO) response, but the magnitude of any causal link and the driving mechanism is still debated (Polvani et al., 2019).

6A.3 VOLCANIC EFFECTS ON CLIMATE DYNAMICS

Radiative heating of the lowermost tropical stratosphere following tropical explosive eruptions leads to an increased meridional temperature gradient and enhanced upwelling in the tropical stratosphere, similar to what has been described for SAI applications. This leads to enhanced transport of ozone from the tropical stratosphere toward higher latitudes (Kinne et al., 1992; Tilmes et al., 2004) and a strengthening of the polar vortex (e.g., Bittner et al., 2016), which further enhances polar ozone loss.

Dynamical processes affecting ozone concentrations are intertwined with chemical processes in the same regions, and they thus potentially mask or enhance some of the chemical loss of ozone following an eruption. The QBO and ENSO phase contribute to year-to-year variability in stratospheric ozone concentrations and further complicate the attribution of individual processes to ozone loss (e.g., Telford et al., 2009). Changes in stratospheric ozone concentrations at mid-latitudes are closely linked to dynamical and radiative perturbations induced by volcanic eruptions in modeling studies (e.g., Telford et al., 2009; Aquila et al., 2013; Dhomse et al., 2014); this is similar to what has been found in SAI modeling studies. In addition, there are feedbacks between stratospheric ozone loss and stratospheric temperature variability in that stratospheric ozone loss results in less UV absorption, which in turn affects the aerosol heating rate (Kinne et al., 1992; Rosenfeld et al., 1997).

Volcanic eruptions can also provide guidance on the specific SAI deployment strategies and the expected impacts. Observations and climate models reveal that volcanic eruptions can cause reductions in global precipitation, with complex regional precipitation responses (e.g., Iles et al., 2013; Trenberth and Dai, 2007). Such a spin-down of the hydrological cycle is also observed in many SAI simulations (e.g., Kravitz et al., 2013). After the high-latitude eruption of Katmai (1912), where stratospheric AODs were enhanced in the Northern Hemisphere, models simulate a significant shift of rain-bearing clouds associated with the intertropical convergence zone (ITCZ) toward the south. Two consequences of this shift were observed historic minimum river flows in both the Nile and Niger Rivers (e.g., Oman et al., 2006) and the lack of any Atlantic hurricanes (Evan, 2012). Such features appear to be due to the asymmetry of hemispheric stratospheric AODs, and this appears to be well represented in model simulations of both volcanic eruptions and SAI (Haywood et al., 2013; Jones et al., 2017). Recognition of these features has contributed to efforts to minimize inter-hemispheric temperature gradients in SAI strategies (e.g., MacMartin et al., 2014a; **Box 6-2**).

SAI-induced heating in the lower tropical stratosphere will have a long-term effect on stratospheric dynamics (Aquila et al., 2014) that does not recover after a few years, as it does for volcanic eruptions (Brenna et al., 2021). Effects on the QBO, stratospheric water vapor concentrations, and ozone will therefore differ in magnitude and longevity between SAI and volcanic eruptions. For example, Aquila et al. (2014) and Jones et al. (2022) suggest that the QBO phase could be severely disrupted and potentially locked into the westerly phase by SAI under medium SAI scenarios, although specific SAI strategies outside of the immediate equatorial region have been developed to mitigate that effect (Richter et al., 2017, 2018; Kravitz et al., 2019; Franke et al., 2021). In models, a positive phase of the NAO and associated continental winter warming and increased precipitation over northern Europe is a robust signal in simulations of SAI (Banerjee et al., 2021; Jones et al., 2021, 2022) but not in simulations of volcanic eruptions (e.g., Polvani et al., 2019). Continuous decadal-scale injections of sulfur will lead to a continuous reduction in surface warming (or to surface cooling, depending on the SAI application), albeit smaller in magnitude than for pulsed volcanic SO_2 emissions (Duan et al., 2019), while the effects of volcanic eruptions are shorter lived.

6A.4 PYROCONVECTION EVENTS AS NATURAL ANALOGUES FOR SAI

Extreme wildfires can generate deep thunderstorms (or pyroCbs), which can inject large amounts of particles, water vapor, and other biomass-burning emissions into the stratosphere (Fromm et al., 2010). The pyroCb biomass-burning particles, which consist of organic carbon, inorganic components, and a significant fraction of black carbon (e.g., Wu et al., 2021), are transported within the stratosphere and have a residence time of months. For example, the stratospheric e-folding residence time of the 2017 Pacific Northwest (wildfire) Event (PNE) was about five months (Yu et al., 2019). The resulting particles can scatter sunlight back to space, absorb solar and terrestrial radiation, and impact the chemical and radiative equilibrium in the stratosphere. While biomass-burning aerosols have not been suggested as candidate SAI particles because of their strong radiative heating (Kravitz et al., 2012; Haywood et al., 2022), observations of pyroCb aerosols are useful for model evaluation purposes. However, the strong radiative heating could potentially be used to loft aerosols from the mid-troposphere to the stratosphere. Gao et al. (2021) estimate that black carbon with a concentration of 10 microgram per cubic meter could be sufficient to loft SAI material from 13.5 km to ~20 km, utilizing solar absorption and the resulting lofting to reach the needed altitudes.

A number of pyroCb events have been identified and analyzed using satellite measurements since the year 2000 (Fromm et al., 2010). Among them, the 2017 PNE (Peterson et al., 2018; Khaykin et al., 2018; Yu et al., 2019; Torres et al., 2020) and the

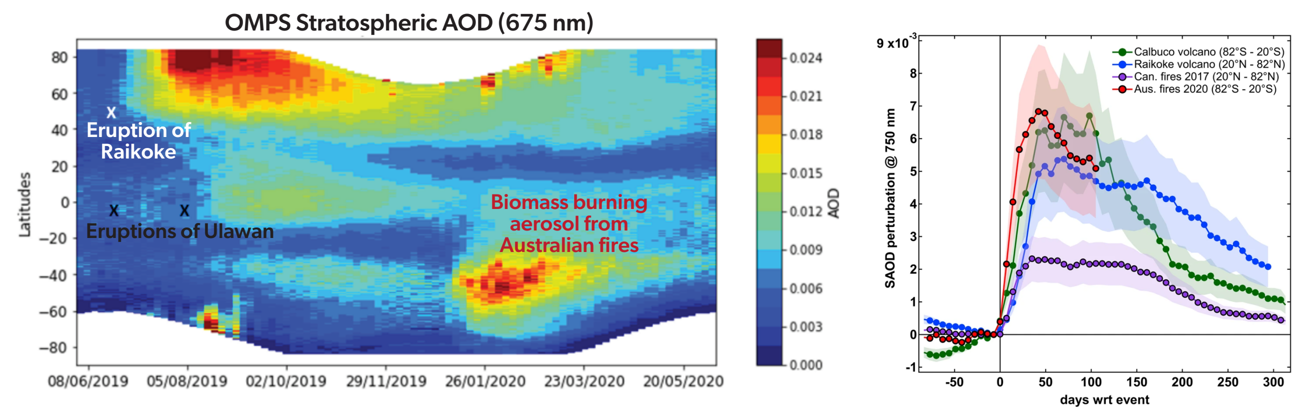

Figure 6A-2. *(left)* Stratospheric AODs from the Southeast Australia fires, compared to those from Raikoke and Ulawan eruptions (adapted from Kloss et al., 2021). *(right)* Stratospheric AOD from the 2017 PNE and 2019–2020 Australian fires, compared to that from the 2015 Calbuco and 2019 Raikoke volcanoes. [Adapted from Khaykin et al., 2020.]

2019–2020 Southeast Australia New Year (SEANY; Khaykin et al., 2020; Kablick et al., 2020; Kloss et al., 2021; Schwartz et al., 2020; Yu et al., 2021; Peterson et al., 2021; Rieger et al., 2021; Damany-Pearce et al., 2022) events injected the largest amounts of biomass-burning aerosols into the stratosphere. The estimated mass injected into the stratosphere by the PNE was 0.1–0.3 Tg (Peterson et al., 2018). Estimates of the injected mass for the SEANY event range from 0.2 to 3.1 Tg (Khaykin et al., 2020; Yu et al., 2021; Hirsch and Koren, 2020), which is comparable to the ~1.5 Tg SO_2 emissions from the Kasatochi volcano (2008) in the Aleutian Islands and the emissions from the Sarychev (2009) and Raikoke (2019) volcanic eruptions in the Kuril Islands. The perturbation of the global mean SAOD at mid-visible wavelengths by the SEANY biomass-burning particles is close to that from the Calbuco (2015) and Raikoke volcano eruptions (**Figure 6A-2**). In each of these cases, the stratospheric AOD perturbation takes over one year to return to background values (Khaykin et al., 2020; Damany-Pearce et al., 2022).

The number and scope of pyroCb modeling studies are relatively limited compared to those for volcanic eruptions. Modeling studies (Christan et al., 2019; Yu et al., 2019; Das et al., 2021; Yu et al., 2021; Osborne et al., 2022) show that the spatial-temporal distributions of the pyroCb biomass-burning particles can generally be well simulated by operational atmospheric dispersion and climate models. These model simulations assume emissions rates and use profiles derived from satellite retrievals as constraints and have been validated using downstream satellite retrievals, surface-based lidar observations, and in situ aircraft observations (e.g., Osborne et al., 2022). However, the present pyroCb modeling is far from sufficient for a comprehensive understanding of key processes and impacts, based on the following shortcomings.

Remote sensing measurements show that significant amounts of water vapor, carbon monoxide, and acetonitrile were also lofted into the stratosphere during the SEANY pyroCb biomass-burning plumes (Schwartz et al., 2020; Khaykin et al., 2020). Airborne and balloon-borne in situ measurements of the pyroCb biomass-burning plume composition are necessary to quantify the emissions, but these measurements are extremely rare at present. As a result, the composition and chemical and physical properties of the plume and the biomass-burning aerosol remain unclear, which prevents a comprehensive understanding of the climate implications of the pyroCb biomass-burning particles.

Wildfire-generated pyroconvection transports large amounts of aerosols and other biomass-burning emissions into the upper troposphere in hours (Peterson et al., 2018). In models, this process occurs at the sub-grid scale; convection and thunderstorms are usually too small to be fully captured by climate models, which typically have a spatial resolution of about 100 kilometers and a temporal resolution of about 1 hour. For this reason, in climate models (Christan et al., 2019; Yu et al., 2019; Das et al., 2021; Yu et al., 2021) pyroCb biomass-burning particles are injected directly into the upper troposphere, and the injection height and area are approximated using observations from remote sensing a day or so after the fire starts.

Measurements and modeling studies suggest that the pyroCb smoke may significantly affect stratospheric ozone through similar heterogeneous reactions on the surface of the volcanic or SAI sulfate aerosols (*Sections 3.2.1.3* and *4.2.3.2*). Recent studies have implicated the SEANY fires and the resulting biomass-burning aerosol particles as a potential contributor to the anomalously deep and long-lived ozone hole that occurred in 2020 (e.g., Rieger et al., 2021; Solomon et al., 2022; Yook et al., 2022; Damany-Pearce et al., 2022). Due to insufficient knowledge on the heterogeneous reaction rate on the surface of organic aerosols, especially those (partly) coated with sulfuric acid, the estimated ozone loss caused by the pyroCb biomass-burning particles is highly uncertain.

To reproduce these pyroCb events, climate models would need to include interactive aerosol-radiation feedbacks, sufficient stratospheric chemistry (e.g., heterogeneous chemistry, halogen chemistry, etc., which have not been studied for stratospheric biomass-burning aerosols), and accurate representation of the stratospheric background and volcanic aerosols. The injected particles can coagulate and grow in the stratosphere for months, and the effective size of the particles can evolve. Consequently, the size-evolving related aerosol microphysics needs to be well represented in climate models.

REFERENCES

Angell, J.K., and J. Korshover, Comparison of tropospheric temperatures following Agung and El Chichón volcanic eruptions, ***Mon. Weather Rev.***, ***112*** (7), 1457–1463, doi:10.1175/1520-0493(1984)112<1457:COTTFA>2.0.CO;2, 1984.

Aquila, V., L.D. Oman, R. Stolarski, A.R. Douglass, and P.A. Newman, The response of ozone and nitrogen dioxide to the eruption of Mount Pinatubo at southern and northern midlatitudes, ***J. Atmos. Sci., 70*** (3), 894–900, doi:10.1175/JAS-D-12-0143.1, 2013.

Aquila, V., C.I. Garfinkel, P.A. Newman, L.D. Oman, and D.W. Waugh, Modifications of the quasi-biennial oscillation by a geoengineering perturbation of the stratospheric aerosol layer, ***Geophys. Res. Lett.***, ***41*** (5), 1738–1744, doi:10.1002/2013GL058818, 2014.

Arfeuille, F., D. Weisenstein, H. Mack, E. Rozanov, T. Peter, and S. Brönnimann, Volcanic forcing for climate modeling: a new microphysics-based data set covering years 1600–present, ***Clim. Past***, ***10*** (1), 359–375, doi:10.5194/cp-10-359-2014, 2014.

Bala, G., P.B. Duffy, and K.E. Taylor, Impact of geoengineering schemes on the global hydrological cycle, ***Proc. Natl. Acad. Sci.***, ***105*** (22), 7664–7669, doi:10.1073/pnas.0711648105, 2008.

Bamber, J.L., M. Oppenheimer, R.E. Kopp, W.P. Aspinall, and R.M. Cooke, Ice sheet contributions to future sea-level rise from structured expert judgment, ***Proc. Natl. Acad. Sci., 116*** (23), 11195, doi:10.1073/pnas.1817205116, 2019.

Banerjee, A., A.H. Butler, L.M. Polvani, A. Robock, I.R. Simpson, and L. Sun, Robust winter warming over Eurasia under stratospheric sulfate geoengineering–the role of stratospheric dynamics, ***Atmos. Chem. Phys.***, ***21*** (9), 6985–6997, doi:10.5194/acp-21-6985-2021, 2021.

Barnes, J.E., and D.J. Hofmann, Lidar measurements of stratospheric aerosol over Mauna Loa Observatory, ***Geophys. Res. Lett.***, ***24*** (15), 1923–1926, doi:10.1029/97GL01943, 1997.

Bauman, J.J., P.B. Russell, M.A. Geller, and P. Hamill, A stratospheric aerosol climatology from SAGE II and CLAES measurements: 2. Results and comparisons, 1984–1999, ***J. Geophys. Res. Atmos.***, ***108*** (D13), doi:10.1029/2002JD002993, 2003.

Bekki, S., J.A. Pyle, W. Zhong, R. Toumi, J.D. Haigh, and D.M. Pyle, The role of microphysical and chemical processes in prolonging the climate forcing of the Toba eruption, ***Geophys. Res. Lett.***, ***23*** (19), 2669–2672, doi:10.1029/96GL02088, 1996.

Benduhn, F., J. Schallock, and M.G. Lawrence, Early growth dynamical implications for the steerability of stratospheric solar radiation management via sulfur aerosol particles, ***Geophys. Res. Lett.***, ***43***, 9956–9963, doi:10.1002/2016GL070701, 2016.

Berthet, G., F. Jégou, V. Catoire, G. Krysztofiak, J.B. Renard, A.E. Bourassa, D.A. Degenstein, C. Brogniez, M. Dorf, S. Kreycy, and K. Pfeilsticker, Impact of a moderate volcanic eruption on chemistry in the lower stratosphere: balloon-borne observations and model calculations. ***Atmos Chem and Phys***, ***17***(3), pp.2229-2253, 2017.

Bhowmick, M., S.K. Mishra, B. Kravitz, S. Sahany, and P. Salunke, Response of the Indian summer monsoon to global warming, solar geoengineering and its termination, ***Sci. Rep., 11*** (1), 9791, doi:10.1038/s41598-021-89249-6, 2021.

Bittner, M., H. Schmidt, C. Timmreck, and F. Sienz, Using a large ensemble of simulations to assess the Northern Hemisphere stratospheric dynamical response to tropical volcanic eruptions and its uncertainty, ***Geophys. Res. Lett.***, ***43*** (17), 9324–9332, doi:10.1002/2016GL070587, 2016.

Bourassa, A.E., L.A. Rieger, N.D. Lloyd, and D.A. Degenstein, Odin-OSIRIS stratospheric aerosol data product and SAGE III intercomparison, ***Atmos. Chem. Phys.***, ***12*** (1), 605–614, doi:10.5194/acp-12-605-2012, 2012.

Brenna, H., S. Kutterolf, M.J. Mills, U. Niemeier, C. Timmreck, and K. Krüger, Decadal disruption of the QBO by tropical volcanic supereruptions, ***Geophys. Res. Lett.***, ***48*** (5), e2020GL089687, doi:10.1029/2020GL089687, 2021.

Budyko, M.I., Izmeniya Klimata. Gidrometeoizdat, also published as: Budyko, M.I. 1977 Climatic changes (transl. Izmeniia Klimata Leningrad: Gidrometeoizdat, 1974), ***American Geophysical Union***, Washington, DC, 1974.

Butchart, N., The Brewer-Dobson circulation, ***Rev. Geophys.***, ***52*** (2),157–184, doi:10.1002/2013RG000448, 2014.

Butler, A.H., J.S. Daniel, R.W. Portmann, A.R. Ravishankara, P.J. Young, D.W. Fahey, and K.H. Rosenlof, Diverse policy implications for future ozone and surface UV in a changing climate, ***Environ. Res. Lett.***, ***11*** (6), 064017, doi:10.1088/1748-9326/11/6/064017, 2016.

Caldeira, K., and L. Wood, Global and Arctic climate engineering: numerical model studies, ***Philos. Trans. Royal Soc. A: Math. Phys. Eng. Sci.***, ***366*** (1882), 4039–4056, doi:10.1098/rsta.2008.0132, 2008.

Canadell, J.G., P.M.S. Monteiro, M.H. Costa, L. Cotrim da Cunha, P.M. Cox, A.V. Eliseev, S., Henson, M. Ishii, S. Jaccard, C. Koven, A. Lohila, P.K. Patra, S. Piao, J. Rogelj, S. Syampungani, S. Zaehle, and K. Zickfeld, Global Carbon and other Biogeochemical Cycles and Feedbacks, Chapter 5, in ***Climate Change 2021: The Physical Science Basis. Contribution of Working Group I to the Sixth Assessment Report of the Intergovernmental Panel on Climate Change***, edited by V. Masson-Delmotte, P. Zhai, A. Pirani, S. L. Connors, C. Péan, S. Berger, N. Caud, Y. Chen, L. Goldfarb, M. I. Gomis, M. Huang, K. Leitzell, E. Lonnoy, J.B.R. Matthews, T. K. Maycock, T. Waterfield, O. Yelekçi, R. Yu and B. Zhou, 144 pp., Cambridge University Press, Cambridge, United Kingdom, doi:10.1017/9781009157896.007, 2021.

Cao, L., L. Duan, G. Bala, and K. Caldeira, Simulated climate and terrestrial biosphere response to three radiation geoengineering schemes, in ***AGU Fall Meeting Abstracts***, Vol. 2018, GC31H-1351 pp., 2018.

Carn, S.A., L. Clarisse, and A.J. Prata, A.J., Multi-decadal satellite measurements of global volcanic degassing. ***Journal of Volcanology and Geothermal Research***, ***311***, pp.99-134, 2016.

Carn, S.A., V.E. Fioletov, C.A. McLinden, C. Li, and N.A. Krotkov, A decade of global volcanic SO2 emissions measured from space. ***Scientific reports***, ***7***(1), pp.1-12, 2017.

Chazette, P., C. David, J. Lefrère, S. Godin, J. Pelon, and G. Mégie, Comparative lidar study of the optical, geometrical, and dynamical properties of stratospheric post-volcanic aerosols, following the eruptions of El Chichon and Mount Pinatubo, ***J. Geophys. Res. Atmos.***, ***100*** (D11), 23,195–23,207, doi:10.1029/95JD02268, 1995.

Christian, K., J. Wang, C. Ge, D. Peterson, E. Hyer, J. Yorks, and M. McGill, Radiative forcing and stratospheric warming of pyrocumulonimbus smoke aerosols: First modeling results with multisensor (EPIC, CALIPSO, and CATS) views from space, ***Geophys. Res. Lett.***, ***46*** (16), 10,061–10,071, doi:10.1029/2019GL082360, 2019.

Christidis, N., G.S. Jones, and P.A. Stott, Dramatically increasing chance of extremely hot summers since the 2003 European heatwave, ***Nat. Clim. Change***, ***5*** (1), 46–50, doi:10.1038/nclimate2468, 2015.

Clarisse, L., D. Hurtmans, C. Clerbaux, J. Hadji-Lazaro, Y. Ngadi, and P.-F. Coheur, Retrieval of sulphur dioxide from the infrared atmospheric sounding interferometer (IASI), ***Atmos. Meas. Tech.***, ***5*** (3), 581–594, doi:10.5194/amt-5-581-2012, 2012.

Clyne M, Lamarque JF, Mills MJ, Khodri M, Ball W, Bekki S, Dhomse SS, Lebas N, Mann G, Marshall L, Niemeier U. Model physics and chemistry causing intermodel disagreement within the VolMIP-Tambora Interactive Stratospheric Aerosol ensemble. Atmos. Chem. Phys., 21, 3317–3343, https://doi.org/10.5194/acp-21-3317-2021, 2021.

Crutzen, P.J., Upper limits on atmospheric ozone reductions following increased application of fixed nitrogen to the soil, ***Geophys. Res. Lett.***, ***3*** (3), 169–172, doi:10.1029/GL003i003p00169, 1976.

Crutzen, P.J., Albedo enhancement by stratospheric sulfur injections: a contribution to resolve a policy dilemma?, ***Clim. Change***, ***77*** (3-4), 211, doi:10.1007/s10584-006-9101-y, 2006.

Curry, C.L., J. Sillmann, D. Bronaugh, K. Alterskjær, J.N.S. Cole, B. Kravitz., J.E. Kristjánsson, H. Muri, U. Niemeier, A. Robock, and S. Tilmes, A multi-model examination of climate extremes in an idealized geoengineering experiment, ***J. Geophys. Res. Atmos.***, ***119*** (7), 3900–3923, doi:10.1002/2013JD020648, 2014.

Cziczo, D.J., M.J. Wolf, B. Gasparini, S. Münch, and U. Lohmann, Unanticipated side effects of stratospheric albedo modification proposals due to aerosol composition and phase, ***Sci. Rep.***, ***9*** (1), 1–7, doi:10.1038/s41598-019-53595-3, 2019.

Dai, Z., D.K. Weisenstein, F.N. Keutsch, and D.W. Keith, Experimental reaction rates constrain estimates of ozone response to calcium carbonate geoengineering, ***Commun. Earth. Environ.***, ***1*** (1), 1–9, doi:10.1038/s43247-020-00058-7, 2020.

Danilin, M.Y., J.M. Rodriguez, W. Hu, M.K. Ko, D.K. Weisenstein, J.B. Kumer, J.L. Mergenthaler, J.M. Russell III, M. Koike, G.K. Yue, and N.B. Jones, Nitrogen species in the post-Pinatubo stratosphere: Model analysis utilizing UARS measurements, ***J. Geophys. Res. Atmos.***, ***104*** (D7), 8247–8262, doi:10.1029/1999JD900024, 1999.

Damany-Pearce, L., B.T. Johnson, A.F. Wells, M.J. Osborne, J. Allan, C. Belcher, J.M. Haywood, Australian wildfires cause the largest stratospheric warming since Pinatubo and extends the lifetime of the Antarctic ozone hole, Scientific Reports, DOI: 10.1038/s41598-022-15794-3, 2022.

Das, S., P.R. Colarco, L.D. Oman, G. Taha, and O. Torres, The long-term transport and radiative impacts of the 2017 British Columbia pyrocumulonimbus smoke aerosols in the stratosphere, ***Atmos. Chem. Phys.***, ***21***, 12,069–12,090, doi:10.5194/acp-21-12069-2021, 2021.

Davidson, P., C. Burgoyne, H. Hunt, and M. Causier, Lifting options for stratospheric aerosol geoengineering: advantages of tethered balloon systems, ***Philos. Trans. Royal Soc. A: Math. Phys. Eng. Sci.***, ***370*** (1974), 4263–4300, doi:10.1098/rsta.2011.0639, 2012.

de Leeuw, J., A. Schmidt, C.S. Witham, N. Theys, I.A. Taylor, R.G. Grainger, R.J. Pope, J. Haywood, M. Osborne, and N.I. Kristiansen, The 2019 Raikoke volcanic eruption: Part 1 Dispersion model simulations and satellite retrievals of volcanic sulfur dioxide, ***Atmos. Chem. Phys.***, ***21*** (14), 10,851–10,879, doi:10.5194/acp-2020-889, 2021.

Deshler, T., M.E. Hervig, D.J. Hofmann, J.M. Rosen, and J.B. Liley, Thirty years of in situ stratospheric aerosol size distribution measurements from Laramie, Wyoming (41 N), using balloon-borne instruments, ***J. Geophys. Res. Atmos.***, ***108*** (D5), doi:10.1029/2002JD002514, 2003.

Deshler, T., B. Luo, M. Kovilakam, T. Peter, and L.E. Kalnajs, Retrieval of aerosol size distributions from in situ particle counter measurements: Instrument counting efficiency and comparisons with satellite measurements, ***J. Geophys. Res. Atmos.***, ***124*** (9), 5058–5087, doi:1029/2018JD029558, 2019.

Dhomse, S.S., K.M. Emmerson, G.W. Mann, N. Bellouin, K.S. Carslaw, M.P. Chipperfield, R. Hommel, N.L. Abraham, P. Telford, P. Braesicke, M. Dalvi, C.E. Johnson, F. O'Connor, O. Morgenstern, J.A. Pyle, T. Deshler, J.M. Zawodny, and L.W. Thomason., Aerosol microphysics simulations of the Mt. Pinatubo eruption with the UM-UKCA composition-climate model, ***Atmos. Chem. Phys.***, ***14*** (20), 11,221–11,246, doi:10.5194/acp-14-11221-2014, 2014.

Doiron, S.D., G.J. Bluth, C.C. Schnetzler, A.J. Krueger, and L.S. Walter, Transport of Cerro Hudson SO_2 clouds, ***Eos***, ***72*** (45), 489–498, doi:10.1029/90EO00354, 1991.

Drdla, K., and R. Müller, Temperature thresholds for chlorine activation and ozone loss in the polar stratosphere, ***Ann. Geophys.***, ***30*** (7), 1055–1073, doi:10.5194/angeo-30-1055-2012, 2012.

Driscoll, S., A. Bozzo, L.J. Gray, A. Robock, and G. Stenchikov, Coupled Model Intercomparison Project 5 (CMIP5) simulations of climate following volcanic eruptions, ***J. Geophys. Res. Atmos.***, ***117*** (D17), doi:10.1029/2012JD017607, 2012.

Duan, L., L. Cao, G. Bala, and K. Caldeira, Climate response to pulse versus sustained stratospheric aerosol forcing, ***Geophys. Res. Lett.***, ***46***, 8976–8984, doi:10.1029/2019GL083701, 2019.

Dykema, J.D., D.W. Keith, and F.N. Keutch, Improved aerosol radiative properties as a foundation for solar geoengineering risk assessment, ***Geophys. Res. Lett.***, ***43***, 7758–7766, doi:10.1002/2016GL069258, 2016.

Eastham, S.D., D.K. Weisenstein, D.W. Keith, and S.R. Barrett, Quantifying the impact of sulfate geoengineering on mortality from air quality and UV-B exposure, ***Atmos. Environ.***, ***187***, 424–434, doi:10.1016/j.atmosenv.2018.05.047, 2018.

Eastham, S., S. Doherty, D. Keith, J.H. Richter, and L. Xia, Improving models for solar climate intervention research, ***Eos***, ***102***, doi:10.1029/2021EO156087, 2021.

English, J.M., O.B. Toon, and M.J. Mills, Microphysical simulations of sulfur burdens from stratospheric sulfur geoengineering, ***Atmos. Chem. Phys.***, ***12*** (10), 4775–4793, doi:10.5194/acp-12-4775-2012, 2012.

English, J.M., O.B. Toon, and M.J. Mills, Microphysical simulations of large volcanic eruptions: Pinatubo and Toba, ***J. Geophys. Res. Atmos.***, ***118*** (4), 1880–1895, doi:10.1002/jgrd.50196, 2013.

Evan, A.T., Atlantic hurricane activity following two major volcanic eruptions. ***Journal of Geophysical Research: Atmospheres***, ***117***(D6), 2012.

Fahey, D.H., S.R. Kawa, E.L. Woodbridge, P. Tin, J.C. Wilson, H.H. Jonsson, J.E. Dye, D. Baumgardner, S. Borrmann, D.W. Toohey, L.M. Avallone, M.H. Proffitt, J. Margitan, M. Loewenstein, J.R. Podolske, R.J. Salawitch, S.C. Wofsy, M.K.W. Ko, D.E. Anderson, M.R. Schoeber, and K.R. Chan, ***In situ*** measurements constraining the role of sulphate aerosols in mid-latitude ozone depletion, ***Nature***, ***363*** (6429), 509–514, doi:10.1038/363509a0, 1993.

Fan, Y., J. Tjiputra, H. Muri, D. Lombardozzi, C.E. Park, S. Wu, and D. Keith, Solar geoengineering can alleviate climate change pressures on crop yields, ***Nat. Food***, ***2*** (5), 373–381, doi:10.1038/s43016-021-00278-w, 2021.

Fasullo, J.T., S. Tilmes, J.H. Richter, B. Kravitz, D.G. MacMartin, M.J. Mills, and I.R. Simpson, Persistent polar ocean warming in a strategically geoengineered climate, ***Nature Geosci.***, ***11*** (12), 910–914, doi:10.1038/s41561-018-0249-7, 2018.

Ferraro, A.J., E.J. Highwood, and A.J. Charlton-Perez, Stratospheric heating by potential geoengineering aerosols, ***Geophys. Res. Lett.***, ***38*** (24), doi:10.1029/2011GL049761, 2011.

Ferraro, A. J., E.J. Highwood, and A. J. Charlton-Perez, Correction to "Stratospheric heating by potential geoengineering aerosols," Geophys. Res. Lett.,39, L10808, doi:10.1029/2012GL052175, 2012.

Ferraro, A.J., E.J. Highwood, and A.J. Charlton-Perez, Weakened tropical circulation and reduced precipitation in response to geoengineering, ***Environ. Res. Lett.***, ***9*** (1), 014001, doi:10.1088/1748-9326/9/1/014001, 2014.

Ferraro, A.J., A.J. Charlton-Perez, and E.J. Highwood, Stratospheric dynamics and midlatitude jets under geoengineering with space mirrors and sulfate and titania aerosols, ***J. Geophys. Res. Atmos.***, ***120*** (2), 414–429, doi:10.1002/2014JD022734, 2015.

Franke, H., U. Niemeier, and D. Visioni, Differences in the QBO response to stratospheric aerosol modification depending on injection strategy and species, ***Atmos. Chem. Phys.***, ***21*** (11), 8615–8635, doi:10.5194/acp-21-8615-2021, 2021.

Frith, S.M., R.S. Stolarski, N.A. Kramarova, and R.D. McPeters, Estimating uncertainties in the SBUV Version 8.6 merged profile ozone data set, ***Atmos. Chem. Phys.***, ***17*** (23), 14,695–14,707, doi:10.5194/acp-17-14695-2017, 2017.

Fromm, M.D., D.T. Lindsey, R. Servranckx, G. Yue, T. Trickl, R. Sica, P. Doucet, and S. Godin-Beekmann, The untold story of pyrocumulonimbus, ***Bull. Amer. Meteor. Soc.***, ***91*** (9), 1193–1210, doi:10.1175/2010BAMS3004.1, 2010.

Fuss, S., J.G. Canadell, P. Ciais, R.B. Jackson, C.D. Jones, A. Lyngfelt, G.P. Peters, and D.P. Van Vuuren, Moving toward net-zero emissions requires new alliances for carbon dioxide removal, ***One Earth***, ***3*** (2), 145–149, doi:10.1016/j.oneear.2020.08.002, 2020.

Fyfe, J.C., J.N.S. Cole, V.K. Arora, and J.F. Scinocca, Biogeochemical carbon coupling influences global precipitation in geoengineering experiments, ***Geophys. Res. Lett.***, ***40*** (3), 651–655, doi:10.1002/grl.50166, 2013.

Gao, R.S., K.H. Rosenlof, B. Kärcher, S. Tilmes, O.B. Toon, C. Maloney, and P. Yu, Toward practical stratospheric aerosol albedo modification: Solar-powered lofting, ***Sci. Adv.***, ***7*** (20), doi:10.1126/sciadv.abe3416, 2021.

Gertler, C.G., P.A. O'Gorman, B. Kravitz, J.C. Moore, S.J. Phipps, and S. Watanabe, Weakening of the extratropical storm tracks in solar geoengineering scenarios, ***Geophys. Res. Lett.***, ***47*** (11), e2020GL087348, doi:10.1029/2020GL087348, 2020.

Glienke, S., P.J. Irvine, and M.G. Lawrence, The impact of geoengineering on vegetation in experiment G1 of the GeoMIP, ***J. Geophys. Res. Atmos.***, ***120*** (19), 10,196–10,213, doi:10.1002/2015JD024202, 2015.

Govindasamy, B., and K. Caldeira, Geoengineering Earth's radiation balance to mitigate CO2-induced climate change, ***Geophys. Res. Lett.***, ***27*** (14), 2141–2144, doi:10.1029/1999GL006086, 2000.

Grant, W.B., J. Fishman, E.V. Browell, V.G. Brackett, D. Nganga, A. Minga, B. Cros, R.E. Veiga, C.F. Butler, M.A. Fenn, and G.D. Nowicki, Observations of reduced ozone concentrations in the tropical stratosphere after the eruption of Mount Pinatubo, ***Geophys. Res. Lett.***, ***19*** (11), 1109–1112, doi:10.1029/92GL01153, 1992.

Gregory, J.M., and T. Andrews, Variation in climate sensitivity and feedback parameters during the historical period, ***Geophys. Res. Lett.***, ***43*** (8), 3911–3920, doi:10.1002/2016GL068406, 2016.

Hamilton, C., ***Earthmasters: the dawn of the age of climate engineering***, Yale University Press, 2013.

Hansen, J., A. Lacis, R. Ruedy, and M. Sato, Potential climate impact of Mount Pinatubo eruption, ***Geophys. Res. Lett.***, ***19*** (2), 215–218, doi:10.1029/91GL02788, 1992.

Hansen, J., M. Sato, L. Nazarenko, R. Ruedy, A. Lacis, D. Koch, I. Tegen, T. Hall, D. Shindell, B. Santer, and P.Stone, Climate forcings in Goddard Institute for space studies SI2000 simulations. ***Journal of Geophysical Research: Atmospheres***, *107*(D18), pp.ACL-2, 2002.

Hawcroft, M., J.M. Haywood, M. Collins, A. Jones, A.C. Jones, and G. Stephens, Southern Ocean albedo, inter-hemispheric energy transports and the double ITCZ: Global impacts of biases in a coupled model, ***Clim Dyn.***, *48* (7), 2279–2295, doi:10.1007/s00382-016-3205-5, 2017.

Haywood, J.M., A. Jones, L. Clarisse, A. Bourassa, J. Barnes, P. Telford, N. Bellouin, O. Boucher, P. Agnew, C. Clerbaux, and P. Coheur, Observations of the eruption of the Sarychev volcano and simulations using the HadGEM2 climate model, ***J. Geophys. Res. Atmos.***, *115* (D21), doi:10.1029/2010JD014447, 2010.

Haywood, J.M., A. Jones, N. Bellouin, and D. Stephenson, Asymmetric forcing from stratospheric aerosols impacts Sahelian rainfall, ***Nat. Clim. Change***, *3* (7), 660–665, doi:10.1038/nclimate1857, 2013.

Haywood, J.M., A. Jones, and G.S. Jones, The impact of volcanic eruptions in the period 2000–2013 on global mean temperature trends evaluated in the HadGEM2-ES climate model, ***Atmos. Sci. Lett.***, *15* (2), 92–96, doi:10.1002/asl2.471, 2014.

Haywood, J.M., A. Jones, B. Johnson, and W.M. Smith, Assessing the consequences of including aerosol absorption in potential stratospheric aerosol injection climate intervention strategies, ***Atmos. Chem. Phys.***, *22* (9), 6135–6150, doi:10.5194/acp-22-6135-2022, 2022.

Heckendorn, P., D. Weisenstein, S. Fueglistaler, B.P. Luo, E. Rozanov, M. Schraner, L.W. Thomason, and T. Peter, The impact of geoengineering aerosols on stratospheric temperature and ozone, ***Environ. Res. Lett.***, *4* (4), 045108, doi:10.1088/1748-9326/4/4/045108, 2009.

Hendricks, J., E. Lippert, H. Petry, and A. Ebel, Heterogeneous reactions on and in sulfate aerosols: Implications for the chemistry of the midlatitude tropopause region, ***J. Geophys. Res. Atmos.***, *104* (D5), 5531–5550, doi:10.1029/1998JD100098, 1999.

Henry, M., and T.M. Merlis, Forcing dependence of atmospheric lapse rate changes dominates residual polar warming in solar radiation management climate scenarios, ***Geophys. Res. Lett.***, *47* (15), e2020GL087929, doi:10.1029/2020GL087929, 2020.

Hirsch, E., and I. Koren, Record-breaking aerosol levels explained by smoke injection into the stratosphere, ***Science***, *371*, 1269–1274, doi:10.1126/science.abe1415, 2021.

Hofmann, D.J., and S. Solomon, Ozone destruction through heterogeneous chemistry following the eruption of El Chichon, ***J. Geophys. Res. Atmos.***, *94* (D4), 5029–5041, doi:10.1029/JD094iD04p05029, 1989.

Huang, Y., Y. Wang, and H. Huang, Stratospheric water vapor feedback disclosed by a locking experiment, ***Geophys. Res. Lett.***, *47* (12), e2020GL087987, doi:10.1029/2020GL087987, 2020.

Huneeus, N., O. Boucher, K. Alterskjaer, J.N. Cole, C.L. Curry, D. Ji, A. Jones, B. Kravitz, J.E. Kristjánsson, J.C. Moore, and H. Muri, Forcings and feedbacks in the GeoMIP ensemble for a reduction in solar irradiance and increase in CO2, ***J. Geophys. Res. Atmos.***, *119* (9), 5226–5239, doi:10.1002/2013JD021110, 2014.

Huynh, H.N., and V.F. McNeill, Heterogeneous reactivity of HCl on CaCO3 aerosols at stratospheric temperature, ***ACS Earth Space Chem.***, *5* (8), 1896–1901, doi:10.1021/acsearthspacechem.1c00151, 2021.

Hwang, Y.T., and D.M. Frierson, Link between the double-Intertropical Convergence Zone problem and cloud biases over the Southern Ocean, ***Proc. Natl. Acad. Sci.***, *110* (13), 4935–4940, doi:10.1073/pnas.1213302110, 2013.

Iles, C.E., G.C. Hegerl, A.P. Schurer, and X. Zhang, The effect of volcanic eruptions on global precipitation. ***Journal of Geophysical Research: Atmospheres***, *118*(16), pp.8770-8786, 2013.

IPCC (Intergovenmental Panel on Climate Change), ***Global warming of 1.5°C. An IPCC Special Report on the impacts of global warming of 1.5°C above preindustrial levels and related global greenhouse gas emission pathways, in the context of strengthening the global response to the threat of climate change, sustainable development, and efforts to eradicate poverty***, edited by V. Masson-Delmotte, P. Zhai, H. O. Pörtner, D. Roberts, J. Skea, P.R. Shukla, A. Pirani, W. Moufouma-Okia, C. Péan, R. Pidcock, S. Connors, J. B. R. Matthews, Y. Chen, X. Zhou, M. I. Gomis, E. Lonnoy, T. Maycock, M. Tignor, and T. Waterfield, 630 pp., Cambridge University Press, Cambridge, United Kingdom, 2018.

IPCC (Intergovenmental Panel on Climate Change), ***Climate Change 2021: The Physical Science Basis. Contribution of Working Group I to the Sixth Assessment Report of the Intergovernmental Panel on Climate Change***, edited by V. Masson-Delmotte, P. Zhai, A. Pirani, S.L. Connors, C. Péan, S. Berger, N. Caud, Y. Chen, L. Goldfarb, M.I. Gomis, M. Huang, K. Leitzell, E. Lonnoy, J.B.R. Matthews, T.K. Maycock, T. Waterfield, O. Yelekçi, R. Yu, and B. Zhou, Cambridge University Press, Cambridge, United Kingdom, 2021.

IPCC (Intergovenmental Panel on Climate Change), ***Climate Change 2022: Mitigation of Climate Change. Contribution of Working Group III to the Sixth Assessment Report of the Intergovernmental Panel on Climate Change***, edited by P.R. Shukla, J. Skea, R. Slade, A. Al Khourdajie, R. van Diemen, D. McCollum, M. Pathak, S. Some, P. Vyas, R. Fradera, M. Belkacemi, A. Hasija, G. Lisboa, S. Luz, J. Malley, Cambridge University Press, Cambridge, United Kingdom and New York, NY, USA, doi:10.1017/9781009157926, 2022.

Irvine, P.J., B. Kravitz, M.G. Lawrence, D. Gerten, C. Caminade, S.N. Gosling, E.J. Hendy, B.T. Kassie, W.D. Kissling, H. Muri, A. Oschlies, and S.J. Smith, Towards a comprehensive climate impacts assessment of solar geoengineering, ***Earth's Future***, *5* (1), 93–106, doi:10.1002/2016EF000389, 2017.

Irvine, P.J., D.W. Keith, and J. Moore, Brief communication: Understanding solar geoengineering's potential to limit sea level rise requires attention from cryosphere experts, ***The Cryosphere***, *12* (7), 2501–2513, doi:10.5194/tc-12-2501-2018, 2018.

Irvine, P., K. Emanuel, J. He, L.W. Horowitz, G. Vecchi, and D. Keith, Halving warming with idealized solar geoengineering moderates key climate hazards, ***Nat. Clim. Change***, *9* (4), 295–299, doi:10.1038/s41558-019-0398-8, 2019.

Irvine, P.J., and D.W. Keith, Halving warming with stratospheric aerosol geoengineering moderates policy-relevant climate hazards, ***Environ. Res. Lett.***, *15* (4), 044011, doi:10.1088/1748-9326/ab76de, 2020.

Ji, D., S. Fang, C.L. Curry, H. Kashimura, S. Watanabe, J.N. Cole, A. Lenton, H. Muri, B. Kravitz, and J.C. Moore, Extreme temperature and precipitation response to solar dimming and stratospheric aerosol geoengineering, ***Atmos. Chem. Phys.***, *18* (14), 10,133–10,156, doi:10.5194/acp-18-10133-2018, 2018.

Jiang, J., L. Cao, D.G. MacMartin, I.R. Simpson, B. Kravitz, W. Cheng, D. Visioni, S. Tilmes, J.H. Richter, and M.J. Mills, Stratospheric sulfate aerosol geoengineering could alter the high-latitude seasonal cycle, ***Geophys. Res. Lett.***, *46* (23), 14,153–14,163, doi:10.1029/2019GL085758, 2019.

Johnston, P.V., R.L. McKenzie, J.G. Keys, and W.A. Matthews, Observations of depleted stratospheric NO2 following the Pinatubo volcanic eruption. ***Geophysical research letters***, *19*(2), pp.211-213, 1992.

Jones, A., J.M. Haywood, O. Boucher, B. Kravitz, and A. Robock, Geoengineering by stratospheric SO2 injection: results from the Met Office HadGEM2 climate model and comparison with the Goddard Institute for Space Studies ModelE, ***Atmos. Chem. Phys.***, *10* (13), 5999–6006, doi:10.5194/acp-10-5999-201010, 74217434, 2010.

Jones, A., J.M. Haywood, and O. Boucher, A comparison of the climate impacts of geoengineering by stratospheric SO2 injection and by brightening of marine stratocumulus cloud, ***Atmos. Sci. Lett.***, *12* (2), 176–183, doi:10.1002/asl.291, 2011.

Jones, A., J.M. Haywood, K. Alterskjær, O. Boucher, J.N.S. Cole, C.L. Curry, P.J. Irvine, D. Ji, B. Kravitz, J.E. Kristjánsson, J.C. Moore, U. Niemeier, A. Robock, H. Schmidt, B. Singh, S. Tilmes, S. Watanabe, and J.-H. Yoon, The impact of abrupt suspension of solar radiation management (termination effect) in experiment G2 of the Geoengineering Model Intercomparison Project (GeoMIP), ***J. Geophys. Res. Atmos.***, *118* (17), 9743–9752, doi:10.1002/jgrd.50762, 2013.

Jones, A.C., J.M. Haywood, and A. Jones, Climatic impacts of stratospheric geoengineering with sulfate, black carbon and titania injection, ***Atmos. Chem. Phys.***, *16* (5), 2843–2862, doi:10.5194/acp-16-2843-2016, 2016a.

Jones, A.C., J.M. Haywood, A. Jones, and V. Aquila, Sensitivity of volcanic aerosol dispersion to meteorological conditions: A Pinatubo case study, ***J. Geophys. Res. Atmos.***, *121* (12), 6892–6908, doi:10.1002/2016JD025001, 2016b.

Jones, A.C., J.M. Haywood, N. Dunstone, K. Emanuel, M.K. Hawcroft, K.I. Hodges, and A. Jones, Impacts of hemispheric solar geoengineering on tropical cyclone frequency, ***Nat. Commun.***, *8* (1), 1–10, doi:10.1038/s41467-017-01606-0, 2017.

Jones, A.C., M.K. Hawcroft, J.M. Haywood, A. Jones, X. Guo, and J.C. Moore, Regional climate impacts of stabilizing global warming at 1.5 K using solar geoengineering, ***Earth's Future***, *6* (2), 230–251, doi:10.1002/2017EF000720, 2018.

Jones, A., J.M. Haywood, A.C. Jones, S. Tilmes, B. Kravitz, and A. Robock, North Atlantic Oscillation response in GeoMIP experiments G6solar and G6sulfur: why detailed modelling is needed for understanding regional implications of solar radiation management, ***Atmos. Chem. Phys.***, *21* (2), 1287–1304, doi:10.5194/acp-21-1287-2021, 2021.

Jones, A., J.M. Haywood, A.A. Scaife, O. Boucher, M. Henry, B. Kravitz, P. Nabat, U. Niemeier, R. Séférian, and D. Visioni, The impact of stratospheric aerosol intervention on the North Atlantic and Quasi-Biennial Oscillations in the Geoengineering Model Intercomparison Project (GeoMIP) G6sulfur experiment, ***Atmos Chem Phys***, https://doi.org/10.5194/acp-22-2999-2022, 2022.

Kablick, G.P., D.R. Allen, M.D. Fromm, and G.E. Nedoluha, Australian pyroCb smoke generates synoptic-scale stratospheric anticyclones, ***Geophys. Res. Lett.***, 47, e2020GL088101, doi:10.1029/2020GL088101, 2020.

Kalidindi S., G. Bala, A. Modak, and K. Caldeira, Modeling of solar radiation management: a comparison of simulations using reduced solar constant and stratospheric sulphate aerosols, ***Clim. Dyn.***, ***44*** (9), 2909–2925, doi:10.1007/s00382-014-2240-3, 2015.

Karagulian, F., L. Clarisse, C. Clerbaux, A.J. Prata, D. Hurtmans, and P.F. Coheur, Detection of volcanic SO2, ash, and H2SO4 using the Infrared Atmospheric Sounding Interferometer (IASI), ***J. Geophys. Res. Atmos.***, ***115*** (D2), doi:10.1029/2009JD012786, 2010.

Keeble, J., B. Hassler, A. Banerjee, R. Checa-Garcia, G. Chiodo, S. Davis, V. Eyring, P.T. Griffiths, O. Morgenstern, P. Nowack, G. Zeng, J. Zhang, G. Bodeker, S. Burrows, P. Cameron-Smith, D. Cugnet, C. Danek, M. Deushi, L.W. Horowitz, A. Kubin, L. Li, G. Lohmann, M. Michou, M.J. Mills, P. Nabat, D. Olivié, S. Park, Ø. Seland, J. Stoll, K.-H. Wieners, and T. Wu, Evaluating stratospheric ozone and water vapour changes in CMIP6 models from 1850 to 2100, ***Atmos. Chem. Phys.***, ***21*** (6), 5015–5061, doi:10.5194/acp-21-5015-2021, 2021.

Keith, D., ***A case for climate engineering***, MIT Press, 224 pp., 2013.

Keith, D.W., Photophoretic levitation of engineered aerosols for geoengineering, ***Proc. Natl. Acad. Sci.***, ***107*** (38), 16,428–16,431, doi:10.1073/pnas.1009519107, 2010.

Keith, D.W., D.K. Weisenstein, J.A. Dykema, and F.N. Keutsch, Stratospheric solar geoengineering without ozone loss, ***Proc. Natl. Acad. Sci.***, ***113*** (52), 14,910–14,914, doi:10.1073/pnas.1615572113, 2016.

Keller, D.P., A. Lenton, V. Scott, N.E. Vaughan, N. Bauer, D. Ji, C.D. Jones, B. Kravitz, H. Muri, and K. Zickfeld, The carbon dioxide removal model intercomparison project (CDRMIP): rationale and experimental protocol for CMIP6, ***Geosci. Model Dev.***, ***11*** (3), 1133–1160, doi:10.5194/gmd-11-1133-2018, 2018.

Khaykin, S.M., S. Godin-Beekmann, A. Hauchecorne, J. Pelon, F. Ravetta, and P. Keckhut, Stratospheric smoke with unprecedentedly high backscatter observed by lidars above southern France, ***Geophys. Res. Lett***, 45, 1639–1646, doi:10.1002/2017GL076763, 2018.

Khaykin, S., B. Legras, S. Bucci, P. Sellitto, L. Isaksen, F. Tencé, S. Bekki, A. Bourassa, L. Rieger, D. Zawada, J. Jumelet, and S. Godin-Beekmann, The 2019/20 Australian wildfires generated a persistent smoke-charged vortex rising up to 35 km altitude, ***Commun. Earth Environ.***, ***1*** (1), 22, doi:10.1038/s43247-020-00022-5, 2020.

Kinne, S., O.B. Toon, and M.J. Prather, Buffering of stratospheric circulation by changing amounts of tropical ozone a Pinatubo Case Study, ***Geophys. Res. Lett.***, ***19*** (19), 1927–1930, doi:10.1029/92GL01937, 1992.

Kleinschmitt, C., O. Boucher, S. Bekki, F. Lott, and U. Platt, The Sectional Stratospheric Sulfate Aerosol module (S3A-v1) within the LMDZ general circulation model: description and evaluation against stratospheric aerosol observations, ***Geosci. Model Dev.***, ***10*** (9), 3359–3378, doi:10.5194/gmd-10-3359-2017, 2017.

Kleinschmitt, C., O. Boucher, and U. Platt, Sensitivity of the radiative forcing by stratospheric sulfur geoengineering to the amount and strategy of the SO2 injection studied with the LMDZ-S3A model, ***Atmos. Chem. Phys.***, ***18*** (4), 2769-2786, doi:10.5194/acp-18-2769-2018, 2018.

Kloss, C., G. Berthet, P. Sellitto, F. Ploeger, G. Taha, M. Tidiga, M. Eremenko, A. Bossolasco, F. Jégou, J.-B. Renard, and B. Legras, Stratospheric aerosol layer perturbation caused by the 2019 Raikoke and Ulawun eruptions and their radiative forcing, ***Atmos. Chem. Phys.***, ***21*** (1), 535–560, doi:10.5194/acp-21-535-2021, 2021.

Koike, M., N.B. Jones, W.A. Matthews, P.V. Johnston, R.L. McKenzie, D. Kinnison, and J. Rodriguez, Impact of Pinatubo aerosols on the partitioning between NO2 and HNO3, ***Geophys. Res. Lett.***, ***21*** (7), 597–600, doi:10.1029/94GL00303, 1994.

Kokkola H., R. Hommel, J. Kazil, U. Niemeier, A.-I. Partanen, J. Feichter, and C. Timmreck, Aerosol microphysics modules in the framework of the ECHAM5 climate model – intercomparison under stratospheric conditions, ***Geosci. Model Dev.***, ***2*** (2), 97–112, doi:10.5194/gmd-2-97-2009, 2009.

Kovilakam, M., L.W. Thomason, N. Ernest, L. Rieger, A. Bourassa, and L. Millán, The global space-based stratospheric aerosol climatology (version 2.0): 1979–2018, ***Earth Syst. Sci. Data***, ***12*** (4), 2607–2634, doi:10.5194/essd-12-2607-2020, 2020.

Kravitz, B., A. Robock, L. Oman, G. Stenchikov, and A.B. Marquardt, Sulfuric acid deposition from stratospheric geoengineering with sulfate aerosols, ***J. Geophys. Res. Atmos.***, ***114*** (D14), doi:10.1029/2009JD011918, 2009.

Kravitz, B., A. Robock, and A. Bourassa, Negligible climatic effects from the 2008 Okmok and Kasatochi volcanic eruptions, ***J. Geophys. Res.***, ***115*** (D2), doi:10.1029/2009JD013525, 2010.

Kravitz, B., A. Robock, O. Boucher, H. Schmidt, K.E. Taylor, G. Stenchikov, and M. Schulz, The geoengineering model intercomparison project (GeoMIP), ***Atmos. Sci. Lett.***, ***12*** (2), 162–167, doi:10.1002/asl.316, 2011.

Kravitz, B., A. Robock, D.T. Shindell, and M.A. Miller, Sensitivity of stratospheric geoengineering with black carbon to aerosol size and altitude of injection, ***J. Geophys. Res.***, ***117*** (D9), doi:10.1029/2011JD017341, 2012.

Kravitz, B., K. Caldeira, O. Boucher, A. Robock, P.J. Rasch, K. Alterskjær, D.B. Karam, J.N. Cole, C.L. Curry, J.M. Haywood, and P.J. Irvine, Climate model response from the geoengineering model intercomparison project (GeoMIP), ***J. Geophys. Res. Atmos.***, ***118*** (15), 8320–8332, doi:10.1002/jgrd.50646, 2013.

Kravitz, B., D.G. MacMartin, D.T. Leedal, P.J. Rasch, and A.J. Jarvis, Explicit feedback and the management of uncertainty in meeting climate objectives with solar geoengineering, ***Environ. Res. Lett.***, ***9*** (4), 044006, doi:10.1088/1748-9326/9/4/044006, 2014.

Kravitz, B., A. Robock, S. Tilmes, O. Boucher, J.M. English, P.J. Irvine, A. Jones, M.G. Lawrence, M. MacCracken, H. Muri, and J.C. Moore, The geoengineering model intercomparison project phase 6 (GeoMIP6): simulation design and preliminary results, ***Geosci. Model Dev.***, ***8*** (10), 3379–3392, doi:10.5194/gmd-8-3379-2015, 2015.

Kravitz, B., D.G. MacMartin, H. Wang, and P.J. Rasch, Geoengineering as a design problem, ***Earth Syst. Dynam.***, ***7***, 469–497, doi:10.5194/esd-7-469-2016, 2016.

Kravitz, B., D.G. MacMartin, M.J. Mills, J.H. Richter, S. Tilmes, J.F. Lamarque, J.J. Tribbia, and F. Vitt, First simulations of designing stratospheric sulfate aerosol geoengineering to meet multiple simultaneous climate objectives, ***J. Geophys. Res. Atmos.***, ***122*** (23), 12,616–12,634, doi:10.1002/2017JD026874, 2017.

Kravitz, B., D.G. MacMartin, S. Tilmes, J.H. Richter, M.J. Mills, W. Cheng, K. Dagon, A.S. Glanville, J.F. Lamarque, I.R. Simpson, and J. Tribbia, Comparing surface and stratospheric impacts of geoengineering with different SO2 injection strategies, ***J. Geophys. Res. Atmos.***, ***124*** (14), 7900–7918, doi:10.1029/2019JD030329, 2019.

Kravitz, B., D.G. MacMartin, D. Visioni, O. Boucher, J.N. Cole, J. Haywood, A. Jones, T. Lurton, P. Nabat, U. Niemeier, and A. Robock, Comparing different generations of idealized solar geoengineering simulations in the Geoengineering Model Intercomparison Project (GeoMIP), ***Atmos. Chem. Phys.***, ***21*** (6), 4231–4247, doi:10.5194/acp-21-4231-2021, 2021.

Kremser, S., L.W. Thomason, M. von Hobe, M. Hermann, T. Deshler, C. Timmreck, M. Toohey, A. Stenke, J.P. Schwarz, R. Weigel, and S. Fueglistaler, Stratospheric aerosol—Observations, processes, and impact on climate, ***Rev. Geophys.***, ***54*** (2), 278–335, doi:10.1002/2015RG000511, 2016.

Krishnamohan, K.P.S.P., G. Bala, L. Cao, L. Duan, and K. Caldeira, Climate system response to stratospheric sulfate aerosols: sensitivity to altitude of aerosol layer, ***Earth Syst. Dynam.***, ***10***, 885–900, doi:10.5194/esd-10-885-2019, 2019.

Kwiatkowski, L., P. Cox, P.R. Halloran, P.J. Mumby, and A.J. Wiltshire, Coral bleaching under unconventional scenarios of climate warming and ocean acidification, ***Nat. Clim. Change***, ***5*** (8), 777–781, doi:10.1038/nclimate2655, 2015.

Laakso, A., H. Korhonen, S. Romakkaniemi, and H. Kokkola, Radiative and climate effects of stratospheric sulfur geoengineering using seasonally varying injection areas, ***Atmos. Chem. Phys.***, ***17*** (11), 6957–6974, doi:10.5194/acp-17-6957-2017, 2017.

Laakso, A., U. Niemeier, D. Visioni, S. Tilmes, and H. Kokkola, Dependency of the impacts of geoengineering on the stratospheric sulfur injection strategy part 1: Intercomparison of modal and sectional aerosol module, ***Atmos. Chem. Phys.***, ***22***, 93–118, doi:10.5194/acp-22-93-2022, 2022.

Labitzke, K. and M.P. McCormick, Stratospheric temperature increases due to Pinatubo aerosols. ***Geophysical Research Letters***, ***19***(2), pp.207-210, 1992.

Labitzke, K., Stratospheric temperature changes after the Pinatubo eruption. ***Journal of Atmospheric and Terrestrial Physics***, ***56***(9), pp.1027-1034, 1994.

Lacis, A., J. Hansen, and M. Sato, Climate forcing by stratospheric aerosols, ***Geophys. Res. Lett.***, ***19*** (15), 1607–1610, doi:10.1029/92GL01620, 1992.

Lawrence, M.G., S. Schäfer, H. Muri, V. Scott, A. Oschlies, N.E. Vaughan, O. Boucher, H. Schmidt, J. Haywood, and J. Scheffran, Evaluating climate geoengineering proposals in the context of the Paris Agreement temperature goals, ***Nat. Commun.***, *9* (1), 1–19, doi:10.1038/s41467-018-05938-3, 2018.

Lee, J.-Y., J. Marotzke, G. Bala, L. Cao, S. Corti, J.P. Dunne, F. Engelbrecht, E. Fischer, J.C. Fyfe, C. Jones, A. Maycock, J. Mutemi, O. Ndiaye, S. Panickal, and T. Zhou, Future Global Climate: Scenario-Based Projections and Near-Term Information, Chapter 4, in ***Climate Change 2021: The Physical Science Basis. Contribution of Working Group I to the Sixth Assessment Report of the Intergovernmental Panel on Climate Change***, edited by V. Masson-Delmotte, P. Zhai, A. Pirani, S.L. Connors, C. Péan, S. Berger, N. Caud, Y. Chen, L. Goldfarb, M.I. Gomis, M. Huang, K. Leitzell, E. Lonnoy, J.B.R. Matthews, T.K. Maycock, T. Waterfield, O. Yelekçi, R. Yu, and B. Zhou, 120 pp., Cambridge University Press, Cambridge, United Kingdom, doi:10.1017/9781009157896.006, 2021.

Lee, W.R., D.G. MacMartin, D. Visioni, and B. Kravitz, High-latitude stratospheric aerosol geoengineering can be more effective if injection is limited to spring, ***Geophys. Res. Lett.***, *48* (9), e2021GL092696, doi:10.1029/2021GL092696, 2021.

Lehner, F., A.P. Schurer, G.C. Hegerl, C. Deser, and T.L. Frölicher, The importance of ENSO phase during volcanic eruptions for detection and attribution. ***Geophysical Research Letters***, *43*(6), pp.2851-2858, 2016.

Lenton, T.M., J. Rockström, O. Gaffney, S. Rahmstorf, K. Richardson, W. Steffen, and H.J. Schellnhuber, Climate tipping points—too risky to bet against, ***Nature***, 592–595, doi:10.1038/d41586-019-03595-0, 2019.

Lohmann, U., and B. Gasparini, A cirrus cloud climate dial?, ***Science***, *357* (6348), 248–249, doi:10.1126/science.aan3325, 2017.

Long J.C.S., and J.G. Shepherd, The strategic value of geoengineering research, in ***Global Environmental Change***, edited by B. Freedman, 13 pp., Springer, Dordrecht, Netherlands, doi:10.1007/978-94-007-5784-4_24, 2014.

Madronich, S., S. Tilmes, B. Kravitz, D.G. MacMartin, and J.H. Richter, Response of surface ultraviolet and visible radiation to stratospheric SO2 injections. ***Atmosphere***, *9*(11), p.432, 2018.

MacMartin, D.G., D.W. Keith, B. Kravitz, and K. Caldeira, Management of trade-offs in geoengineering through optimal choice of non-uniform radiative forcing, ***Nat. Clim. Change***, *3* (4), 365–368, doi:10.1038/nclimate1722, 2013.

MacMartin, D.G., B. Kravitz, D.W. Keith, and A. Jarvis, Dynamics of the coupled human–climate system resulting from closed-loop control of solar geoengineering, ***Clim. Dyn.***, *43* (1), 243–258, doi:10.1007/s00382-013-1822-9, 2014a.

MacMartin, D.G., K. Caldeira, and D.W. Keith, Solar geoengineering to limit the rate of temperature change, ***Philos. Trans. Royal Soc. A: Math. Phys. Eng. Sci.***, *372* (2031), 20140134, doi:10.1098/rsta.2014.0134, 2014b.

MacMartin, D.G., B. Kravitz, S. Tilmes, J.H. Richter, M.J. Mills, J.F. Lamarque, J.J. Tribbia, and F. Vitt, The climate response to stratospheric aerosol geoengineering can be tailored using multiple injection locations, ***J. Geophys. Res. Atmos.***, *122* (23), 12,574–12,590, doi:10.1002/2017JD026868, 2017.

MacMynowski, D.G., D.W. Keith, K. Caldeira, and H.J. Shin, Can we test geoengineering?, ***Energy Environ. Sci.***, *4* (12), 5044–5052, doi:10.1039/C1EE01256H, 2011.

Mankin, W.G., and M.T. Coffey, Increased stratospheric hydrogen chloride in the El Chichon cloud, ***Science***, *226* (4671), 170–172, doi:10.1126/science.226.4671.170, 1984.

Marshall, L.R., C.J. Smith, P.M. Forster, T.J. Aubry, T. Andrews, and A. Schmidt, Large variations in volcanic aerosol forcing efficiency due to eruption source parameters and rapid adjustments, ***Geophys. Res. Lett.***, *47* (19), e2020GL090241, doi:10.1029/2020GL090241, 2020.

Matthews, H.D., and S.E. Turner, Of mongooses and mitigation: ecological analogues to geoengineering, ***Environ. Res. Lett.***, *4* (4), 045105, doi:10.1088/1748-9326/4/4/045105, 2009.

McClellan, J., D.W. Keith, and J. Apt, Cost analysis of stratospheric albedo modification delivery systems, ***Environ. Res. Lett.***, *7* (3), 034019, doi:10.1088/1748-9326/7/3/034019, 2012.

McCormick, M.P., L.W. Thomason, and C.R. Trepte, Atmospheric effects of the Mt Pinatubo eruption, ***Nature***, *373* (6513), 399–404, doi:10.1038/373399a0, 1995.

McCusker, K.E., D.S. Battisti, and C.M. Bitz, Inability of stratospheric sulfate aerosol injections to preserve the West Antarctic Ice Sheet, ***Geophys. Res. Lett.***, *42* (12), 4989–4997, doi:10.1002/2015GL064314, 2015.

Mie, G., Sättigungsstrom und Stromkurve einer schlecht leitenden Flüssigkeit, ***Ann. Phys.***, *331* (8), 597–614, doi:10.1002/andp.19083310810, 1908.

Millar, R.J., J.S. Fuglestvedt, P. Friedlingstein, J. Rogelj, M.J. Grubb, H.D. Matthews, R.B. Skeie, P.M. Forster, D.J. Frame, and M.R. Allen, Emission budgets and pathways consistent with limiting warming to 1.5 °C, ***Nat. Geosci.***, *10* (10), 741–747, doi:10.1038/ngeo3031, 2017.

Mills, M.J., A. Schmidt, R. Easter, S. Solomon, D.E. Kinnison, S.J. Ghan, R.R. Neely III, D.R. Marsh, A. Conley, C.G. Bardeen, and A. Gettelman, Global volcanic aerosol properties derived from emissions, 1990–2014, using CESM1 (WACCM), ***J. Geophys. Res. Atmos.***, *121* (5), 2332–2348, doi:10.1002/2015JD024290, 2016.

Mills, M.J., J.H. Richter, S. Tilmes, B. Kravitz, D.G. MacMartin, A.A. Glanville, J.J. Tribbia, J.F. Lamarque, F. Vitt, A. Schmidt, and A. Gettelman, Radiative and chemical response to interactive stratospheric sulfate aerosols in fully coupled CESM1 (WACCM), ***J. Geophys. Res. Atmos.***, *122* (23), 13,061–13,078, doi:10.1002/2017JD027006, 2017.

Minnis, P., E.F. Harrison, L.L. Stowe, G.G. Gibson, F.M. Denn, D.R. Doelling, and W.L. Smith Jr, Radiative climate forcing by the Mount Pinatubo eruption, ***Science***, ***259*** (5100), 1411–1415, doi:10.1126/science.259.5100.1411, 1993.

Molina, M.J., L.T. Molina, R. Zhang, R.F. Meads, and D.D. Spencer, The reaction of ClONO2 with HCl on aluminum oxide, ***Geophys. Res. Lett.***, *24* (13), 1619–1622, doi:10.1029/97GL01560, 1997.

Moon, D.R., G.S. Taverna, C. Anduix-Canto, T. Ingham, M.P. Chipperfield, P.W. Seakins, M.T. Baeza-Romero, and D.E. Heard, Heterogeneous reaction of HO 2 with airborne TiO 2 particles and its implication for climate change mitigation strategies, ***Atmos. Chem. Phys.***, *18* (1), 327–338, doi:10.5194/acp-18-327-2018, 2018.

Morgenstern, O., M.I. Hegglin, E. Rozanov, F.M. O'Connor, N.L. Abraham, H. Akiyoshi, A.T. Archibald, S. Bekki, N. Butchart, M.P. Chipperfield, M. Deushi, S.S. Dhoms, R.R. Garcia, S.C. Hardiman, L.W. Horowitz, P. Jöckel, B. Josse, D. Kinnison, M. Lin, E. Mancini, M.E. Manyin, M. Marchand, V. Marécal, M. Michou, L.D. Oman, G. Pitari, D.A. Plummer, L.E. Revell, D, Saint-Martin, R. Schofield, A. Stenke, K. Stone, K. Sudo, T.Y. Tanaka, S. Tilmes, Y. Yamashita, K. Yoshida, and G. Zeng, Review of the global models used within phase 1 of the Chemistry–Climate Model Initiative (CCMI), ***Geosci. Model Dev.***, *10* (2), 639–671, doi:10.5194/gmd-10-639-2017, 2017.

Muser, L.O., G.A. Hoshyaripour, J. Bruckert, Á. Horváth, E. Malinina, S. Wallis, F.J. Prata, A. Rozanov, C. von Savigny, H. Vogel, and B. Vogel, Particle aging and aerosol–radiation interaction affect volcanic plume dispersion: evidence from the Raikoke 2019 eruption, ***Atmos. Chem. Phys.***, *20* (23), 15,015–15,036, doi:10.5194/acp-20-15015-2020, 2020.

Muthyala, R., G. Bala, and A. Nalam, Regional scale analysis of climate extremes in an SRM geoengineering simulation, Part 1: Precipitation Extremes, ***Curr. Sci.***, *114* (5), 1024–1035, doi:10.18520/cs/v114/i05/1024-1035, 2018a.

Muthyala, R., G. Bala, and A. Nalam, Regional scale analysis of climate extremes in an SRM geoengineering simulation, Part 2: Temperature Extremes, ***Curr. Sci.***, *114* (5), 1036–1045, doi:10.18520/cs/v114/i05/1036-1045, 2018b.

Myhre, G., K. Alterskjær, C.W. Stjern, Ø. Hodnebrog, L. Marelle, B.H. Samset, J. Sillmann, N. Schaller, E. Fischer, M. Schulz, and A. Stohl, Frequency of extreme precipitation increases extensively with event rareness under global warming, ***Sci. Rep.***, *9* (1), 1–10, doi:10.1038/s41598-019-52277-4, 2019.

NAS (U.S. National Academy of Sciences), ***Reflecting Sunlight: Recommendations for Solar Geoengineering Research and Research Governance***, 328 pp., The National Academies Press, Washington, DC, doi:10.17226/25762, 2021.

NRC (National Research Council), ***Climate Intervention: Carbon Dioxide Removal and Reliable Sequestration***, 154 pp., The National Academies Press, Washington, DC, doi:10.17226/18805, 2015.

Neely III, R.R and A. Schmidt, VolcanEESM: Global volcanic sulphur dioxide (SO2) emissions database from 1850 to present. *Centre for Environmental Data Analysis*. https://doi.org/10.5285/76ebdc0b-0eed-4f70-b89e-55e606bcd568, 2016.

Niemeier, U., H. Schmidt, and C. Timmreck, The dependency of geoengineered sulfate aerosol on the emission strategy, ***Atmos. Sci. Lett.***, *12* (2), 189–194, doi:10.1002/asl.304, 2011.

Niemeier, U., H. Schmidt, K. Alterskjær, and J.E. Kristjánsson, Solar irradiance reduction via climate engineering: Impact of different techniques on the energy balance and the hydrological cycle, ***J. Geophys. Res. Atmos.***, *118*, 11,905–11,917, doi:10.1002/2013JD020445, 2013.

Niemeier, U., and C. Timmreck, What is the limit of climate engineering by stratospheric injection of SO2?, ***Atmos. Chem. Phys.***, *15* (16), 9129–9141, doi:10.5194/acp-15-9129-2015, 2015.

Niemeier, U., and H. Schmidt, Changing transport processes in the stratosphere by radiative heating of sulfate aerosols, ***Atmos. Chem. Phys.***, *17*, 14,871–14,886, doi:10.5194/acp-17-14871-2017, 2017.

Niemeier, U., J.H. Richter, and S. Tilmes, Differing responses of the quasi-biennial oscillation to artificial SO2 injections in two global models, ***Atmos. Chem. Phys.***, *20*, 8975–8987, doi:10.5194/acp-20-8975-2020, 2020.

Nowack, P.J., N.L. Abraham, P. Braesicke, and J.A. Pyle, Stratospheric ozone changes under solar geoengineering: implications for UV exposure and air quality, ***Atmos. Chem. Phys.***, *16* (6), 4191–4203, doi:10.5194/acp-16-4191-2016, 2016.

Oman, L., A. Robock, G.L. Stenchikov, and T. Thordarson, High-latitude eruptions cast shadow over the African monsoon and the flow of the Nile, ***Geophys. Res. Lett.***, *33* (18), doi:10.1029/2006GL027665, 2006.

Osborne, M.J., J. de Leeuw, C. Witham, A. Schmidt, F. Beckett, N. Kristiansen, J. Buxmann, C. Saint, E.J. Welton, J. Fochesatto, A.R. Gomes, U. Bundke, A. Petzold, F. Marenco, and J. Haywood, The 2019 Raikoke volcanic eruption part 2: Particle phase dispersion and concurrent wildfire smoke emissions, ***Atmos. Chem. Phys.***, *22* (5), 2975–2997, doi:10.5194/acp-2021-448, 2022.

Parker, A. and P.J. Irvine, P.J., The risk of termination shock from solar geoengineering. ***Earth's Future***, *6*(3), pp.456-467, 2018.

Peterson, D.A., J.R. Campbell, E.J. Hyer, M.D. Fromm, G.P. Kablick III, J.H. Cossuth, and M.T. DeLand, Wildfire-driven thunderstorms cause a volcano-like stratospheric injection of smoke, ***npj Clim. Atmos. Sci.***, *1* (1), doi:10.1038/s41612-018-0039-3, 2018.

Peterson, D.A., M.D. Fromm, R.H.D. McRae, J.R. Campbell, E.J. Hyer, G. Taha, C.P. Camacho, G.P. Kablick III, C.C. Schmidt, and M.T. DeLand, Australia's Black Summer pyrocumulonimbus super outbreak reveals potential for increasingly extreme stratospheric smoke events, ***npj Clim. Atmos. Sci.***, *4* (1), doi:10.1038/s41612-021-00192-9, 2021.

Pierce, J.R., D.K. Weisenstein, P. Heckendorn, T. Peter, and D.W. Keith, Efficient formation of stratospheric aerosol for climate engineering by emission of condensible vapor from aircraft, ***Geophys. Res. Lett.***, *37* (18), doi:10.1029/2010GL043975, 2010.

Pinto, J.P., R.P. Turco, and O.B. Toon, Self-limiting physical and chemical effects in volcanic eruption clouds, ***J. Geophys. Res. Atmos.***, *94* (D8), 11,165–11,174, doi:10.1029/JD094iD08p11165, 1989.

Pitari, G., and E. Mancini, Short-term climatic impact of the 1991 volcanic eruption of Mount Pinatubo and effects on atmospheric tracers, ***Nat. Hazards Earth Syst. Sci.***, *2* (1/2), 91–108, doi:10.5194/nhess-2-91-2002, 2002.

Pitari, G., V. Aquila, B. Kravitz, A. Robock, S. Watanabe, I. Cionni, N.D. Luca, G.D. Genova, E. Mancini, and S. Tilmes, Stratospheric ozone response to sulfate geoengineering: Results from the Geoengineering Model Intercomparison Project (GeoMIP), ***J. Geophys. Res. Atmos.***, *119* (5), 2629–2653, doi:10.1002/2013JD020566, 2014.

Plummer, D., T. Nagashima, S. Tilmes, A. Archibald, G. Chiodo, S. Fadnavis, H. Garny, B. Josse, J. Kim, J.-F. Lamarque, O. Morgenstern, L. Murray, C. Orbe, A. Tai, M. Chipperfield, B. Funke, M. Juckes, D. Kinnison, M. Kunze, B. Luo, K. Matthes, P.A. Newman, C. Pascoe, and T. Peter, CCMI-2022: A new set of Chemistry-Climate Model Initiative (CCMI) Community Simulations to Update the Assessment of Models and Support Upcoming Ozone Assessment Activities, SPARC newsletter, [available at: https://www.sparc-climate.org/wp-content/uploads/sites/5/2021/07/SPARCnewsletter_Jul2021_web.pdf#page=22], 2021.

Poberaj, C.S., J. Staehelin, and D. Brunner, Missing stratospheric ozone decrease at Southern Hemisphere middle latitudes after Mount Pinatubo: a dynamical perspective, ***J Atmos Sci.***, *68* (9), 1922–1945, doi:10.1175/JAS-D-10-05004.1, 2011.

Polvani, L.M., A. Banerjee, and A. Schmidt, Northern Hemisphere continental winter warming following the 1991 Mount Pinatubo eruption: reconciling models and observations, ***Atmos. Chem. Phys.***, *19* (9), 6351–6366, doi:10.5194/acp-19-6351-2019, 2019.

Pope, F.D., P. Braesicke, R.G. Grainger, M. Kalberer, I.M. Watson, P.J. Davidson, and R.A. Cox, Stratospheric aerosol particles and solar-radiation management, ***Nat. Clim. Change***, *2* (10), 713–719, doi:10.1038/nclimate1528, 2012.

Portmann, R.W., S. Solomon, R.R. Garcia, L.W. Thomason, L.R. Poole, and M.P. McCormick, Role of aerosol variations in anthropogenic ozone depletion in the polar regions, ***J. Geophys. Res. Atmos.***, *101* (D17), 22,991–23,006, doi:10.1029/96JD02608, 1996.

Preston, C.J., Ethics and geoengineering: reviewing the moral issues raised by solar radiation management and carbon dioxide removal, ***Wiley Interdiscip. Rev. Clim. Change***, *4* (1), 23–37, doi:10.1002/wcc.198, 2013.

Proctor, J., S. Hsiang, J. Burney, M. Burke, and W. Schlenker, Estimating global agricultural effects of geoengineering using volcanic eruptions, ***Nature***, *560* (7719), 480–483, doi:10.1038/s41586-018-0417-3, 2018.

Quaglia, I., D. Visioni, G. Pitari, and B. Kravitz, An approach to sulfate geoengineering with surface emissions of carbonyl sulfide. ***Atmos. Chem. Phys***, *22*(9), pp.5757-5773, 2022.

Randel, W.J., F. Wu, J.M. Russell III, J.W. Waters, and L. Froidevaux, Ozone and temperature changes in the stratosphere following the eruption of Mount Pinatubo, ***J. Geophys. Res. Atmos.***, *100* (D8), 16,753–16,764, doi:10.1029/95JD01001, 1995.

Rasch, P.J., S. Tilmes, R.P. Turco, A. Robock, L. Oman, C.C. Chen, G.L. Stenchikov, and R.R. Garcia, An overview of geoengineering of climate using stratospheric sulphate aerosols, ***Philos. Trans. Royal Soc. A: Math. Phys. Eng. Sci.***, *366* (1882), 4007–4037, doi:10.1098/rsta.2008.0131, 2008a.

Rasch, P.J., P.J. Crutzen, and D.B. Coleman, Exploring the geoengineering of climate using stratospheric sulfate aerosols: the role of particle size, ***Geophys. Res. Lett.***, *35* (2), L02809, doi:10.1029/2007GL032179, 2008b.

Ravishankara, A.R., J.S. Daniel, and R.W. Portmann, R.W., Nitrous oxide (N2O): the dominant ozone-depleting substance emitted in the 21st century. ***science***, *326*(5949), pp.123-125, 2009.

Richter, J. H., S. Tilmes ,M.J. Mills, J.J. Tribbia, B. Kravitz, D.G. MacMartin, F. Vitt, and J.-F. Lamarque, Stratospheric dynamical response and ozone feedbacks in the presence of SO_2 injections, ***J. Geophys. Res. Atmos.***, *122*, 12,557–12,573, doi:10.1002/2017JD026912, 2017.

Richter, J. H., S. Tilmes, A. Glanville, B. Kravitz, D.G. MacMartin, M.J. Mills, I.R. Simpson, F. Vitt, J.J. Tribbia, and J.-F. Lamarque, Stratospheric response in the first geoengineering simulation meeting multiple surface climate objectives, ***J. Geophys. Res. Atmos.***, *123* (11), 5762–5782, doi:10.1029/2018JD028285, 2018.

Richter, J.H., D. Visioni, D. MacMartin, D.A. Bailey, W. Lee, S. Woodhouse, N.A. Rosenbloom, M.R. Tye, and J.F. Lamarque, Assessing Responses and Impacts of Solar climate intervention on the Earth system with stratospheric aerosol injection (ARISE-SAI): protocol and initial results from the first simulations, ***Geosci. Model Dev.***, 15, 8221–8243, https://doi.org/10.5194/gmd-15-8221-2022, 2022.

Rieger, L.A., W.J. Randel, A.E. Bourassa, and S. Solomon,. Stratospheric temperature and ozone anomalies associated with the 2020 Australian New Year fires, ***Geophys. Res. Lett.***, *48*, e2021GL095898, doi:10.1029/2021GL095898, 2021.

Robock, A. and J. Mao, Winter warming from large volcanic eruptions. ***Geophysical Research Letters***, *19*(24), pp.2405-2408, 1992.

Robock, A., and J. Mao, The volcanic signal in surface temperature observations, ***J. Clim.***, *8* (5), 1086–1103, doi:10.1175/1520-0442(1995)008<1086:TVSIST>2.0.CO;2, 1995.

Robock, A., Volcanic eruptions and climate, ***Rev. Geophys.***, *38* (2), 191–219, doi:10.1029/1998RG000054, 2000.

Robock, A., 20 reasons why geoengineering may be a bad idea, ***Bull. At. Sci.***, *64* (2), 14–18, doi:10.2968/064002006, 2008a.

Robock, A., L. Oman, and G.L. Stenchikov, Regional climate responses to geoengineering with tropical and Arctic SO2 injections, ***J. Geophys. Res.***, *113* (D16), D16101, doi:10.1029/2008JD010050, 2008b.

Robock, A., A. Marquardt, B. Kravitz, and G. Stenchikov, Benefits, risks, and costs of stratospheric geoengineering, ***Geophys. Res. Lett.***, *36* (19), doi:10.1029/2009GL039209, 2009.

Robock, A., Benefits and risks of stratospheric solar radiation management for climate intervention (geoengineering), ***Bridge***, *50* (1), 59–67, [available at: http://climate.envsci.rutgers.edu/pdf/RobockBridge.pdf], 2020.

Robrecht, S., B. Vogel, S. Tilmes, and R. Müller, Potential of future stratospheric ozone loss in the midlatitudes under global warming and sulfate geoengineering, ***Atmos. Chem. Phys.***, *21* (4), 2427–2455, doi:10.5194/acp-21-2427-2021, 2021.

Rogelj, J., M. den Elzen, N. Höhne, T. Fransen, H. Fekete, H. Winkler, R. Schaeffer, F. Sha, K. Riahi, and M. Meinshausen, Paris Agreement climate proposals need a boost to keep warming well below 2 °C, ***Nature***, *534* (7609), 631–639, doi:10.1038/nature18307, 2016.

Rogelj, J., O. Geden, A. Cowie, and A. Reisinger, Net-zero emissions targets are vague: three ways to fix, ***Nature***, ***591***, 365–368, doi:10.1038/d41586-021-00662-3, 2021.

Rosenfeld, J.E., D.B. Considine, P.E. Meade, J.T. Bacmeister, C.H. Jackman, and M.R. Schoeberl, Stratospheric effects of Mount Pinatubo aerosol studied with a coupled two-dimensional model, ***J. Geophys. Res. Atmos.***, ***102*** (D3), 3649–3670, doi:10.1029/96JD03820, 1997.

Samaniego, L., S. Thober, R. Kumar, N. Wanders, O. Rakovec, M. Pan, M. Zink, J. Sheffield, E.F. Wood, and A. Marx, Anthropogenic warming exacerbates European soil moisture droughts, ***Nat. Clim. Change***, ***8*** (5), 421–426, doi:10.1038/s41558-018-0138-5, 2018.

Santer, B.D., C. Bonfils, J.F. Painter, M.D. Zelinka, C. Mears, S. Solomon, G.A. Schmidt, J.C. Fyfe, J.N. Cole, L. Nazarenko, and K.E. Taylor, Volcanic contribution to decadal changes in tropospheric temperature, ***Nat. Geosci.***, ***7*** (3), 185–189, doi:10.1038/ngeo2098, 2014.

Schmidt, A., M.J. Mills, S. Ghan, J.M. Gregory, R.P. Allan, T. Andrews, C.G. Bardeen, A. Conley, P.M. Forster, A. Gettelman, and R.W. Portmann, Volcanic radiative forcing from 1979 to 2015, ***J. Geophys. Res. Atmos.***, ***123*** (22), 12,491–12,508, doi:10.1029/2018JD028776, 2018.

Schmidt, H., K. Alterskjær, D. Bou Karam, O. Boucher, A. Jones, J.E. Kristjánsson, U. Niemeier, M. Schulz, A. Aaheim, F. Benduhn, and M. Lawrence, Solar irradiance reduction to counteract radiative forcing from a quadrupling of CO2: climate responses simulated by four earth system models, ***Earth Syst. Dyn.***, ***3*** (1), 63–78, doi:10.5194/esd-3-63-2012, 2012.

Schwartz, M.J., M.L. Santee, H.C. Pumphrey, G.L. Manney, A. Lambert, N.J. Livesey, L. Millán, J.L. Neu, W.G. Read, and F. Werner, Australian new year's pyroCb impact on stratospheric composition, ***Geophys. Res. Lett.***, ***47*** (24), e2020GL090831, doi:10.1029/2020GL090831, 2020.

Seinfeld, J.H., and S.N. Pandis, *Atmospheric Chemistry and Physics: From Air Pollution to Climate Change*, 2nd Edition, John Wiley & Sons, New York, NY, 2007.

Shepherd, J.G., *Geoengineering the climate: science, governance and uncertainty*, 99 pp., Royal Society, London, United Kingdom, 2009.

Shi, Q., J.T. Jayne, C.E. Kolb, D.R. Worsnop, and P. Davidovits, Kinetic model for reaction of ClONO2 with H2O and HCl and HOCl with HCl in sulfuric acid solutions, ***J. Geophys. Res. Atmos.***, ***106*** (D20), 24,259–24,274, doi:10.1029/2000JD000181, 2001.

Simpson, I.R., S. Tilmes, J.H. Richter, B. Kravitz, D.G. MacMartin, M.J. Mills, J.T. Fasullo, and A.G. Pendergrass, The regional hydroclimate response to stratospheric sulfate geoengineering and the role of stratospheric heating, ***J. Geophys. Res. Atmos.***, ***124*** (23), 12,587–12,616, doi:10.1029/2019JD031093, 2019.

Smith, P., S.J. Davis, F. Creutzig, S. Fuss, J. Minx, B. Gabrielle, E. Kato, R.B. Jackson, A. Cowie, E. Kriegler, D.P. van Vuuren, J. Rogelj, P. Ciais, J. Milne, J.G. Canadell, D. McCollum, G. Peters, R. Andrew, V. Krey, G. Shrestha, P. Friedlingstein, T. Gasser, A. Grübler, W.K. Heidug, M. Jonas, C.D. Jones, F. Kraxner, E. Littleton, J. Lowe, J.R. Moreira, N. Nakicenovic, M. Obersteiner, A. Patwardhan, M. Rogner, E. Rubin, A. Sharifi, A. Torvanger, Y. Yamagata, J. Edmonds, and C. Yongsung, Biophysical and economic limits to negative CO2 emissions, ***Nat. Clim. Change***, ***6*** (1), 42–50, doi:10.1038/nclimate2870, 2016.

Smith, W., and Wagner, G., Stratospheric aerosol injection tactics and costs in the first 15 years of deployment, ***Environ. Res. Lett.***, ***13*** (12), 124001, doi:10.1088/1748-9326/aae98d, 2018.

Smith, W., The cost of stratospheric aerosol injection through 2100, ***Environ. Res. Lett.***, ***15*** (11), 114004, doi:10.1088/1748-9326/aba7e7, 2020.

Soden, B.J., R.T. Wetherald, G.L. Stenchikov, and A. Robock, Global cooling after the eruption of Mount Pinatubo: A test of climate feedback by water vapor, ***Science***, ***296*** (5568), 727–730, 10.1126/science.296.5568.727, 2002.

Solomon, S., R.W. Portmann, R.R. Garcia, L.W. Thomason, L.R. Poole, and M.P. McCormick, The role of aerosol variations in anthropogenic ozone depletion at northern midlatitudes, ***J. Geophys. Res. Atmos.***, ***101*** (D3), 6713–6727, doi:10.1029/95JD03353, 1996.

Solomon, S., R.W. Portmann, R.R. Garcia, W. Randel, F. Wu, R. Nagatani, J. Gleason, L. Thomason, L.R. Poole, and M.P. McCormick, Ozone depletion at mid-latitudes: Coupling of volcanic aerosols and temperature variability to anthropogenic chlorine, ***Geophys. Res. Lett.***, ***25*** (11), 1871–1874, doi:10.1029/98GL01293, 1998.

Solomon, S., Stratospheric ozone depletion: A review of concepts and history, ***Rev. Geophys.***, ***37*** (3), 275–316, doi:10.1029/1999RG900008, 1999.

Solomon, S., D.J. Ivy, D. Kinnison, M.J. Mills, R.R. Neely III, and A. Schmidt, Emergence of healing in the Antarctic ozone layer, ***Science***, ***353*** (6296), 269–274, doi:10.1126/science.aae0061, 2016.

Solomon, S., K. Dube, K. Stone, K., P. Yu, D. Kinnison, O.B. Toon, S.E. Strahan, K.H. Rosenlof, R. Portmann, S. Davis, and W. Randel, 2022. On the stratospheric chemistry of midlatitude wildfire smoke. ***Proceedings of the National Academy of Sciences***, ***119***(10), p.e2117325119, 2022.

SPARC (Stratospheric Processes And their Role in Climate), ***SPARC Assessment of Stratospheric Aerosol Properties (ASAP)***, edited by L. Thomason and T. Peter, SPARC Report No. 4, WCRP-124, WMO/TD No. 1295, [available at: www.sparc-climate.org/publications/sparc-reports/], 2006.

Staunton-Sykes, J., T.J. Aubry, Y.M. Shin, J. Weber, L.R. Marshall, N. Luke Abraham, A. Archibald, and A. Schmidt, Co-emission of volcanic sulfur and halogens amplifies volcanic effective radiative forcing, ***Atmos. Chem. Phys.***, ***21*** (11), 9009–9029, doi:10.5194/acp-21-9009-2021, 2021.

Stenchikov, G., A. Ukhov, S. Osipov, R. Ahmadov, G. Grell, K. Cady-Pereira, E. Mlawer, and M. Iacono, How does a Pinatubo-size volcanic cloud reach the middle stratosphere?, ***J. Geophys. Res. Atmos.***, ***126*** (10), e2020JD033829, doi:10.1029/2020JD033829, 2021.

Stephens, G.L., M.Z. Hakuba, M. Hawcroft, J.M. Haywood, A. Behrangi, J.E. Kay, and P.J Webster, The curious nature of the hemispheric symmetry of the Earth's water and energy balances, ***Curr. Clim. Change Rep.***, ***2*** (4), 135–147, doi:10.1007/s40641-016-0043-9, 2016.

Stone, K.A., S. Solomon, D.E. Kinnison, M.C. Pitts, L.R. Poole, M.J. Mills, A. Schmidt, R.R. Neely III, D. Ivy, M.J. Schwartz, J.P. Vernier, B.J. Johnson, M.B. Tully, A.R. Klekociuk, G. König-Langlo, and S. Hagiya, Observing the impact of Calbuco volcanic aerosols on South Polar ozone depletion in 2015, ***J. Geophys. Res. Atmos.***, ***122*** (21), 11,862–11,879, doi:10.1002/2017JD026987, 2017.

Sugiyama, M., Y. Arino, T. Kosugi, A. Kurosawa, and S. Watanabe, Next steps in geoengineering scenario research: Limited deployment scenarios and beyond, ***Clim. Policy***, ***18*** (6), 681–689, doi:10.1080/14693062.2017.1323721, 2018.

Tang, M., J. Keeble, P.J. Telford, F.D. Pope, P. Braesicke, P.T. Griffiths, N.L. Abraham, J. McGregor, I.M. Watson, R.A. Cox, and J.A. Pyle, Heterogeneous reaction of $ClONO_2$ with TiO_2 and SiO_2 aerosol particles: implications for stratospheric particle injection for climate engineering, ***Atmos. Chem. Phys.***, ***16*** (23), 15,397–15,412, doi:10.5194/acp-16-15397-2016, 2016.

Tang, M.J., P.J. Telford, F.D. Pope, L. Rkiouak, N.L. Abraham, A.T. Archibald, P. Braesicke, J.A. Pyle, J. McGregor, I.M. Watson, and R.A. Cox, Heterogeneous reaction of N_2O_5 with airborne TiO_2 particles and its implication for stratospheric particle injection, ***Atmos. Chem. Phys.***, ***14*** (12), 6035–6048, doi:10.5194/acp-14-6035-2014, 2014.

Telford, P., P. Braesicke, O. Morgenstern, and J. Pyle, Reassessment of causes of ozone column variability following the eruption of Mount Pinatubo using a nudged CCM, ***Atmos. Chem. Phys.***, ***9*** (13), 4251–4260, doi:10.5194/acp-9-4251-2009, 2009.

Theys, N., I.D. Smedt, H. Yu, T. Danckaert, J.V. Gent, C. Hörmann, T. Wagner, P. Hedelt, H. Bauer, F. Romahn, and M. Pedergnana, Sulfur dioxide retrievals from TROPOMI onboard Sentinel-5 Precursor: algorithm theoretical basis, ***Atmos. Meas. Tech.***, ***10*** (1), 119–153, doi:10.5194/amt-10-119-2017, 2017.

Thomason, L.W., G.S. Kent, C.R. Trepte, and L.R. Poole, A comparison of the stratospheric aerosol background periods of 1979 and 1989–1991, ***J. Geophys. Res. Atmos.***, ***102*** (D3), 3611–3616, doi:10.1029/96JD02960, 1997.

Thomason, L.W., N. Ernest, L. Millán, L. Rieger, A. Bourassa, J.P. Vernier, G. Manney, B. Luo, F. Arfeuille, and T. Peter, A global space-based stratospheric aerosol climatology: 1979–2016, ***Earth Syst. Sci. Data***, ***10*** (1), 469–492, doi:10.5194/essd-10-469-2018, 2018.

Tie, X., and G. Brasseur, The response of stratospheric ozone to volcanic eruptions: Sensitivity to atmospheric chlorine loading, ***Geophys. Res. Lett.***, ***22*** (22), 3035–3038, doi:10.1029/95GL03057, 1995.

Tie, X., G.P. Brassuer, C. Granier, A. De Rudder, and N. Larsen, Model study of polar stratospheric clouds and their effect on stratospheric ozone: 2. Model results, ***J. Geophys. Res. Atmos.***, ***101*** (D7), 12,575–12,584, doi:10.1029/96JD00403, 1996.

Tilmes, S., R. Müller, J.U. Grooß, and J.M. Russell III, Ozone loss and chlorine activation in the Arctic winters 1991-2003 derived with the tracer-tracer correlations. ***Atmospheric Chemistry and Physics***, ***4***(8), pp.2181-2213, 2004.

Tilmes, S., R. Müller, and R. Salawitch, The sensitivity of polar ozone depletion to proposed geo-engineering schemes, ***Science***, ***320*** (5880), 1201–1204, doi:10.1126/science.1153966, 2008.

Tilmes, S., R.R. Garcia, D.E. Kinnison, A. Gettelman, and P.J. Rasch, Impact of geoengineered aerosols on the troposphere and stratosphere, ***J. Geophys. Res. Atmos.***, ***114*** (D12), doi:10.1029/2008JD011420, 2009.

Tilmes, S., Kinnison, D. E., Garcia, R. R., Salawitch, R., Canty, T., Lee-Taylor, J., Madronich, S., and Chance, K.: Impact of very short-lived halogens on stratospheric ozone abundance and UV radiation in a geo-engineered atmosphere, Atmos. Chem. Phys., 12, 10945–10955, https://doi.org/10.5194/acp-12-10945-2012, 2012.

Tilmes, S., J. Fasullo, J.F. Lamarque, D.R. Marsh, M. Mills, K. Alterskjær, H. Muri, J.E. Kristjánsson, O. Boucher, M. Schulz, and J.N. Cole, The hydrological impact of geoengineering in the Geoengineering Model Intercomparison Project (GeoMIP), ***J. Geophys. Res. Atmos.***, ***118*** (19), 11,036–11,058, doi:10.1002/jgrd.50868, 2013.

Tilmes, S., B.M. Sanderson, and B.C. O'Neill, Climate impacts of geoengineering in a delayed mitigation scenario, ***Geophys. Res. Lett.***, ***43*** (15), 8222–8229, doi:10.1002/2016GL070122, 2016.

Tilmes, S., J.H. Richter, M.J. Mills, B. Kravitz, D.G. MacMartin, F. Vitt, J.J. Tribbia, and J.-F. Lamarque, Sensitivity of aerosol distribution and climate response to stratospheric SO2 injection locations, ***J. Geophys. Res. Atmos.***, ***122*** (23), 12,591–12,615, doi:10.1002/2017JD026888, 2017.

Tilmes, S., J.H. Richter, B. Kravitz, D.G. MacMartin, M.J. Mills, I.R. Simpson, A.S. Glanville, J.T. Fasullo, A.S. Phillips, J.-F. Lamarque, J. Tribbia, J. Edwards, J., S. Mickelson, and S. Ghosh, CESM1 (WACCM) stratospheric aerosol geoengineering large ensemble project, ***Bull. Am. Meteorol. Soc., 99*** (11), 2361–2371, doi:10.1175/BAMS-D-17-0267.1, 2018a.

Tilmes, S., J.H. Richter, M.J. Mills, B. Kravitz, D.G. MacMartin, R.R. Garcia, D.E. Kinnison, J.-F. Lamarque, J. Tribbia, and F. Vitt, Effects of different stratospheric SO_2 injection altitudes on stratospheric chemistry and dynamics, ***J. Geophys. Res. Atmos.***, ***123***, 4654–4673, doi:10.1002/2017JD028146, 2018b.

Tilmes, S., D.G. MacMartin, J. Lenaerts, L.V. Kampenhout, L. Muntjewerf, L. Xia, C.S. Harrison, K.M. Krumhardt, M.J. Mills, B. Kravitz, and A. Robock, Reaching 1.5 and 2.0 °C global surface temperature targets using stratospheric aerosol geoengineering, ***Earth Syst. Dyn.***, ***11*** (3), 579–601, doi:10.5194/esd-11-579-2020, 2020.

Tilmes, S., J.H. Richter, B. Kravitz, D.G. MacMartin, A.S. Glanville, D. Visioni, D.E. Kinnison, and R. Müller, Sensitivity of total column ozone to stratospheric sulfur injection strategies, ***Geophys. Res. Lett.***, ***48*** (19), e2021GL094058, doi:10.1029/2021GL094058, 2021.

Tilmes, S., D. Visioni, A. Jones, J. Haywood, R. Séférian, P. Nabat, O. Boucher, E.M. Bednarz, and U. Niemeier, Stratospheric ozone response to sulfate aerosol and solar dimming climate interventions based on the G6 Geoengineering Model Intercomparison Project (GeoMIP) simulations, ***Atmos. Chem. Phys.***, ***22*** (7), 4557–4579, doi:10.5194/acp-2021-1003, 2022.

Timmreck, C., and H.-F. Graf, The initial dispersal and radiative forcing of a Northern Hemisphere mid-latitude super volcano: a model study, ***Atmos. Chem. Phys.***, ***6***, 35–49, doi:10.5194/acp-6-35-2006, 2006.

Timmreck, C., S.J. Lorenz, T.J. Crowley, S. Kinne, T.J. Raddatz, M.A. Thomas, and J.H. Jungclaus, Limited temperature response to the very large AD 1258 volcanic eruption, ***Geophys. Res. Lett.***, ***36*** (21), doi:10.1029/2009GL040083, 2009.

Timmreck, C., H.F. Graf, S.J. Lorenz, U. Niemeier, D. Zanchettin, D. Matei, J.H. Jungclaus, and T.J. Crowley, Aerosol size confines climate response to volcanic super-eruptions, ***Geophys. Res. Lett.***, ***37*** (24), doi:10.1029/2010GL045464, 2010.

Tollefson, J., IPCC says limiting global warming to 1.5 °C will require drastic action, ***Nature***, ***562*** (7726), 172–173, doi:10.1038/d41586-018-06876-2, 2018.

Thompson, D.W. and S. Solomon,Understanding recent stratospheric climate change. ***Journal of Climate***, ***22***(8), pp.1934-1943, 2009.

Torres, O., H. Jethva, C. Ahn, G. Jaross, and D.G. Loyola, TROPOMI aerosol products: evaluation and observations of synoptic-scale carbonaceous aerosol plumes during 2018–2020, ***Atmos. Meas. Tech.***, ***13*** (12), 6789–6806, doi:10.5194/amt-13-6789-2020, 2020.

Trenberth, K.E., and A. Dai, Effects of Mount Pinatubo volcanic eruption on the hydrological cycle as an analog of geoengineering, ***Geophys. Res. Lett.***, ***34*** (15), doi:10.1029/2007GL030524, 2007.

Trisos, C.H., G. Amatulli, J. Gurevitch, A. Robock, L. Xia, and B. Zambri, Potentially dangerous consequences for biodiversity of solar geoengineering implementation and termination, ***Nat. Ecol. Evol.***, ***2*** (3), 475–482, doi:10.1038/s41559-017-0431-0, 2018.

Van Roozendael, M., M. De Maziere, C. Hermans, P.C. Simon, J.P. Pommereau, F. Goutail, X.X. Tie, G. Brasseur, and C. Granier, Ground-based observations of stratospheric NO2 at high and midlatitudes in Europe after the Mount Pinatubo eruption, ***J. Geophys. Res. Atmos.***, ***102*** (D15), 19,171–19,176, doi:10.1029/97JD01098, 1997.

Vattioni, S., D. Weisenstein, D. Keith, A. Feinberg, T. Peter, and A. Stenke, Exploring accumulation-mode H_2SO_4 versus SO_2 stratospheric sulfate geoengineering in a sectional aerosol–chemistry–climate model, ***Atmos. Chem. Phys.***, ***19***, 4877–4897, doi:10.5194/acp-19-4877-2019, 2019.

Vehkamäki, H., M. Kulmala, I. Napari, K.E.J. Lehtinen, C. Timmreck, M. Noppel, and A. Laaksonen, An improved parameterization for sulfuric acid water nucleation rates for tropospheric and stratospheric conditions, ***J. Geophys. Res.***, ***107*** (D22), 4622, doi:10.1029/2002JD002184, 2002.

Vernier, J.P., L.W. Thomason, J.P. Pommereau, A. Bourassa, J. Pelon, A. Garnier, A. Hauchecorne, L. Blanot, C. Trepte, D. Degenstein, and F. Vargas, Major influence of tropical volcanic eruptions on the stratospheric aerosol layer during the last decade, ***Geophys. Res. Lett.***, ***38*** (12), doi:10.1029/2011GL047563, 2011.

Visioni, D., G. Pitari, and V. Aquila, Sulfate geoengineering: a review of the factors controlling the needed injection of sulfur dioxide, ***Atmos. Chem. Phys.***, ***17***, 3879–3889, doi:10.5194/acp-17-3879-2017, 2017a.

Visioni, D., G. Pitari, V. Aquila, S. Tilmes, I. Cionni, G. Di Genova, and E. Mancini, Sulfate geoengineering impact on methane transport and lifetime: results from the Geoengineering Model Intercomparison Project (GeoMIP), ***Atmos. Chem. Phys.***, ***17***, 11,209–11,226, doi:10.5194/acp-17-11209-2017, 2017b.

Visioni, D., G. Pitari, G. di Genova, S. Tilmes, and I. Cionni, Upper tropospheric ice sensitivity to sulfate geoengineering, ***Atmos. Chem. Phys.***, ***18***, 14,867–14,887, doi:10.5194/acp-18-14867-2018, 2018.

Visioni, D., D.G. MacMartin, B. Kravitz, S. Tilmes, M.J. Mills, J.H. Richter, and M.P. Boudreau, Seasonal injection strategies for stratospheric aerosol geoengineering, ***Geophys. Res. Lett.***, ***46*** (13), 7790-7799, doi:10.1029/2019GL083680, 2019.

Visioni, D., D.G. MacMartin, B. Kravitz, J.H. Richter, S. Tilmes, and M.J. Mills, Seasonally modulated stratospheric aerosol geoengineering alters the climate outcomes, ***Geophys. Res. Lett.***, ***47*** (12), e2020GL088337, doi:10.1029/2020GL088337, 2020a.

Visioni, D., D.G. MacMartin, B. Kravitz, W. Lee, I.R. Simpson, and J.H. Richter, Reduced poleward transport due to stratospheric heating under stratospheric aerosols geoengineering, ***Geophys. Res. Lett.***, ***47*** (17), e2020GL089470, doi:10.1029/2020GL089470, 2020b.

Visioni, D., E. Slessarev, D.G. MacMartin, N.M. Mahowald, C.L. Goodale, and L. Xia, What goes up must come down: impacts of deposition in a sulfate geoengineering scenario, ***Environ. Res. Lett.***, ***15*** (9), 094063, doi:10.1088/1748-9326/ab94eb, 2020c.

Visioni, D., D.G. MacMartin, B. Kravitz, O. Boucher, A. Jones, T. Lurton, M. Martine, M.J. Mills, P. Nabat, U. Niemeier, R. Séférian, and S. Tilmes, Identifying the sources of uncertainty in climate model simulations of solar radiation modification with the G6sulfur and G6solar Geoengineering Model Intercomparison Project (GeoMIP) simulations, ***Atmos. Chem. Phys.***, ***21***, 10,039–10,063, doi:10.5194/acp-21-10039-2021, 2021a.

Visioni, D., D.G. MacMartin, and B. Kravitz, Is turning down the sun a good proxy for stratospheric sulfate geoengineering?, ***J. Geophys. Res. Atmos.***, ***126*** (5), e2020JD033952, doi:10.1029/2020JD033952, 2021b.

Visioni, D., S. Tilmes, C. Bardeen, M. Mills, D.G. MacMartin, B. Kravitz, and Richter, J.H., 2022, Limitations of assuming internal mixing between different aerosol species: a case study with sulfate geoengineering simulations. ***Atmospheric Chemistry and Physics***, ***22***(3), pp.1739-1756, 2022.

Wei, L., D. Ji, C. Miao, H. Muri, and J.C. Moore, Global streamflow and flood response to stratospheric aerosol geoengineering, ***Atmos. Chem. Phys.***, ***18*** (21), 16,033–16,050, doi:10.5194/acp-18-16033-2018, 2018.

Weisenstein, D., S. Bekki, G. Pitari, C. Timmreck, and M. Mills, Modeling of Stratospheric Aerosols, Chapter 6, in ***SPARC Assessment of Stratospheric Aerosol Properties (ASAP)***, edited by L. Thomason and Th. Peter, SPARC Report No. 4, WCRP-124, WMO/TD–No. 1295, 54 pp., Stratosphere-troposphere Processes And their Role in Climate, [available at: https://www.sparc-climate.org/publications/sparc-reports/sparc-report-no-4/], 2006.

Weisenstein, D.K., D.W. Keith, and J.A. Dykema, Solar geoengineering using solid aerosol in the stratosphere, ***Atmos. Chem. Phys.***, ***15*** (20), 11,835–11,859, doi:10.5194/acp-15-11835-2015, 2015.

Weisenstein, D.K., D. Visioni, H. Franke, U. Niemeier, S. Vattioni, G. Chiodo, T. Peter, and D.W. Keith, An interactive stratospheric aerosol model intercomparison of solar geoengineering by stratospheric injection of SO2 or accumulation-mode sulfuric acid aerosols, ***Atmos. Chem. Phys.***, ***22***, 2955–2973, doi:10.5194/acp-22-2955-2022, 2022.

Wigley, T.M.L., A combined mitigation/geoengineering approach to climate stabilization, ***Science***, ***314***, 452–454, doi:10.1126/science.1131728, 2006.

Wilka, C., K. Shah, K. Stone, S. Solomon, D. Kinnison, M. Mills, A. Schmidt, and R.R. Neely III, On the role of heterogeneous chemistry in ozone depletion and recovery. ***Geophysical Research Letters***, ***45***(15), pp.7835-7842, 2018.

Wu, H., J.W. Taylor, J.M. Langridge, C. Yu, J.D. Allan, K. Szpek, M.I. Cotterell, P.I. Williams, M. Flynn, P. Barker, C. Fox, G. Allen, J. Lee, and H. Coe, Rapid transformation of ambient absorbing aerosols from West African biomass burning, ***Atmos. Chem. Phys.***, ***21***, 9417–9440, doi:10.5194/acp-21-9417-2021, 2021.

Xia, L., A. Robock. J.N.S. Cole, C.L. Curry, D. Ji, A. Jones, B. Kravitz, J.C. Moore, H. Muri, U. Niemeier, B. Singh, S. Tilmes, S. Watanabe, and J.-H. Yoon, Solar Radiation Management impacts on agriculture in China: A case study in the Geoengineering Model Intercomparison Project (GeoMIP), ***J. Geophys. Res. Atmos.***, ***119*** (14), 8695–8711, doi:10.1002/2013JD020630, 2014.

Xia, L., A. Robock, S. Tilmes, and R.R. Neely, Stratospheric sulfate geoengineering could enhance the terrestrial photosynthesis rate, ***Atmos. Chem. Phys.***, ***16*** (3), 1479–1489, doi:10.5194/acp-16-1479-2016, 2016.

Xia, L., P.J. Nowack, S. Tilmes, and A. Robock, Impacts of stratospheric sulfate geoengineering on tropospheric ozone, ***Atmos. Chem. Phys.***, ***17***, 11,913–11,928, doi:10.5194/acp-17-11913-2017, 2017.

Yook, S., D.W. Thompson, and S. Solomon, Climate impacts and potential drivers of the unprecedented Antarctic ozone holes of 2020 and 2021. ***Geophysical Research Letters***, p.e2022GL098064, 2022.

Young, R.E., H. Houben, and O.B. Toon, Radiatively forced dispersion of the Mount Pinatubo volcanic cloud and induced temperature perturbations in the stratosphere during the first few months following the eruption, ***Geophys. Res. Lett.***, ***21*** (5), 369–372, doi:10.1029/93GL03302, 1994.

Yu, P., O.B. Toon, C.G. Bardeen, Y. Zhu, K.H. Rosenlof, R.W. Portmann, T.D. Thornberry, R.S. Gao, S.M. Davis, E.T. Wolf, and J. de Gouw, Black carbon lofts wildfire smoke high into the stratosphere to form a persistent plume, ***Science***, ***365*** (6453), 587–590, doi:10.1126/science.aax1748, 2019.

Yu, P., S.M. Davis, O.B. Toon, R.W. Portmann, C.G. Bardeen, J.E. Barnes, H. Telg, C. Maloney, and K.H. Rosenlof, Persistent stratospheric warming due to 2019–2020 Australian wildfire smoke, ***Geophys. Res. Lett.***, ***48*** (7), e2021GL092609, doi:10.1029/2021GL092609, 2021.

Zambri, B., A.N. LeGrande, A. Robock, and J. Slawinska, Northern Hemisphere winter warming and summer monsoon reduction after volcanic eruptions over the last millennium, ***J. Geophys. Res. Atmos.***, ***122*** (15), 7971–7989, doi:10.1002/2017JD026728, 2017.

Zanchettin, D., M. Khodri, C. Timmreck, M. Toohey, A. Schmidt, E.P. Gerber, G. Hegerl, A. Robock, F.S.R. Pausata, W.T. Ball, S.E. Bauer, S. Bekki, S.S. Dhomse, A.N. LeGrande, G.W. Mann, L. Marshall, M. Mills, M. Marchand, U. Niemeier, V. Poulain, E. Rozanov, A. Rubino, A. Stenke, K. Tsigaridis, and F. Tummon, The Model Intercomparison Project on the climatic response to Volcanic forcing (VolMIP): experimental design and forcing input data for CMIP6, ***Geosci. Model Dev.***, ***9*** (8), 2701–2719, doi:10.5194/gmd-9-2701-2016, 2016.

Zhu, Y., O.B. Toon, D. Kinnison, V.L. Harvey, M.J. Mills, C.G. Bardeen, M. Pitts, N. Bègue, J.B. Renard, G. Berthet, and F. Jégou, Stratospheric aerosols, polar stratospheric clouds, and polar ozone depletion after the Mount Calbuco eruption in 2015, ***J. Geophys. Res. Atmos.***, ***123*** (21), 12,308–12,331, doi:10.1029/2018JD028974, 2018.

Zhu, Y., O.B. Toon, E.J. Jensen, C.G. Bardeen, M.J. Mills, M.A. Tolbert, P. Yu, and S. Woods, Persisting volcanic ash particles impact stratospheric SO2 lifetime and aerosol optical properties, ***Nat. Commun.***, ***11*** (1), 1–11, doi:10.1038/s41467-020-18352-5, 2020.